E-ELT PROGRAMME

MICADO Phase A
Opto-Mechanical Design and Analysis

Document: E-TRE-MCD-561-0011

Issue: 5.0

Date: 2009-10-23

Author(s)	D. Magrin N. Tromp M. Drost H. Hanenburg	
Proj. Manager	R. Davies	R. Davies
	Name	Date & Signature

CHANGE RECORD

ISSUE	DATE	SECTION/PAGE AFFECTED	REASON/ REMARKS
1.0	2008-10-3	All	First issue
2.3	2008-11-17	All	Revised for Phase A1
2.4	2008-12-8	All	Updated according to RIX 77
5.0	2009-10-23	All	Fully updated for Phase A

TABLE OF CONTENTS

ABBREVIATIONS AND ACRONYMS

AO	Adaptive Optics
ADC	Atmospheric Dispersion Corrector
CAD	Computer Aided Design
CAE	Computer Aided Engineering
CoG	Centre of Gravity
CTE	Coefficient of Thermal Expansion
ECSS	European Cooperation for Space Standardization
E-ELT	European Extremely Large Telescope
EGSE	Electronically Ground Support Equipment
ESO	European Southern Observatory
FDR	Final Design Review
FTE	Full Time Equivalent (year)
GLAO	Ground Layer Adaptive Optics
GMT	Giant Magellan Telescope
JWST	James Web Space Telescope
LESIA	Laboratoire d'Etudes Spatiales et Instrumentations pour l'Astrophysique
LTAO	Laser Tomography Adaptive Optics
MAIT	Manufacture, Assembly, Integration, Test
MAORY	Multi-conjugate Adaptive Optics Relay
MCAO	Multi-conjugate adaptive optics
MGSE	Mechanically Ground Support Equipment
MIA	Milling In Assembly
MICADO	Multi-adaptive optics Imaging Camera for Deep Observations
MPE	Max-Planck-Institut für extraterrestrische Physik
MPIA	Max-Planck-Institut für Astronomie
NOVA	Nederlandse Onderzoekschool voor Astronomie
OAPD	Osservatorio Astronomico di Padova
OGSE	Optically Ground Support Equipment
PAE	Preliminary Acceptance in Europe
PAO	Preliminary Acceptance at the Observatory
PA/QA	Product Assurance / Quality Assurance
PDR	Preliminary Design Review
PSF	Point Spread Function
RTD	Real Time Display
SCAO	Single-Conjugate Adaptive Optics
TMT	Thirty Meter Telescope
USM	Universitäts-Sternwarte München
WP	Workpackage

1 SCOPE

This document describes to an advanced conceptual level the optical, mechanical, and cryogenic design of the Phase A concept for the MICADO instrument. It describes the various sub-systems, specifies the key components, and includes analyses of the tolerances. The decision path followed to select appropriate design options and the resulting (minimal) risks is given elsewhere, in the Design Trade-Off and Risk Assessment (RD4).

2 APPLICABLE AND REFERENCE DOCUMENTS

2.1 Applicable Documents

The following applicable documents form a part of the present document to the extent specified herein. In the event of conflict between applicable documents and the content of the present document, the present document shall be taken as superseding.

AD1 Common definitions and acronyms , E-ESO-SPE-313-0066, Issue 1

AD2 E-ELT Interfaces for Scientific Instruments, E-TRE-ESO-586-0252, issue 1

AD3 Call for Proposal For a Phase A Study of a High Angular Resolution Camera for the E-ELT, Specifications of the Instrument to be studied, E-ESO-SPE-561-0097, v2.0

AD4 Statement of Work for the Phase A Design of MICADO, E-SOW-ESO-561-0127, v1.0

AD5 E-ELT Optical Design Report, E-TRE-ESO-227-138 Issue 3

AD6 Properties and Cost of Reference Detectors, Technical Note INS-2009/02

2.2 Reference Documents

RD1 MICADO Instrument Development and Management Plan, E-PLA-MCD-561-0020, v1.0

RD2 MICADO Scientific Analysis Report, E-TRE-MCD-561-0007, v2.0

RD3 MICADO System Overview, E-TRE-MCD-561-0009, v2.0

RD4 MICADO Design Trade-Off and Risk Assessment, E-TRE-MCD-561-0010, v2.0

RD5 High Precision Astrometry with MICADO, Trippe et al., MNRAS submitted

RD6 MICADO Single Conjugate Adaptive Optics Module, E-TRE-MCD-561-0022, v1.0

3 INTRODUCTION

This document presents and describes the opto-mechancial and cryogenic design concept developed for the MICADO instrument in a Phase A study. The SCAO module proposed by the MICADO consortium for the initial scientific operations phase is presented in RD6 and is not subject of this document. From hereon the name MICADO is used to represent all components following after the interface with SCAO/MAORY such as the ADC, cold optics, cryostat, electronic racks and support equipment.

During Phase A1 the MICADO consortium has studied two basic general layout options, and chosen the monolithic instrument design to be further pursued. Further trade-off studies have been carried out in Phase A2 (see RD4) and finally brought out an advanced conceptual opto-mechanical and cryogenic design which we consider an ideal starting point for the development and detailed design of a powerful instrument to fulfill all scientific objectives as defined in the Science Analysis Report (RD2) and both promote and exploit the unique potential of the E-ELT.

3.1 Optics

The concept for MICADO comprises purely reflective optics that (i) image a large contiguous field in the primary arm, and (ii) provide additional functionality and flexibility in an auxiliary arm. In the global design, the (warm) ADC and collimators are combined in the central 'common path'. After this, the light is by default directed via fixed mirrors to the camera optics of the primary arm. Alternatively, by rotating in a different parabolic collimator, the light can be sent to the auxiliary arm. An overview of the optics is given in Figure 1.

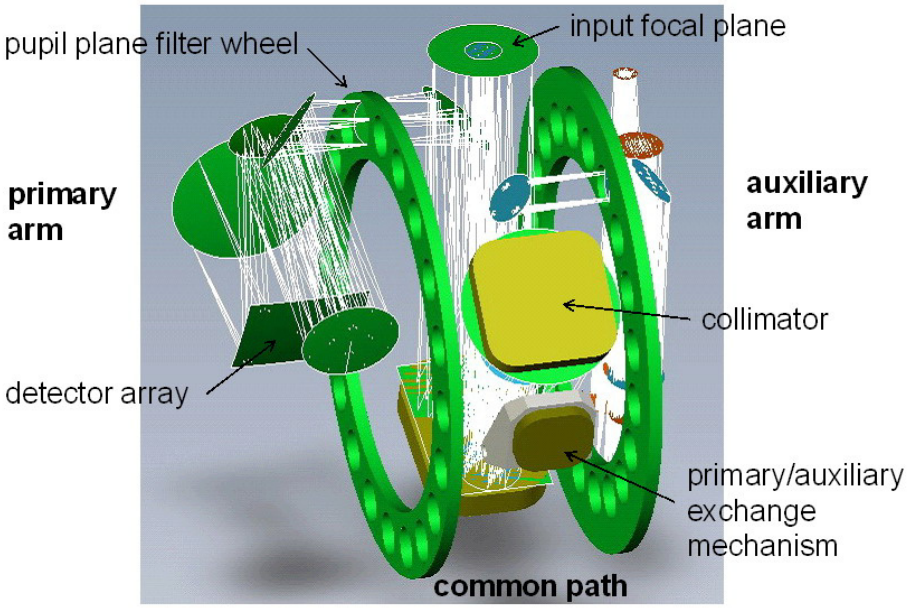

Figure 1: Overview of MICADO optics, which comprises the common path (ADC (not shown) and collimator) in the centre, the primary arm, and the auxiliary arm.

3.2 Mechanics

3.2.1 MICADO General Layout

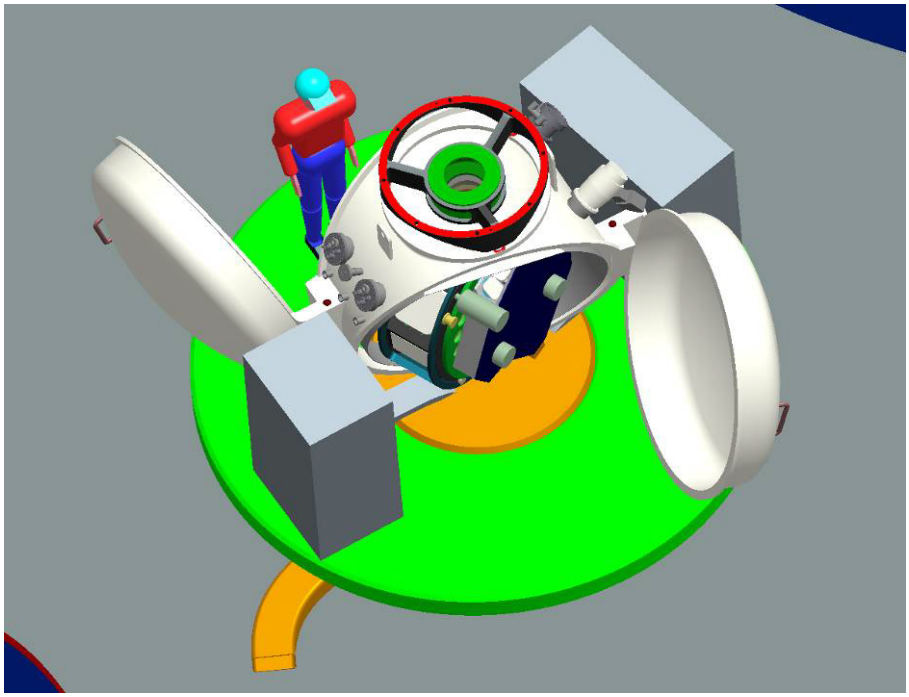

Figure 2: Overview of MICADO. The mechanical interface to the AO systems is the red mounting ring at the top. Access to all key systems is provided through 2 large doors in the cryostat. The electronics are mounted on a co-rotating platform that rests on the Nasmyth floor and provides the cable-wrap for external supplies.

The MICADO instrument must rotate together with the observed field as the optical design does not contain an optical image derotator. The rotation axis is chosen vertical in order to minimize flexure effects. This gravity independent focus is created by both SCAO and MAORY. The mechanical design has been driven by the limited space beneath MAORY. To keep torques small and to maintain optical alignment during cool-down, the centre of gravity is close to the optical axis which itself is close to the centre of shrinkage. In order to minimize cable lengths and to limit the mass mounted on the derotator, the electronics racks are mounted on a co-rotating platform on the Nasmyth floor which also houses the cable-wrap for external supplies. Service and maintenance are key aspects of the design, leading to a design in which the core instrument and optics structure are rotated by 25° with respect to the cryostat. This provides better access through the 2 large cryostat doors to the detector arrays, the primary/auxiliary arm selection and focal plane mechanisms, the filter wheels, and the core optics.

MICADO is surrounded by a cryostat that has a tapered part that provides space for all the through-ports. The instrument inside the cryostat comprises 3 main structures: primary arm, auxiliary arm, and core sub-assembly. The design approach for each of these housings is to assemble them from plate material to keep part complexity and accuracy low, and ensure a rigid boxed structure. The instrument core is supported by the cryostat via 3 V-rods and a transfer structure, which has been designed to accommodate the rotating focal plane mechanism and acts as a bridge to the stiff support structure of the core sub-assembly.

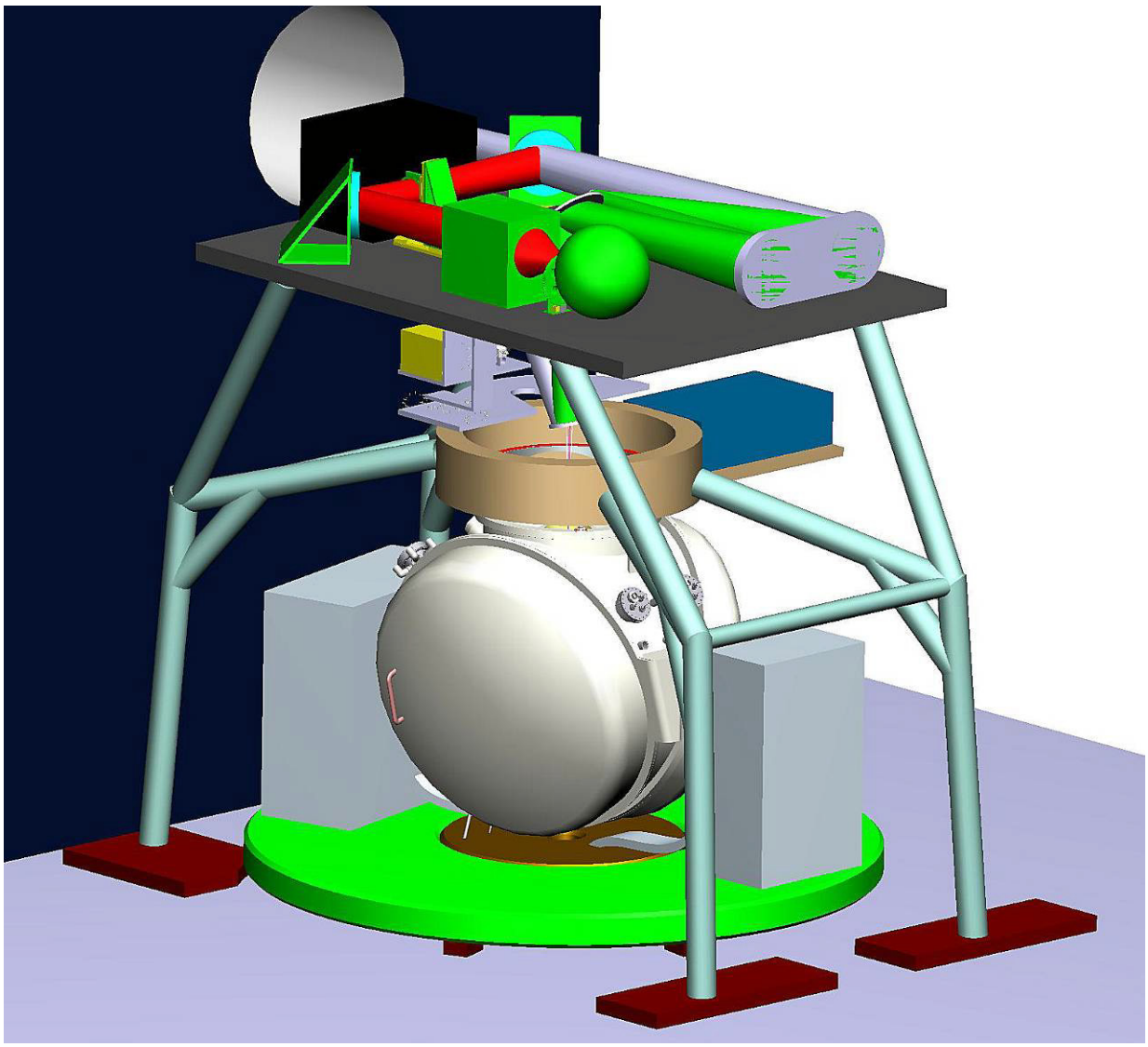

Figure 3: SCAO with MICADO on Nasmyth platform

3.2.2 MICADO Mounting Interface and Space Envelope

Figure 4 shows a simplified representation of the mounting interface of MICADO below the SCAO/MAORY derotator. The focal plane is situated inside the cryostat such that the cryostat entrance window will be positioned somewhere between the MICADO interface and the focal plane.

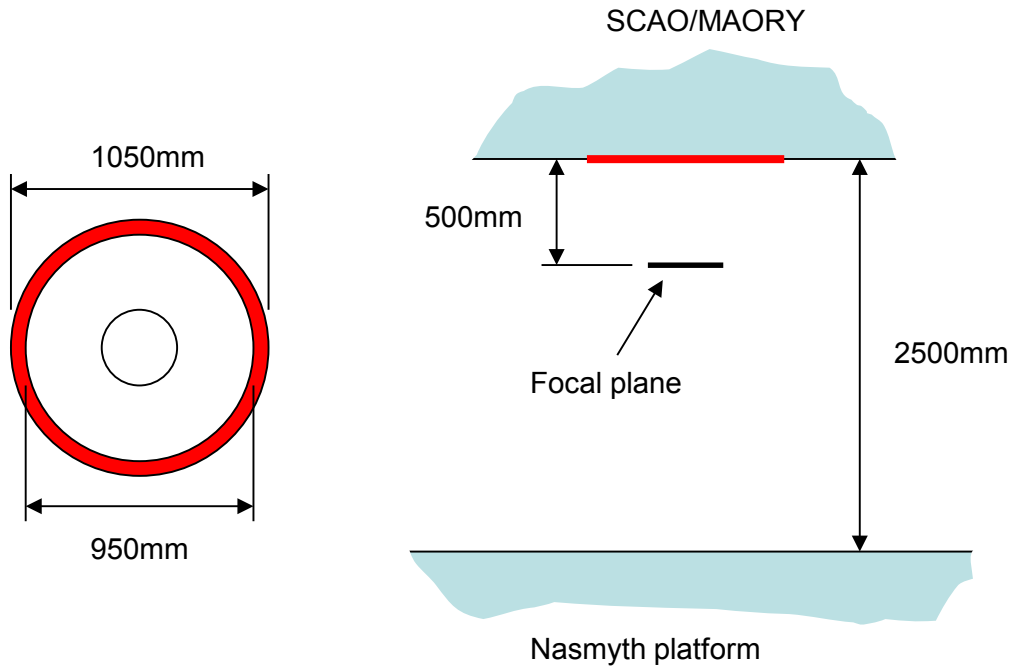

Figure 4: On the left a top view of the MICADO mounting flange, on the right a front view of the MICADO space envelope below SCAO/MAORY with the mounting interface in red.

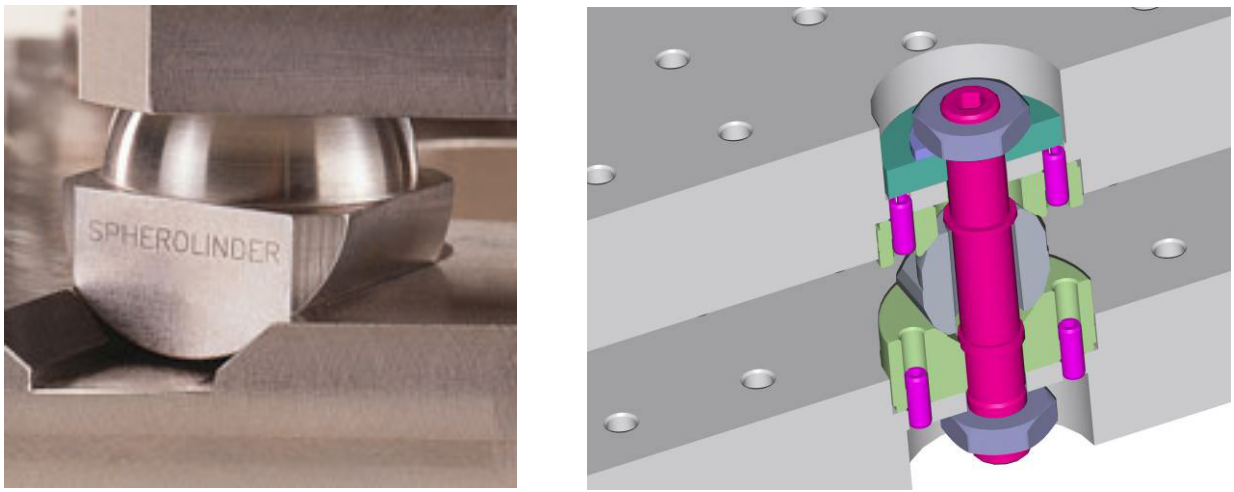

Figure 5: Three spherolinders are used for accurate cryostat repositioning.

Accurate repositioning of the cryostat is possible by the use of three spherolinders (see Figure 5). Three stainless steel spherolinders can easily carry a combined load of 14 tons (source http://www.gizmonicsinc.com/products/spherolinder.html) which is several times the weight of

the MICADO cryostat + instrument. Spring washers are used to cope with differential shrinkage and limit the amount of stress on the sphere/cylinder contact surfaces.

Assembling MICADO without an adjustment possibility is deemed too risky considering the long interface chain from the derotator until the detectors inside the cryostat. The spherolinders themselves don't allow any degree of adjustment; however both the cone and groove part can be designed to move slightly sideways. Using shims and sideways adjusting screws the whole cryostat can be aligned in relation to the incoming beam.

3.2.3 MICADO Dimensions and Mass

3.2.3.1 Cryostat Size

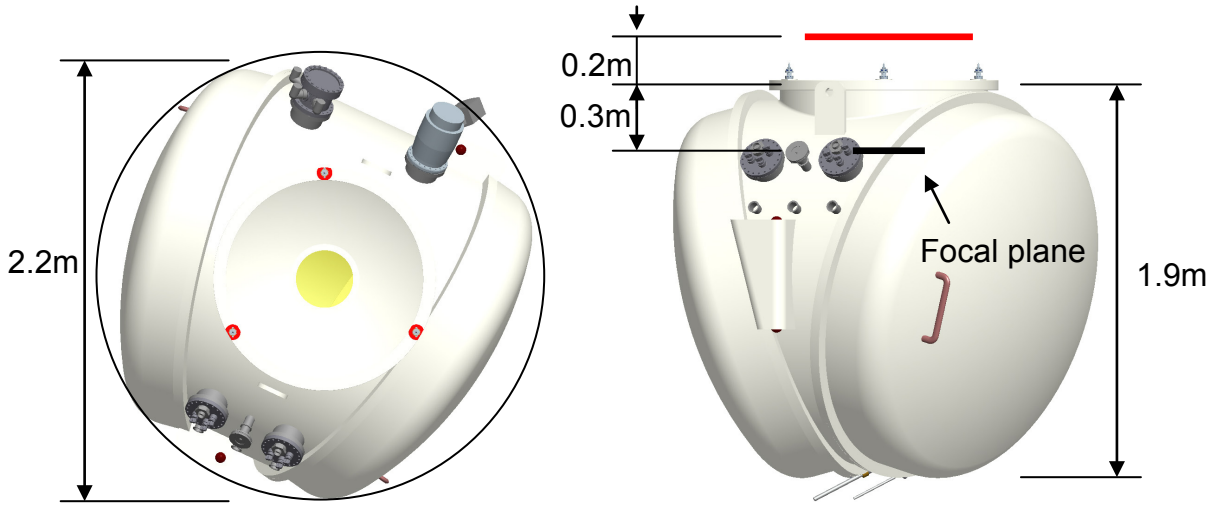

Figure 6: Cryostat dimensions and relative position to MICADO mounting interface.

Figure 6 shows the overall dimensions of the MICADO cryostat housing the cold optics section. The 2.2m diameter is the free rotating diameter. Considering the length of the optical model, from focal plane to detector array, of approximately 6m this is a compact design. The cryostat volume is about 3.5 m^3. The top flange of the cryostat is *not* directly mounted to the MICADO mounting interface: an intermediate support structure of 200mm height is positioned in between (see 6.3.4 for more details).

3.2.3.2 Mass Distribution

Table 1: MICADO mass distribution

Location	Element	Mass estimate, tons
Below derotator	Cryostat	2.1
	Instrument	0.9
On Nasmyth Platform (co-rotating)	Rotating platform	1.2
	Electronics racks	1.1
	Cable wrap	0.5
Static, at input focal plane to AO system	Calibration Unit	0.5
	Total mass	6.3

Mass estimates of the cryostat and instrument shown in Table 1 have been based on the X-Shooter instrument and cryostat keeping in mind the larger volume, a less extreme light weighting of parts, a larger volume of glass type optics and the removal of the LN2 bath.

The resulting instrument mass estimate might look rather high. However, as the instrument is not tilting with regards to the gravity vector, a high degree of instrument light weighting is not necessary. Cool down time could be a driver for a more lightweight design, at the expense of design time, production cost and lead times, but as the volume of moving glass optical elements is high (there are 40 filters), and with limited thermal contact, this will likely dominate the shortest achievable cool down time overruling any lower structural mass benefits.

3.2.4 MICADO Space Claim

The cryostat plus its operational equipment need a certain space envelope and therefore impact the support design of SCAO/MAORY. The collaboration with the SCAO design team has resulted in a compact and efficient space envelope. The next paragraphs describe the MICADO space envelope in three phases: the **operational,** the **servicing** and the **assembly and integration** phase.

3.2.4.1 Operational Space Envelope

By putting all non-cryogenic hardware into the lower regions of the available 2.5m height and using lower electronic racks, the resulting required operational space for MICADO is a cylinder of 3.8m with a rounded top leaving ample room for the derotator to be adequately supported by the SCAO support.

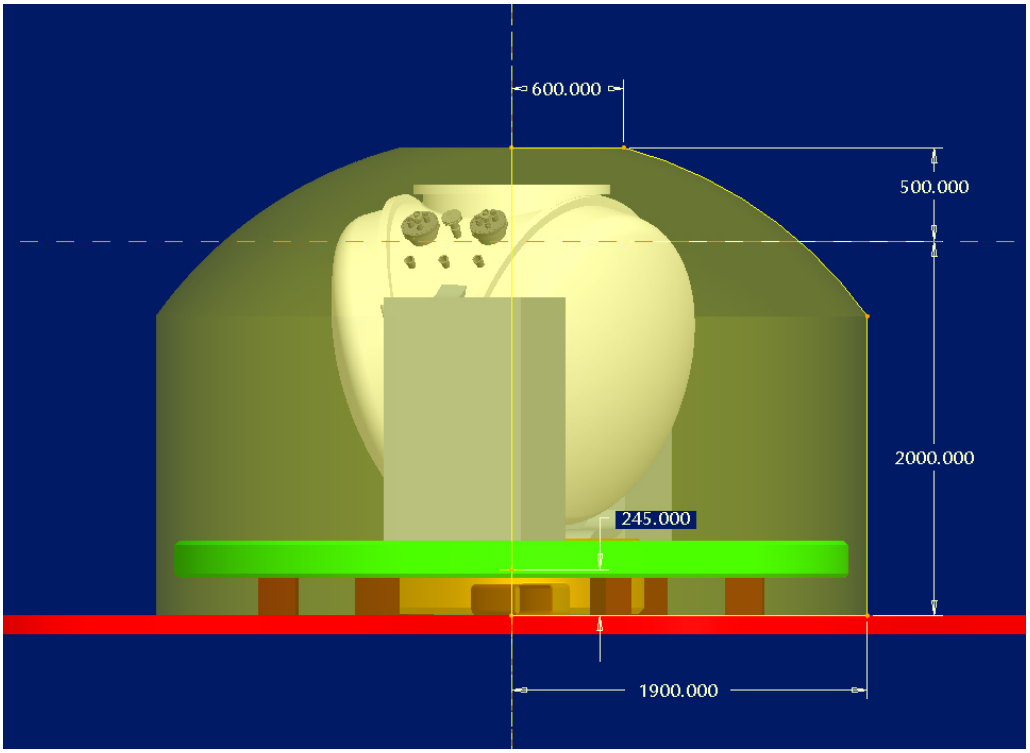

Figure 7: The rotationally symmetric operational space envelope is visible as transparent yellow. Dimensions given are with regards to the focal plane, MICADO mounting interface and Nasmyth platform.

The operational space envelope depicted in Figure 7 is a front view of the free rotating envelope occupied by the cryostat, its extensions, the rotating platform and the electronics racks.

3.2.4.2 Servicing Space Envelope

For servicing of MICADO a much larger cylindrical space is necessary of 5m diameter as shown in Figure 8. This volume may however (partly) be intersected by the support structure of SCAO/MAORY as long as a human being can move around relatively unhindered to reach the various areas on the rotating platform and the electronics racks.

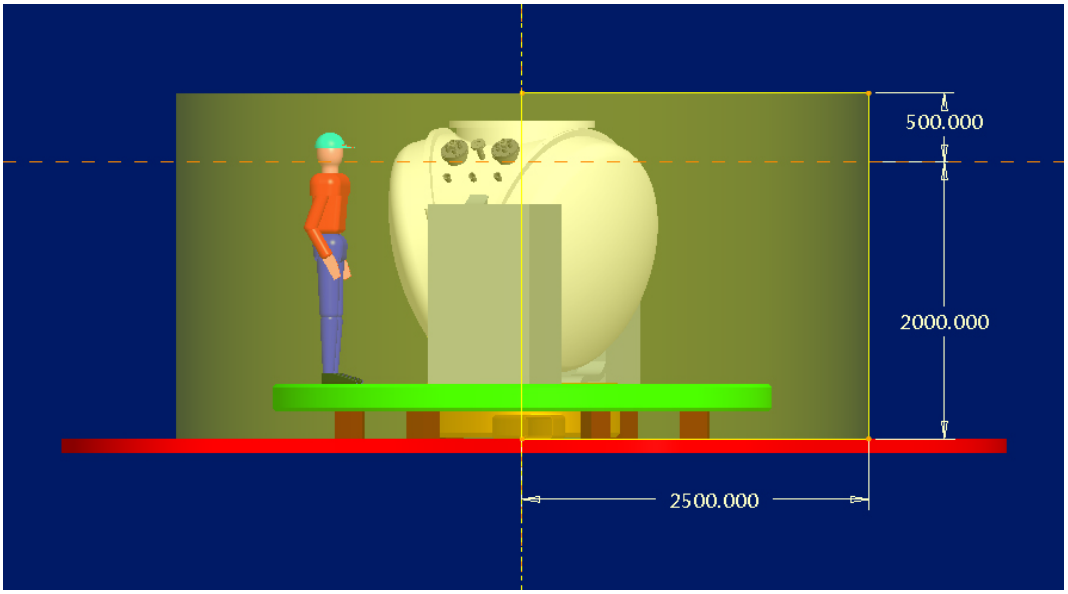

Figure 8: The rotationally symmetric servicing space envelope is visible as transparent yellow. Dimensions given are with regards to the focal plane, MICADO mounting interface and Nasmyth platform.

Inside this volume two areas (see Figure 9) are off-limits to any SCAO/MAORY support structures because of the opening of the hinged cryostat doors (see Figure 9).

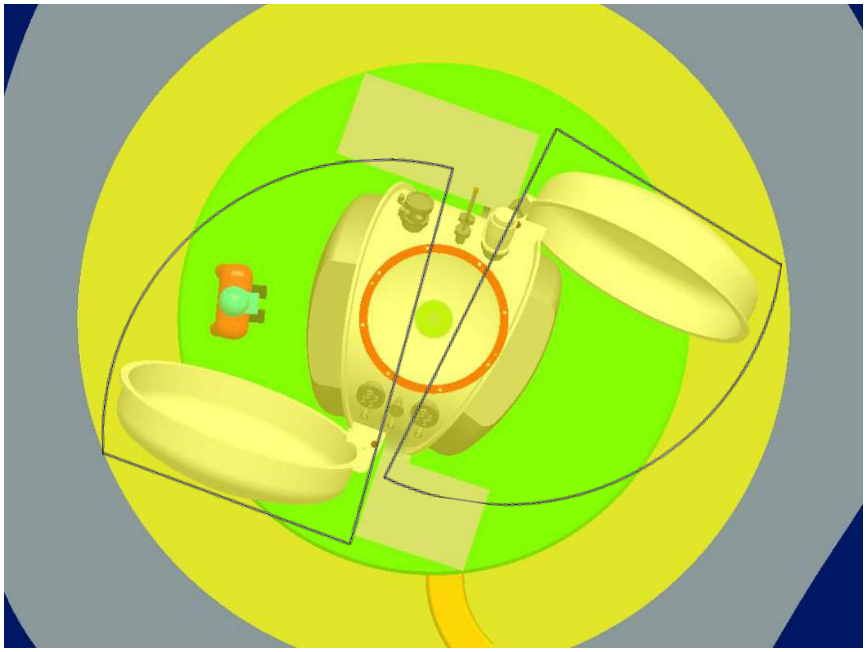

Figure 9: Top view of servicing space envelope (yellow): SCAO/MAORY off-limits area for moving doors within black lines.

The current support designs of both SCAO and MAORY already comply allowing the doors to open freely.

3.2.4.3 Assembly and Integration Space Envelope

All MICADO parts can be assembled on site using a trolley with a manual hydraulic lifting ability. The trolley will run on the Nasmyth platform on temporarily installed rails. In this way MICADO can be installed below SCAO/MAORY.

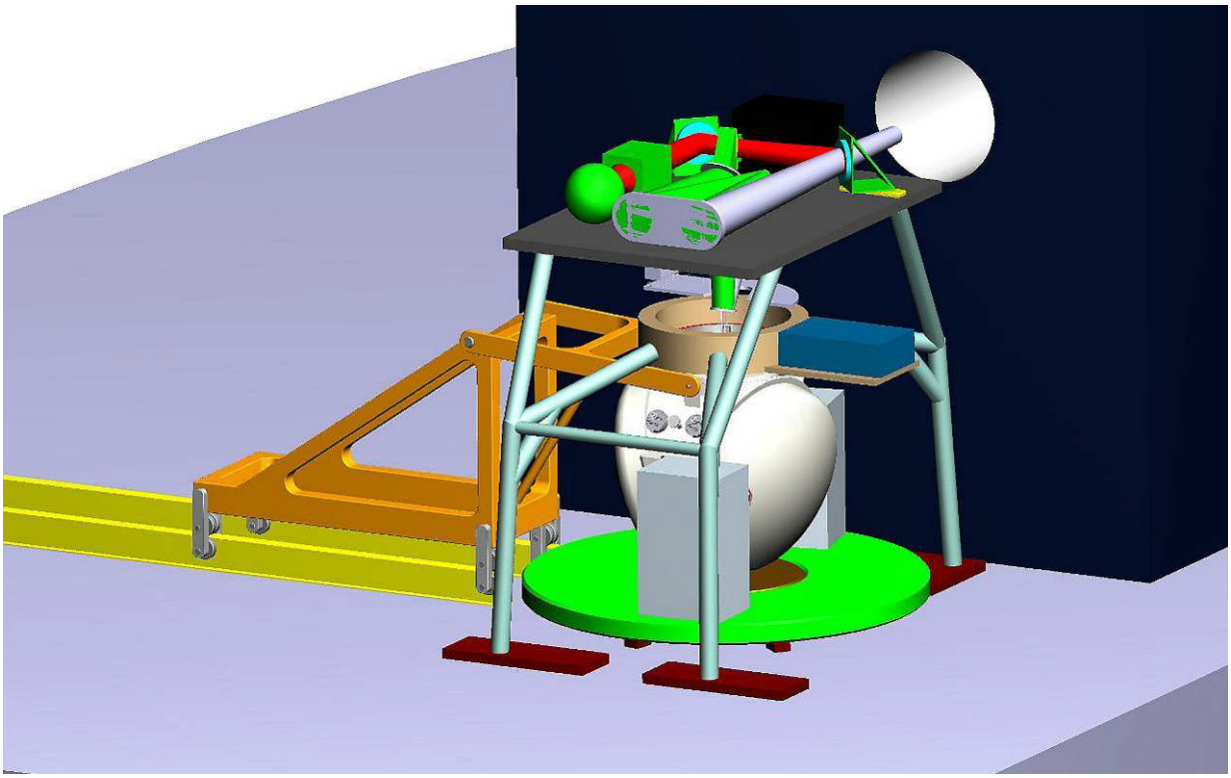

Figure 10: Nasmyth platform with SCAO, MICADO and the MICADO trolley

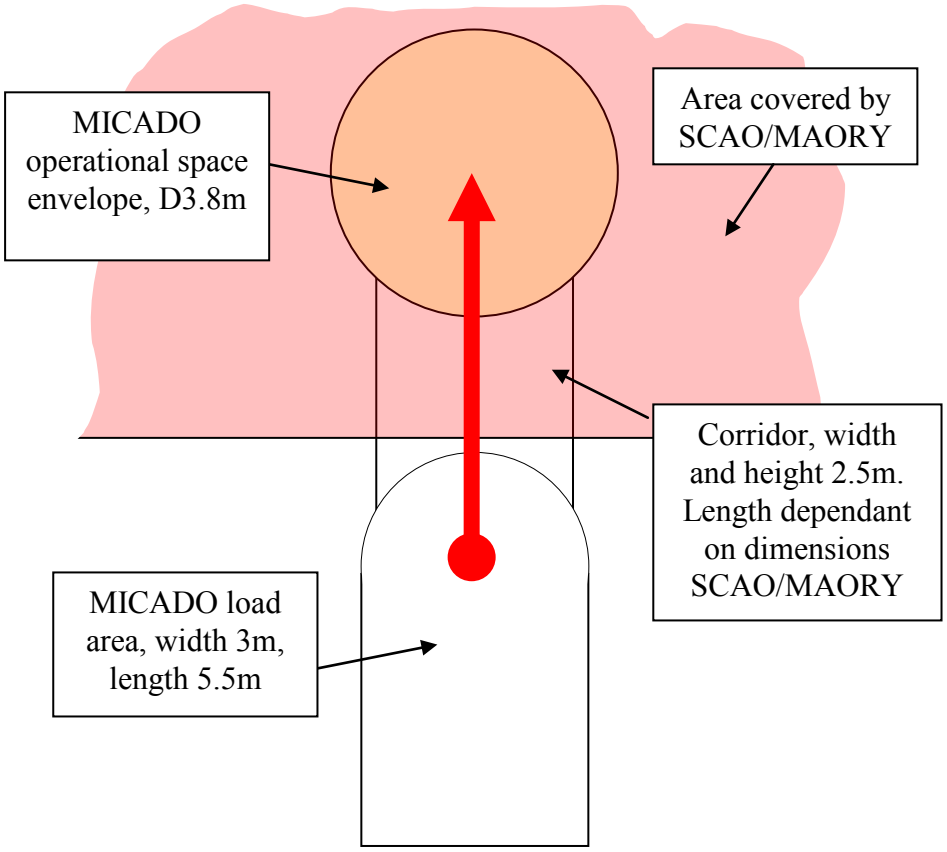

Figure 11: Schematic top view of the MICADO assembly space envelope. Trolley and rails are not shown.

In top view the MICADO load area (see Figure 11) is next to SCAO/MAORY and supposed to be reachable by the telescope crane. This load area is only in use during (dis)assembly of the cryostat.

The corridor is used to transport MICADO to its final location. It's a volume that should not be intersected by any part of the SCAO/MAORY support structure or any other part.

3.3 Cryogenics

The MICADO cooling system is driven by the specified detector temperature which should be lower then 90 K and preferably around 80 K. Open continues flow LN2 cooling is chosen for cooling the cryostat. The circuit uses CRIRES heat exchanger pads and is as simple as possible. Baseline is a serial circuit layout which cools the three temperature levels in the right order. The LN2 flow control is done with a warm valve in the output line. A heater block is put in front of this valve which ensures that no liquid LN2 can flow out of the cryostat. Only the detector temperature is kept warm by electrical heaters.

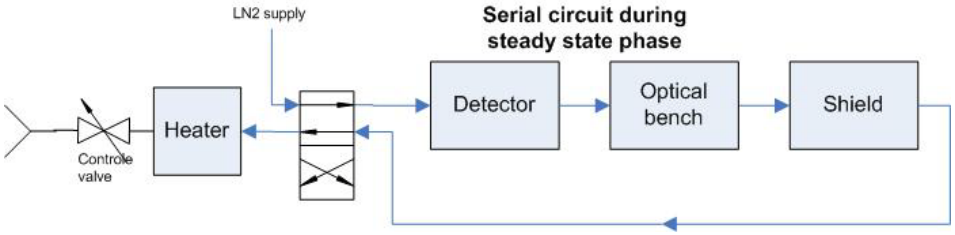

After the cool down phase the flow through the circuit is reversed by switching the LN2 supply and return line.

The detector unit is thermally damped by an additional mass and resistance which are placed in-between the cooling circuit and detector unit. The detector temperature is actively controlled by an electrical heater.

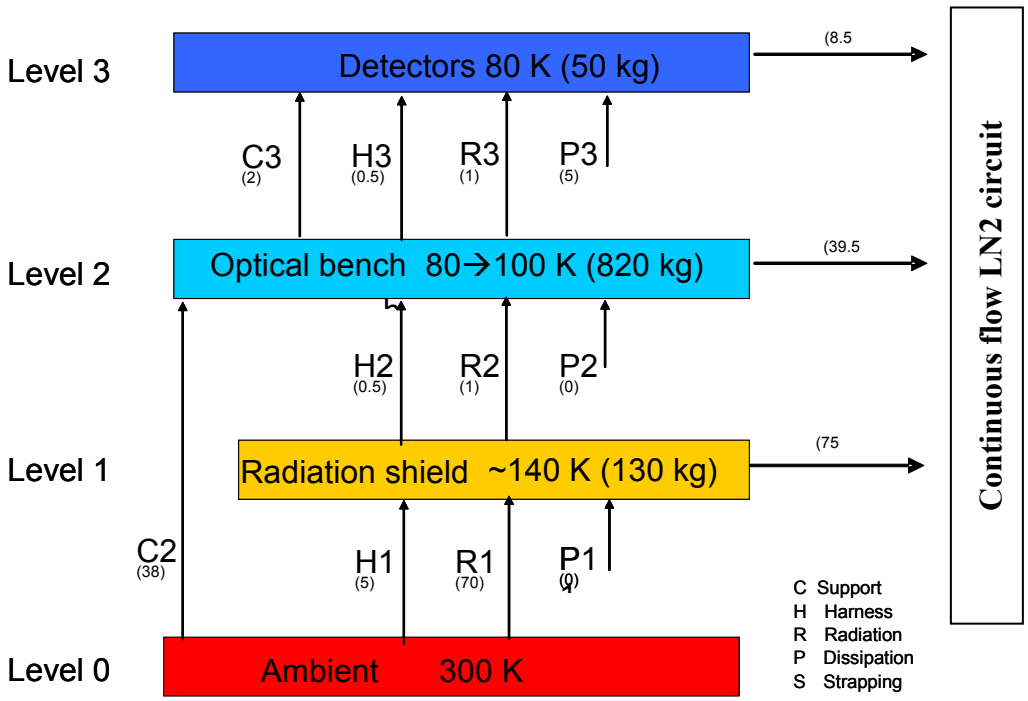

Figure 12: MICADO temperature levels

4 OPTICS

This chapter describes the interfaces between MICADO and MAORY, as identified during the Phase A studies. It is intended to indicate where the interfaces are compatible, as well as to highlight where there might be potential discrepancies.

4.1 ELT, MAORY and SCAO Assumptions

The ELT optical behavior has been simulated using the Zemax file **EELT_v.2BDE.zmx**. The MAORY behavior has been simulated using the Zemax file **MAORY_4M_TLC_2009-02-17_unfold.zmx**. The SCAO module behavior has been simulated using the Zemax file **Relay_V4_multiconf.zmx**.

The MICADO optical design results, both for main and auxiliary arms, are always referred to the concatenation of these ELT+MAORY files or ELT+SCAO files.

4.2 Primary Arm Optical Design

The primary arm provides imaging and astrometric capability over the spectral bands I-z-Y-J-H-K. The wavelength range has been determined by the filter bands of interest:

Name	I	Y	J	H	K	
Central wavelength	0.900	1.021	1.215	1.650	2.200	μm
Width	0.24	0.10	0.26	0.29	0.50	μm

- Wavelength range: (0.900-0.24/2 μm) – (2.20 + 0.50/2) μm = 0.78 μm – 2.45 μm
- Central wavelength: (0.78 μm + 2.32 μm) / 2 = 1.615 μm

The following design refers to ELT+MAORY.

The primary arm is composed of a single off-axis parabolic mirror working as collimator and also a camera based on the well-known concept of Three Mirrors Anastigmatic (TMA). The optical layout is shown in Figure 13.

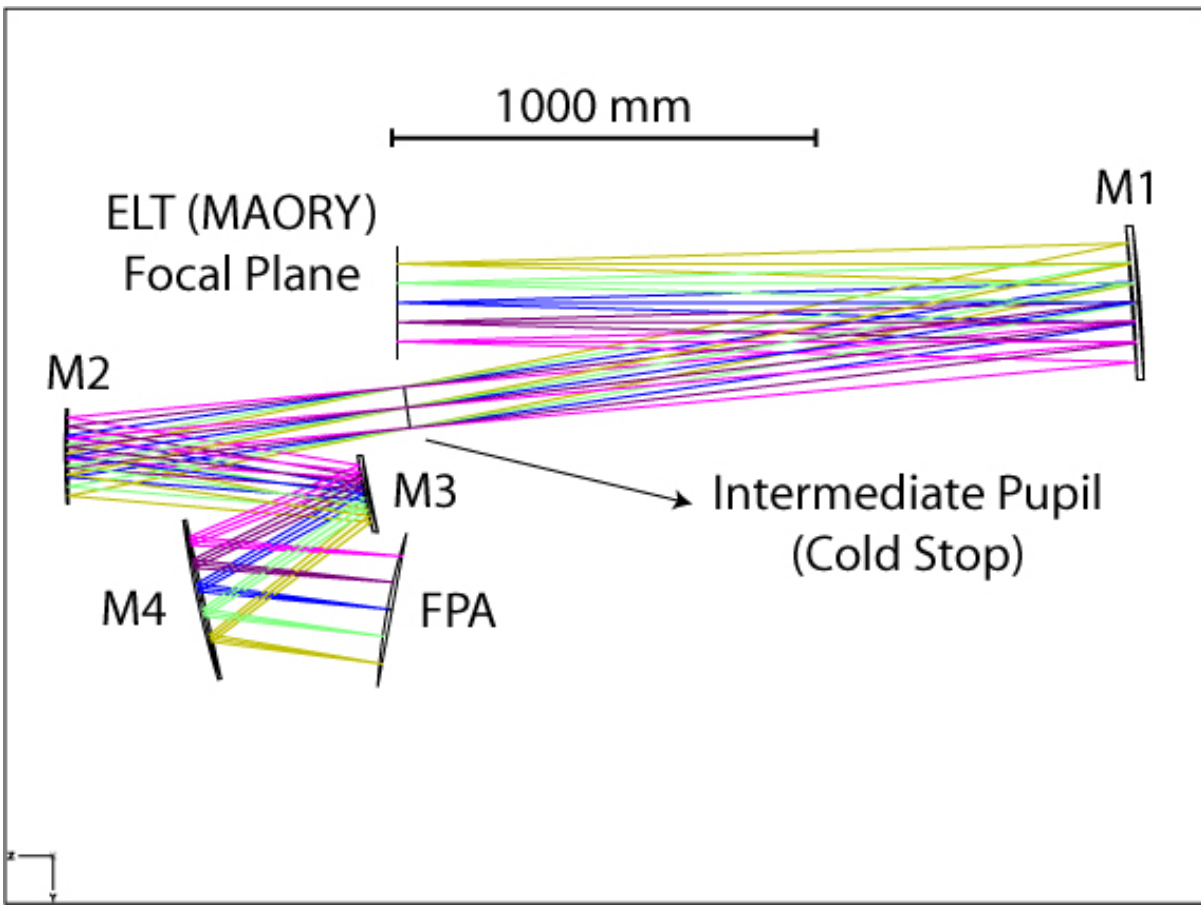

Figure 13: Optical layout of the working mirrors in the primary arm.

The optical design characteristics are as follows:

M1: parabolic concave mirror

M2: elliptical concave mirror

M3: Toroidal convex mirror

M3: spherical concave mirror

The Focal Plane Array (FPA) is composed of 4×4 4096^2 pixels, having a size of 15 μm, with gaps among them of 5 mm. The resulting FPA has a size of 260.76 mm.

The optical design meets the required plate scale of 3mas/px. The simulated FoV size is about $52{,}5\times51.4$ arcsec^2 (tacking into account of the field distortion).

The scale at the ELT focal plane is 3.6 mm/arcsec, implying a FoV at the ELT/MAORY focal plane having dimensions 190.2×186.3 mm^2. The main arm applies a magnification factor (x, y) of (1.37, 1.40), giving a nominal focal plane size of 260.76 mm.

The curvature of the FP supplied by MAORY (1291.94 mm) is translated on a curved camera FP having radius 1500.00 mm. The FPA will mime this shape maximizing the optical quality: the maximum angle of the corner detectors have been estimated to be about 5 degrees (the defocus at the corners of each detector is small).

The spot diagrams for the fields covering the whole FPA (rows) and wavelengths at 0.780, 1.615 and 2.450 μm (columns) are shown in Figure 14**:** ; the Strehl ratio over the entire field of view at the three wavelengths is shown in Figure 15. The worst value is 83.1%, i.e. the main channel is diffraction limited over the whole spectral range.

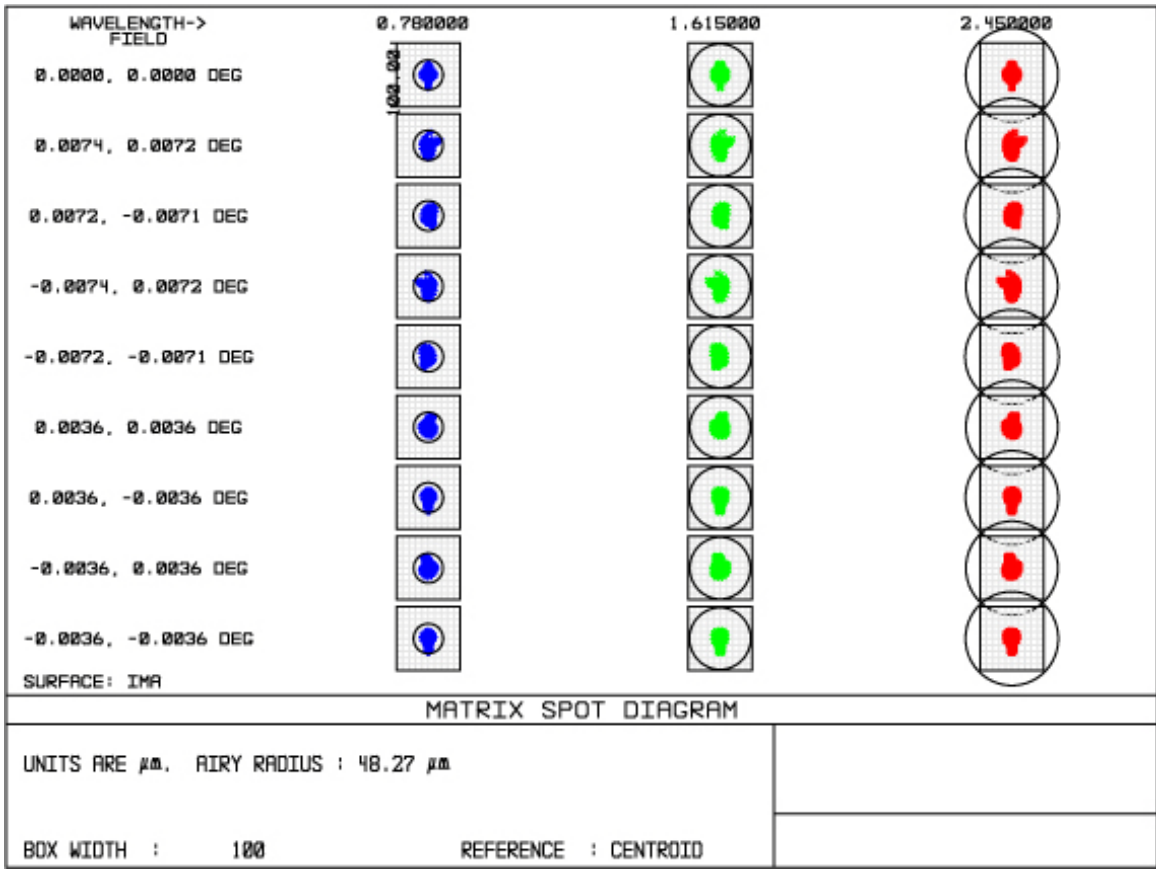

Figure 14: Spot diagrams for different wavelengths (columns) and different FOVs (rows). Circles represent the AIRY disk at the correspondent wavelength.

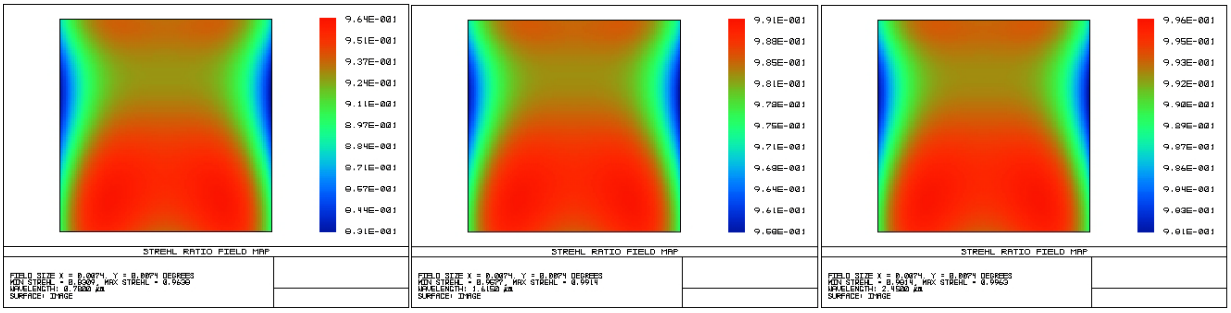

Figure 15: Strehl ratio map over the entire field of view at 0.780, 1.615 and 2.450 μm.

In Figure 16 the footprints of the beam at the pupil image location for different off-axis fields are superimposed. The maximum circular aperture diameter is 100.5 mm. The shape of the cold is circular. The pupil shape varies with field position so cold stop must be undersized at 99.085 mm (i.e. all the light for the on-axis field is unvignetted). The maximum fraction of light blocked is 0.96% for corner field (worst case).

The distortion over the entire field of view has a maximum value of 1.17%. The grid distortion and the footprint over the detector surface are shown in Figure 17. The effective field of view covered by the FPA can be approximated by an isosceles trapeze having the upper base of 53 arcsec, a lower base of 52 arcsec and a height of 51.4 arcsec.

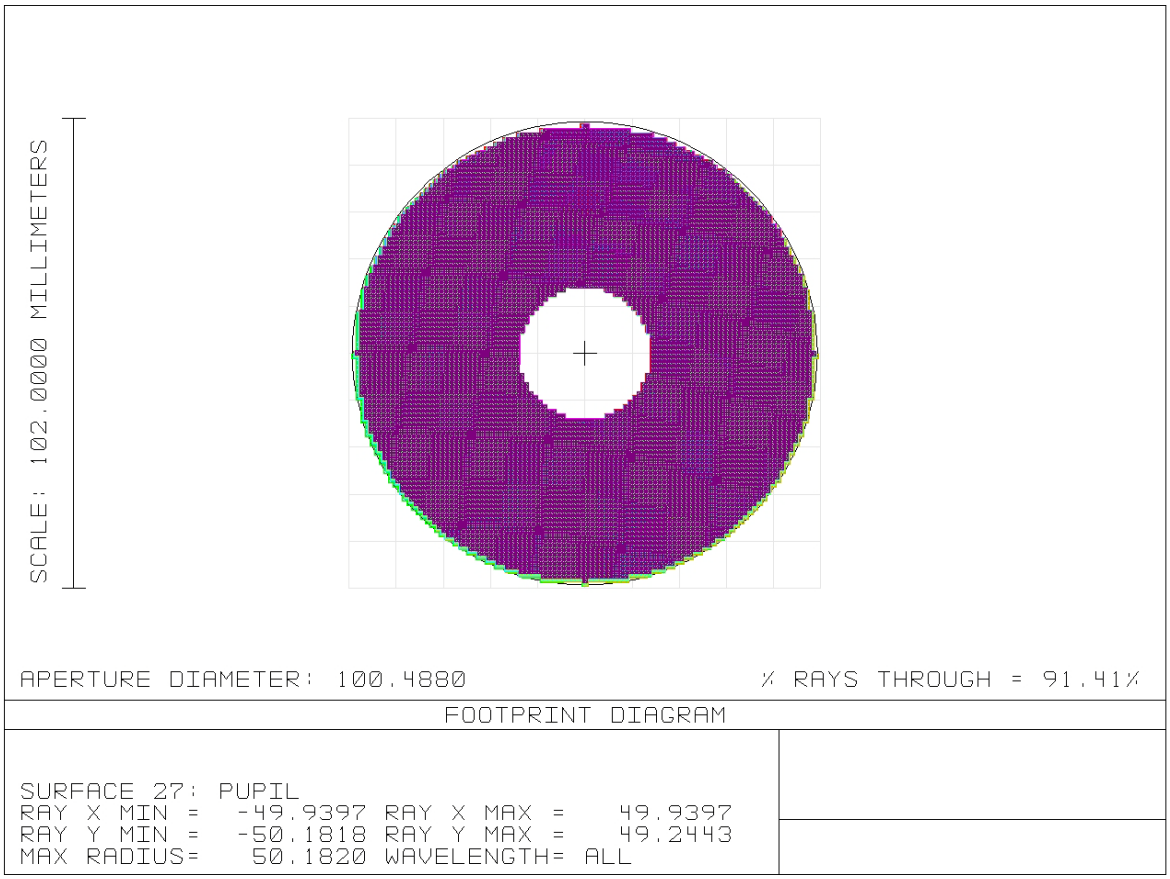

Figure 16: Footprint at the cold stop.

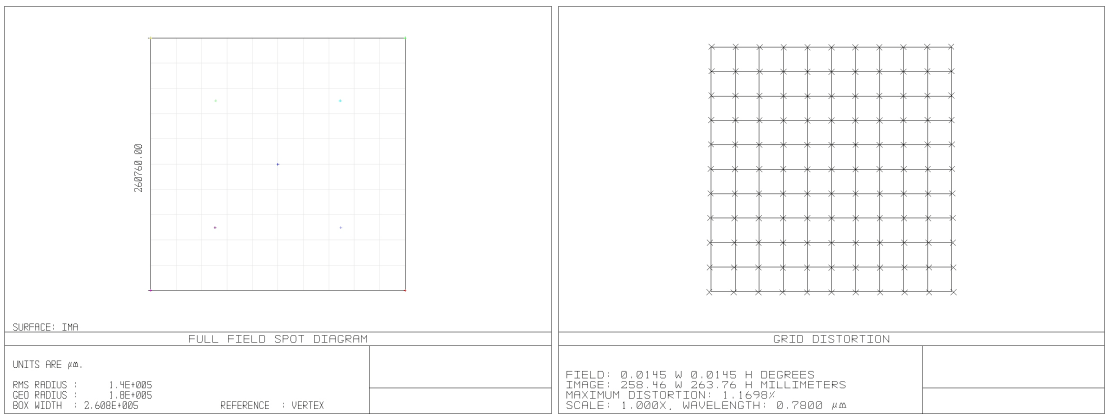

Figure 17: Footprint over the detector surface (left) and the grid distortion over the entire field of view (right).

The field curvature and the field distortion along two orthogonal field directions are shown in Figure 18.

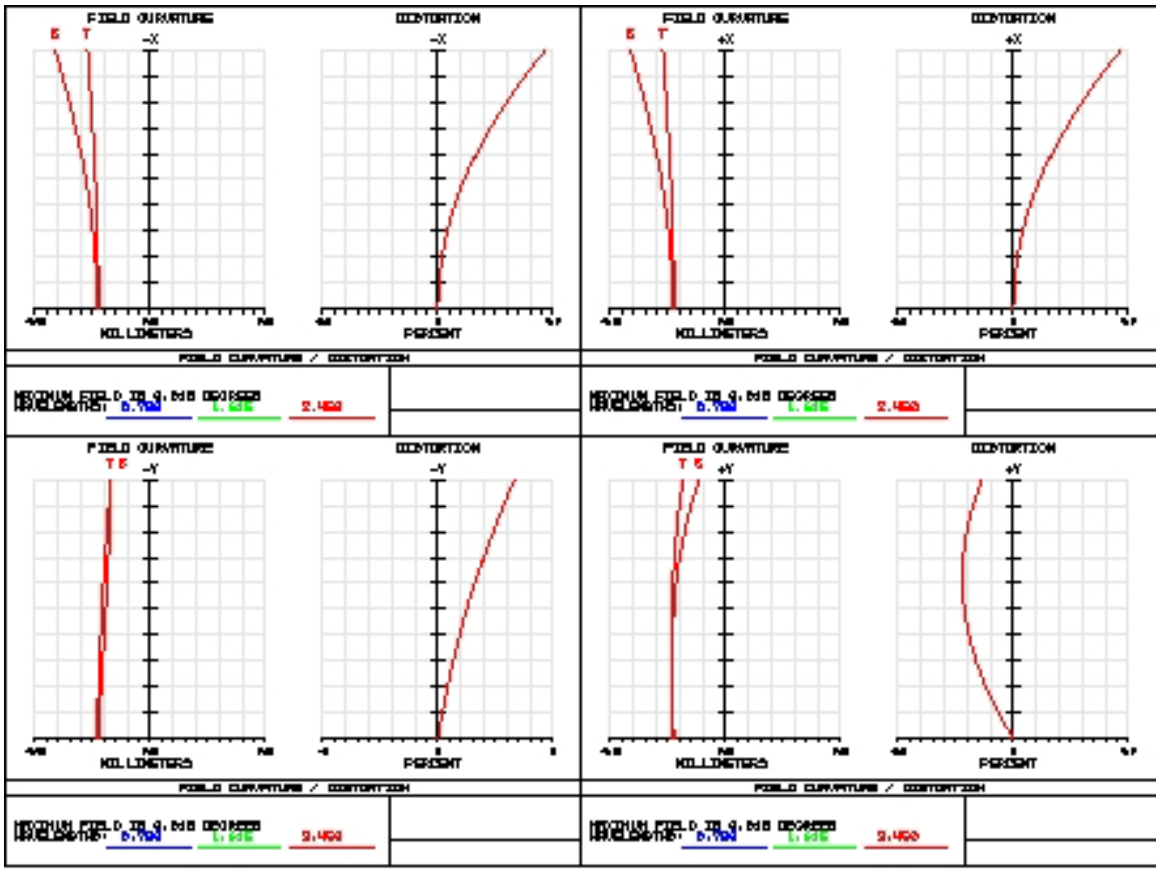

Figure 18: Field curvature (left curve) and absolute distorsion (right curve) vs. fields in different field directions (-x top left, +x top right, -y bottom left, +y bottom right).

Being all the optical elements mirrors, they do not produce any ghost on the focal plane (we expect to have diffuse light in case of poor roughness). The refractive elements that could cause

problems are the filters, the entrance window and the ADC. To avoid the ghosts due to filters it is necessary to tilt the filters with respect to the collimating beam with an angle of about 9 degrees. The ADC presents itself tilted surfaces and should avoid ghosts: an accurate study will be carried out in the next phase (when the ADC parameters and location will be redefined). Assuming a 5 mm thickness ZnSe entrance window, the expected ghost will be spread on FPA over into a spot having diameter 0.372 arcsec (the airy diameter at 1 micron is 0.012 arcsec). The area ratio between the ghost spot and a focalized spot is about 965 times. Moreover the intensity of the light producing the ghost has to be multiplied by a factor $(0.04)^2 - (0.02)^2$ depending on the anti-reflection coating efficiency. A detailed ghost analysis will be done in the next phase.

4.2.1 Primary Arm Folding and Mirror Parameters

The main arm has been folded in order to have a common optical bench with the auxiliary arm (collimator), to allow the accommodation of the filter wheel(s) and to have a separate optical bench for the camera (TMA), minimizing the required volume. All the optical elements (but the filters) are static.

The layout of the folded main arm is shown in Figure 19. The radiation incoming from the entrance focal plane has a first reflection in a double-pass fold mirror MF1, then it is collimated by M1 and reflected back toward MF1 itself and reach the second fold mirror MF2. All these mirrors lay over the same optical bench. The intermediate pupil is formed between the fold mirror MF2 and MF3, and in this position will be allocated the cold stop and the filter wheel. The fold mirror MF3 feeds the TMA and these mirrors lay in a common optical bench. A 3D image of the folded main channel is shown in Figure 20.

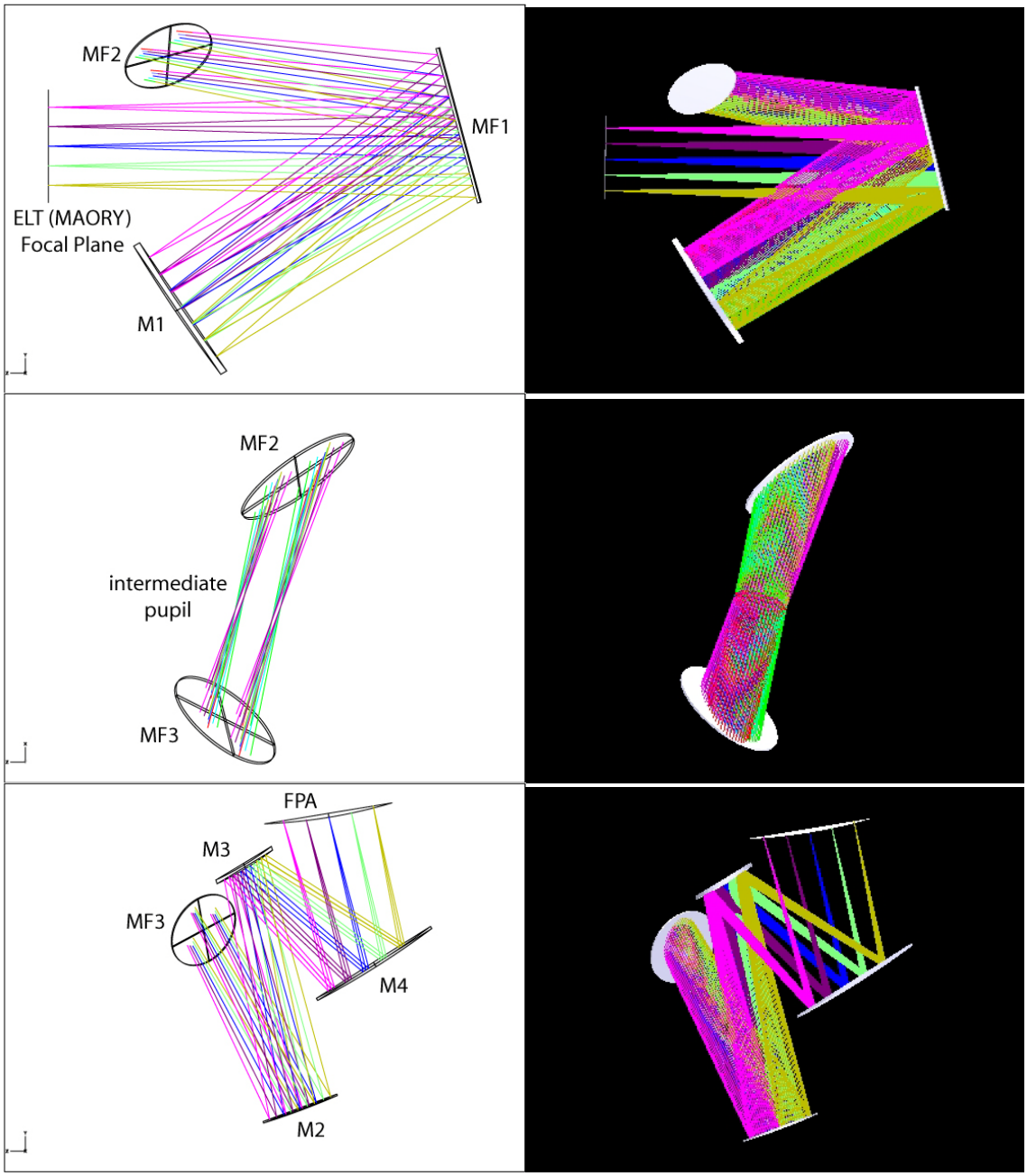

Figure 19: Layout of the folded main channel. Collimator optical bench (top), cold stop position (middle) and camera optical bench (bottom).

The main parameters for all the mirrors are given in Table 2. In the Table, the vertex to center distance has been computed assuming as mirror center the intersection between the chief ray of the on-axis field of view and the mirror surface. The positions of the mirrors have been given in global vertex coordinates assuming a coordinate reference linked to the ELT focal plane.

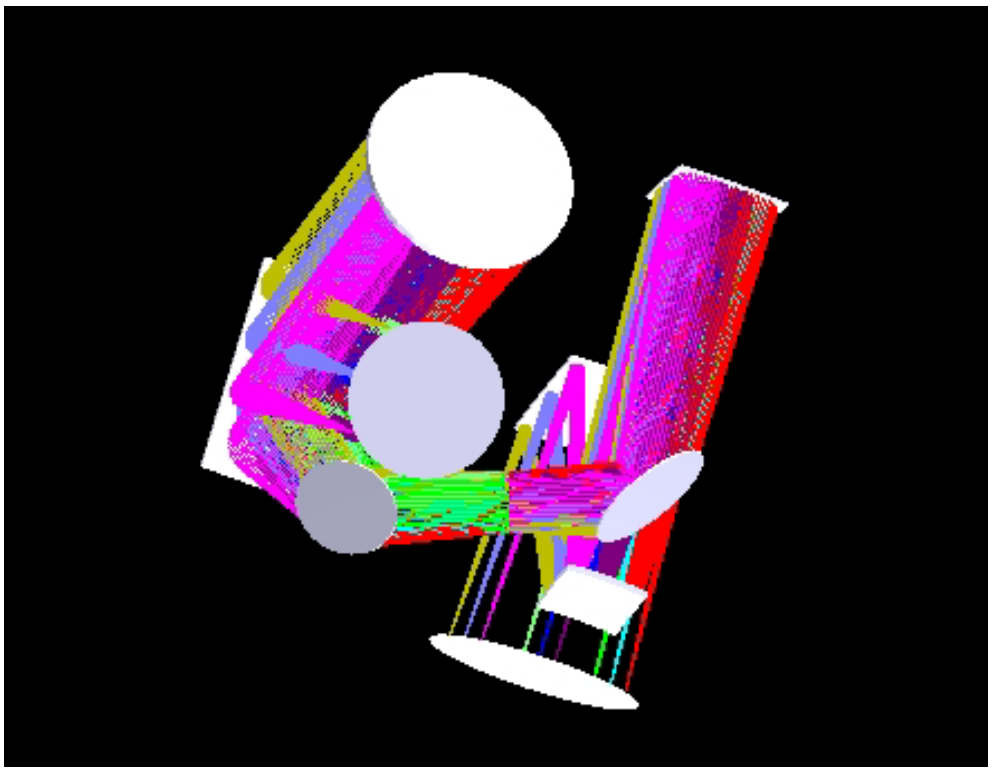

Figure 20: 3D layout of the folded main channel.

Table 2: Main parameters (upper) and global vertex coordinates (lower) for the main arm optical elements.

	R mm	K	Aperture Shape	Clear Aperture mm × mm	Vertex/Center mm
MF1	infinity	-	rectangular	260×380	-
M1	-3474.000	-1	circular	368	-250
MF2	infinity	-	elliptical	230×160	7
MF3	infinity	-	elliptical	160×230	-10
M2	-2043.180	-0.203188	rectangular	196×196	1
M3	-852.566 -843.882	-0.034190 -0.059705	rectangular	144 × 144	210.7
M4	-2449.386	-	rectangular	256 × 276	-12
FPA	-1500.000	-	rectangular	261× 261	-

	Tilt X degree	Tilt Y degree	Tilt Z degree	Decenter X mm	Decenter Y mm	Decenter Z mm
ELT Focal Plane	0	0	0	0	0	0
MF1	15.000	0	0	0	50.000	-980.000
M1	30.000	0	0	0	-171.994	-182.098
MF2	-35.000	45.000	40.000	0	212.390	-280.000
MF3	145.000	45.000	-125.000	-439.341	30.584	-152.887
M2	110.500	0	180.000	-439.341	-483.294	-427.832
M3	107.000	0	180.000	-439.341	121.443	-77.621
M4	122.000	0	180.000	-439.341	-75.849	-629.414
FPA	99.382	0	180.000	-439.341	356.235	-510.781

4.2.2 Primary Arm Tolerance Analysis

A preliminary tolerance analysis has been performed using as a merit function the PSF Strehl ratio > 70% at wavelength 1 micron. A list of parameters have been defined corresponding to the errors in positioning (tilts and decenters) and manufacturing for all the mirrors. All the mirrors are assumed to be independent. The location of the detector has been assumed to be adjustable to the best focus position, allowing one to relax the tolerances.

The sensitivity analysis provides for each parameter the change in RMS wavefront errors and underlines the most sensitive parameters. The criteria of the PSF Strehl ratio > 70% has been checked *a posteriori* on the worst case of a Monte Carlo simulation of 100 trials.

For tilts and decenters, tolerances have been computed with respect to the center of each mirror and not to its vertex. More precisely, the local coordinates system has the origin in the intersection between the chief ray of the central field with the optical surface, the local Z axis parallel to the ELT optical axis and X and Y axes parallel to the main directions of the mirror shape.

Details on the results are given in Table 3. In Figure 21, the nominal, the best and the worst cases over 100 Montecarlo simulations of the Strehl ratio map over the whole field of view at 1 micron are shown. The 3σ level worst case has a minimum Strehl ratio of 70.4%.

Table 3: Optical sensitivities for the Main Arm.

			min	max
MF1	radius of curvature	(mm)	lambda/10	lambda/10
(double pass)	decenter z	(mm)	-0,050	0,050
	decenter x	(mm)	-0,100	0,100
	decenter y	(mm)	-0,100	0,100
	tilt x	(degree)	-0,010	0,010
	tilt y	(degree)	-0,010	0,010
	tilt z	(degree)	-1,000	1,000
M1	radius of curvature	(mm)	-0,8	0,8
(parabolic)	conic constant		-0,001	0,001
	decenter z	(mm)	-0,100	0,100
	decenter x	(mm)	-0,100	0,100
	decenter y	(mm)	-0,100	0,100
	tilt x	(degree)	-0,010	0,010
	tilt y	(degree)	-0,010	0,010
	tilt z	(degree)	-0,010	0,010
MF2	radius of curvature	(mm)	lambda/10	lambda/10
	decenter z	(mm)	-0,100	0,100
	decenter x	(mm)	-0,100	0,100
	decenter y	(mm)	-0,100	0,100
	tilt x	(degree)	-0,010	0,010
	tilt y	(degree)	-0,010	0,010
	tilt z	(degree)	-1,000	1,000
MF3	radius of curvature	(mm)	lambda/10	lambda/10
	decenter z	(mm)	-0,100	0,100
	decenter x	(mm)	-0,100	0,100
	decenter y	(mm)	-0,100	0,100
	tilt x	(degree)	-0,010	0,010
	tilt y	(degree)	-0,010	0,010
	tilt z	(degree)	-1,000	1,000
M2	radius of curvature	(mm)	-0,1	0,1
(Aspheric)	conic constant		-0,001	0,001
	decenter z	(mm)	-0,050	0,050
	decenter x	(mm)	-0,050	0,050
	decenter y	(mm)	-0,050	0,050
	tilt x	(degree)	-0,010	0,010
	tilt y	(degree)	-0,010	0,010
	tilt z	(degree)	-0,010	0,010
M3	radius of curvature 1	(mm)	-0,2	0,2
(Toroidal)	conic constant 1		-0,001	0,001
	radius of curvature 2	(mm)	-0,2	0,2
	conic constant 2		-0,001	0,001
	decenter z	(mm)	-0,050	0,050
	decenter x	(mm)	-0,100	0,100
	decenter y	(mm)	-0,100	0,100
	tilt x	(degree)	-0,010	0,010
	tilt y	(degree)	-0,010	0,010
	tilt z	(degree)	-0,010	0,010
M4	radius of curvature	(mm)	-1,0	1,0
(Spherical)	decenter z	(mm)	-0,06	0,06

	decenter x	(mm)	-0,100	0,100
	decenter y	(mm)	-0,100	-0,100
	tilt x	(degree)	-0,050	-0,050
	tilt y	(degree)	-0,050	-0,050
	tilt z	(degree)	-0,050	-0,050
Detector	decenter x	(mm)	-0,100	0,100
	decenter y	(mm)	-0,100	0,100
	tilt x	(degree)	-0,100	0,100
	tilt y	(degree)	-0,100	0,100
compensator	decenter z	(mm)	-0,800	0,800

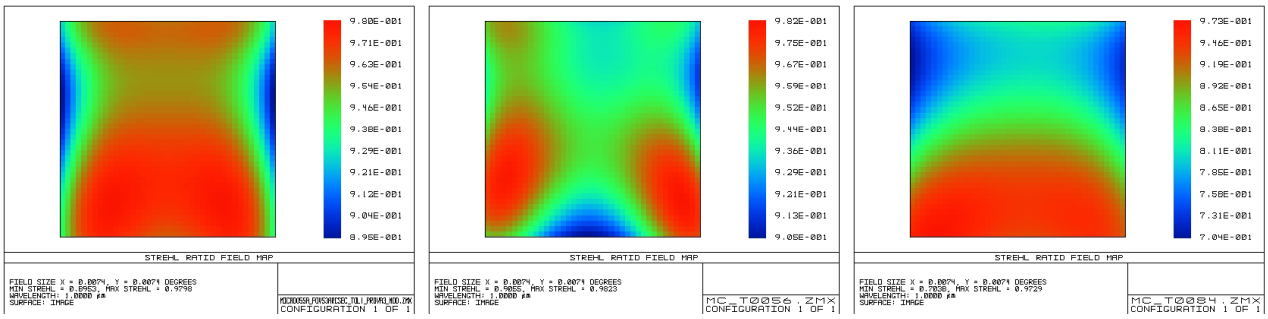

Figure 21: Strehl ratio map of the nominal, best and worst cases at 1 micron over the whole field of view.

4.2.3 Verification of Optical Quality with the SCAO Module

The SCAO module provides a corrected flat focal plane having size 127.88 mm (i.e. 2×2 detectors having a gap of 5 mm). The corresponding FoV is 25.91×25.91 arcsec^2. The optical quality for the main arm in this configuration has been verified.

The spot diagrams for the fields covering the 2×2 detectors FPA (rows) and wavelengths at 0.780, 1.615 and 2.450 μm (columns) are shown in Figure 22; the Strehl ratio over the entire field of view at the three wavelengths is shown in Figure 23. The worst value is 83.8%, i.e. the main channel is diffraction limited over the whole spectral range.

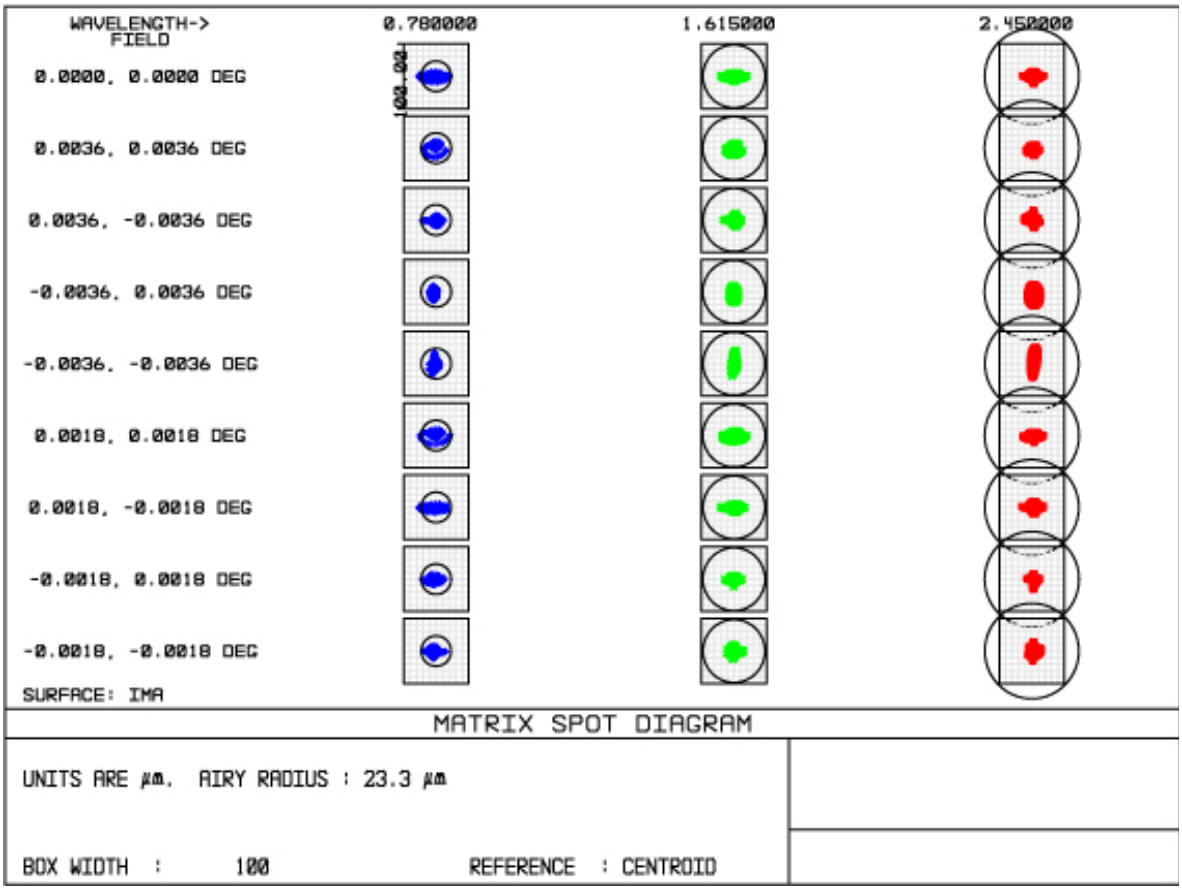

Figure 22: Spot diagrams for different wavelengths (columns) and different FOVs (rows). Circles represent the AIRY disk at the correspondent wavelength.

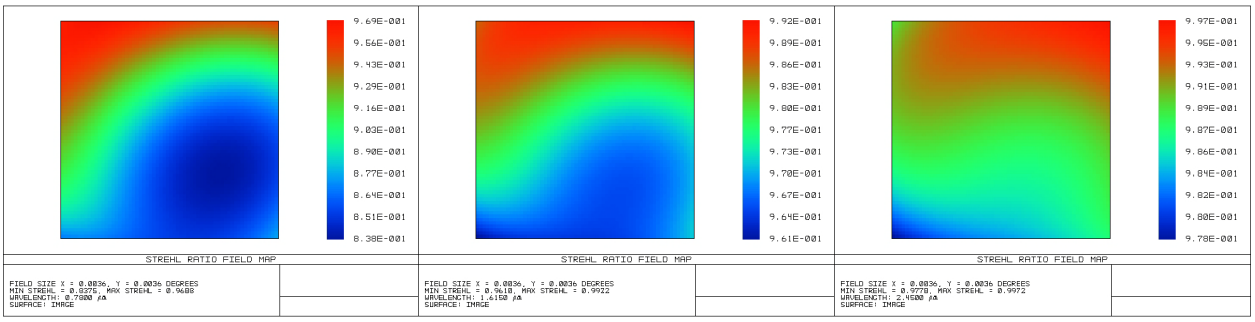

Figure 23: Strehl ratio map over the entire field of view at 0.780, 1.615 and 2.450 µm.

4.2.4 Conceptual Design of the Atmospheric Dispersion Corrector

Because of the wavelength depend refractive index of air, the observed altitude of a star varies with wavelength, thus smearing the stars image. This effect can be partially compensated with a so-called atmospheric dispersion corrector (ADC) made from two pairs of double prisms. Here we calculate how well this effect can be compensated with a classical ZnSe/ZnSe ADC. The ADC has been design as stand alone, independently by the main arm; the optical quality of the ELT+MAORY+ADC+MAINARM has been checked a posteriori. In the next phase, the optimization of the ADC will be included into the optimization of the camera performances.

The ADC has been assumed to be placed at about 500 mm in front of the ELT+MAORY focal plane. At this location the diameters of the ADC optical elements result to be about 300mm.

With reference to Figure 25, the ADC parameters are given in Table 4. The first and the last surfaces present toroidal shapes in order to correct the astigmatism introduced from the rather thick prisms in the convergent beam. The ADC has some residual axial chromatism (focus shift as function of wavelength) but it seems negligible over the single filters pass-bands. The focus shift on the entrance FP introduced by the ADC is expected to be compensated by the AO module (MAORY/SCAO). The expected dispersion correction performance in the J-band is shown in Figure 24 . The correction in H-band and K-band is similar.

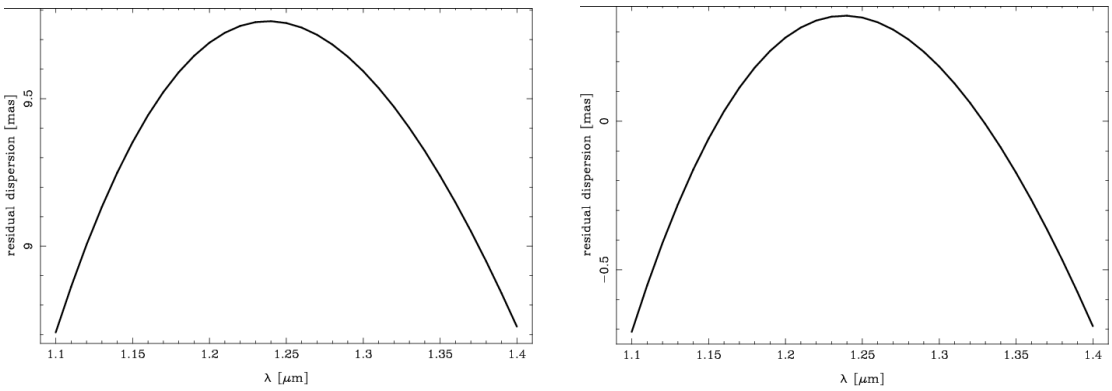

Figure 24: Residual dispersion vs. wavelength assuming a JHK-range ADC tuned to J-band (left) and residual dispersion vs. wavelength assuming an ADC specifically designed for J-band (right).

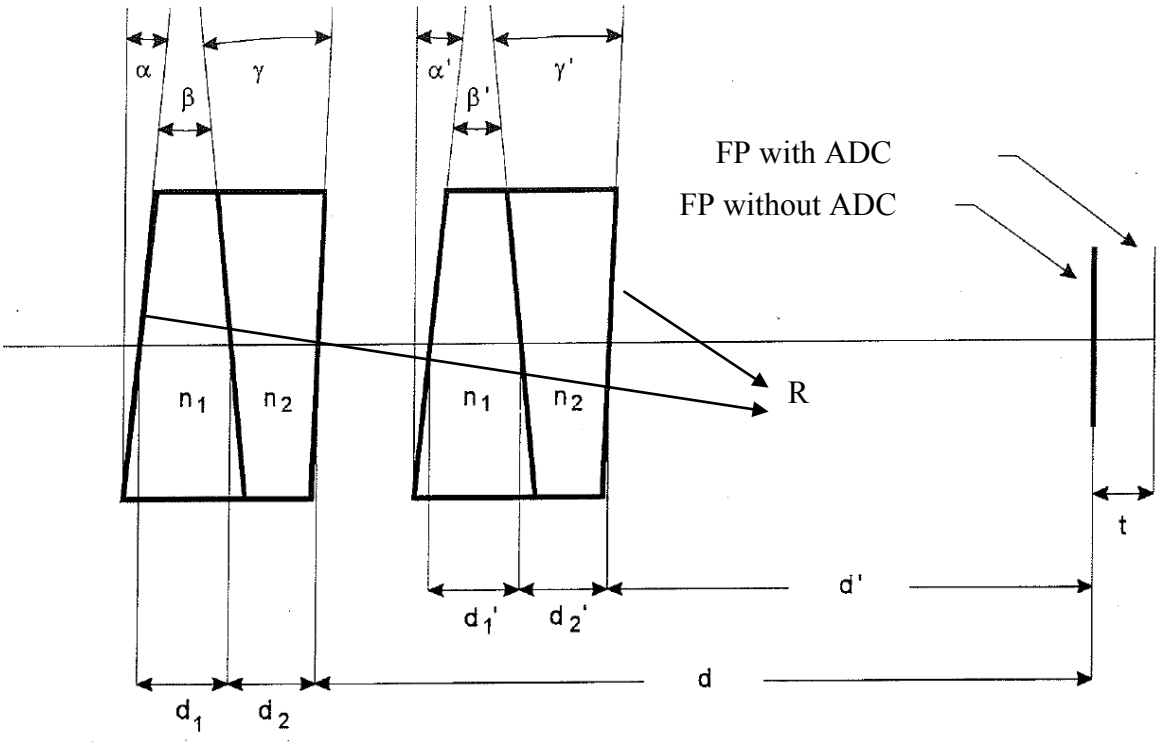

Figure 25: Scheme of the ADC.

Table 4: Main Parameters of the ADC.

d	505 mm	α	0 degree
d_1	30 mm	β	5,14816 degree
d_2	30 mm	γ	5,91493 degree
d'	435 mm	α'	-0,77192 degree
d_1'	30 mm	β'	5,45329 degree
d_2'	30 mm	γ'	6,22521 degree
cylinder radius of curvature R	471737 mm		
n_1	ZnSe		
n_2	ZnS		

The ADC has been inserted into the ELT+MAORY+MAIN ARM design, and the performances have been estimated through the Strehl ratio map in the H and K band (central and wings wavelength). The focus on the ELT+MAORY FP has been optimized for each band. The worst case in the H band 61.5% while it is 77.2% in the K band (see Figure 26).

Having the ADC in its current location is itself not optimal, we would prefer it to be near a pupil in the preceding AO system. This solution will be investigated in phase B.

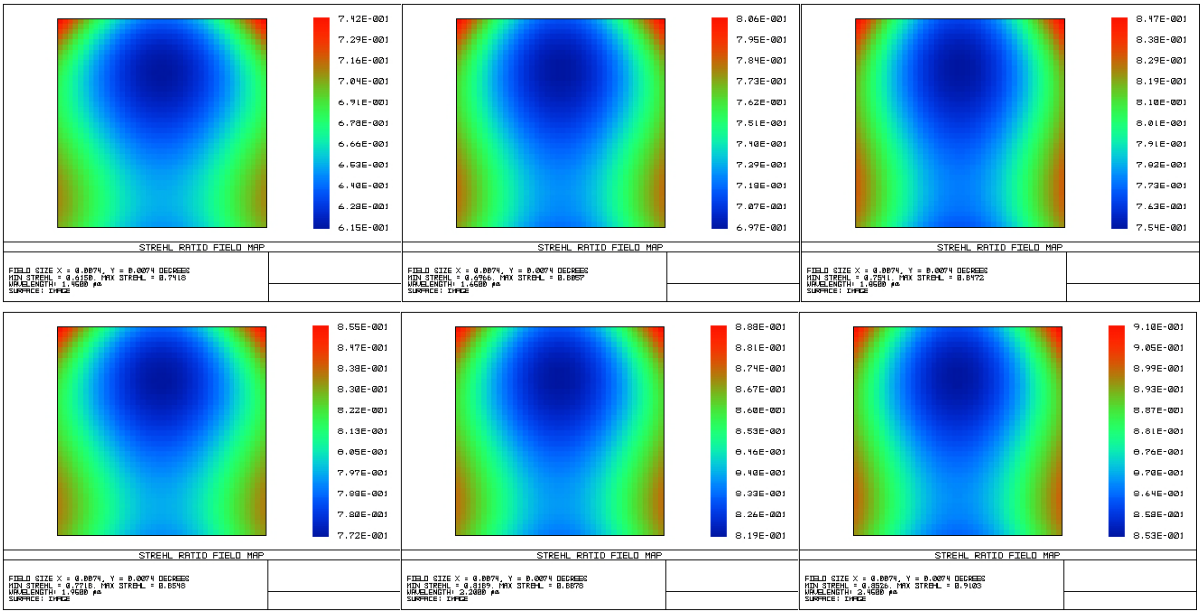

Figure 26: Strehl ratio map over the whole field of view for the H band (top) and K band (bottom).

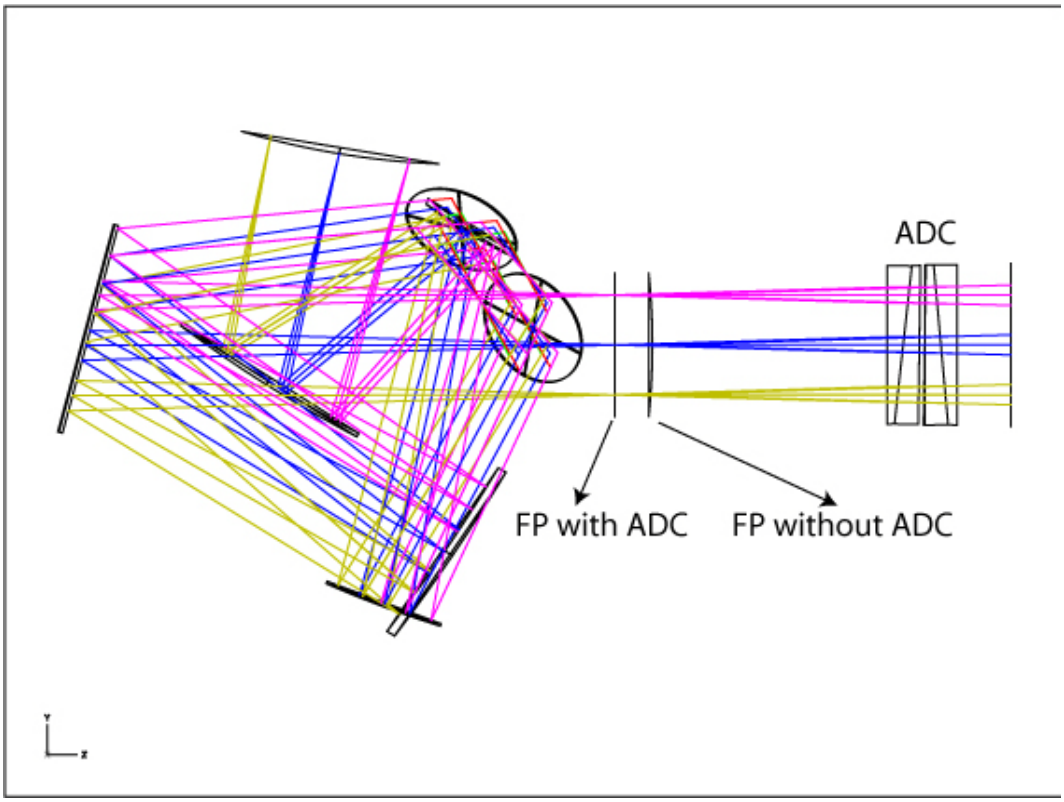

Figure 27: Layout of the ADC integrated in the main channel.

4.3 Auxiliary Arm Optical Design

The auxiliary arm will provide two focal plane samplings (4 mas/pixel and 1.5 mas/pixel) and spectroscopic capability (for the zoom mode 4 mas/pixel) exploiting the same detector. Both the zoom modes take advantage of a common off-axis parabolic mirror as collimator and, as camera, the first mode uses another off-axis parabolic mirror while the second mode uses a direct Ritchey-Chretien mirrors system.

The following design has referred to ELT+MAORY.

The optical layout is shown in Figure 28.

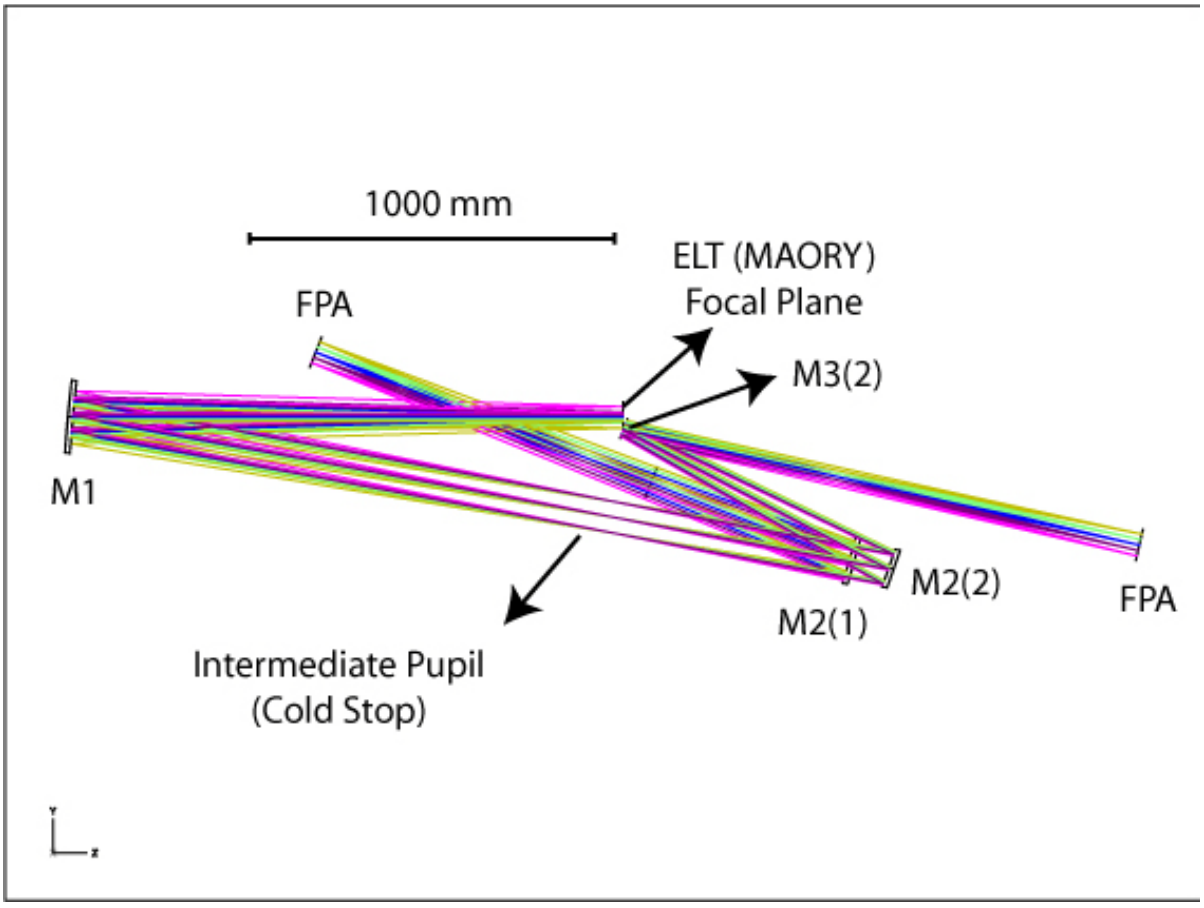

Figure 28: Optical layout of the working mirrors in the auxiliary arm.

The optical design characteristics are as follows:

M1: parabolic concave mirror

M2(1): parabolic concave mirror

M2(2): hyperbolic concave mirror

M3(3): hyperbolic convex mirror

The Focal Plane Array (FPA) is composed of a 4096^2 pixels, having a size of 15 μm. The resulting FPA has a size of 61.44 mm. The folding of the design has been made in order to use the same detector for both the zoom modes.

The optical design meets the required plate scale of 4mas/pixel for the first mode and 1.5mas/pixel for the second mode. The simulated FoV sizes are about 17.1×17.1 arcsec^2 and 6.4×6.4 arcsec^2 respectively (taking into account the field distortion).

The curvature of the FP supplied by MAORY does not deteriorate the quality at the auxiliary arm FP by placing a flat detector.

The common cold stop has 86.3 mm in diameter and it is located at the intermediate pupil.

The spot diagrams for the fields covering the whole FPA (rows) and wavelengths at 0.780, 1.615 and 2.450 μm (columns) for the first and second zoom mode are shown in Figure 29 and Figure 30 respectively; the Strehl ratio over the entire field of view at the three wavelengths for the first and second zoom mode are shown in Figure 31.

For the for zoom mode, the worst case is about 61% Strehl ratio at 0.780 μm that is largely better than the expected performance of MAORY at this wavelength. The worst case for the second zoom mode at the same wavelength is 89%, i.e. it is diffraction limited over the whole spectral range.

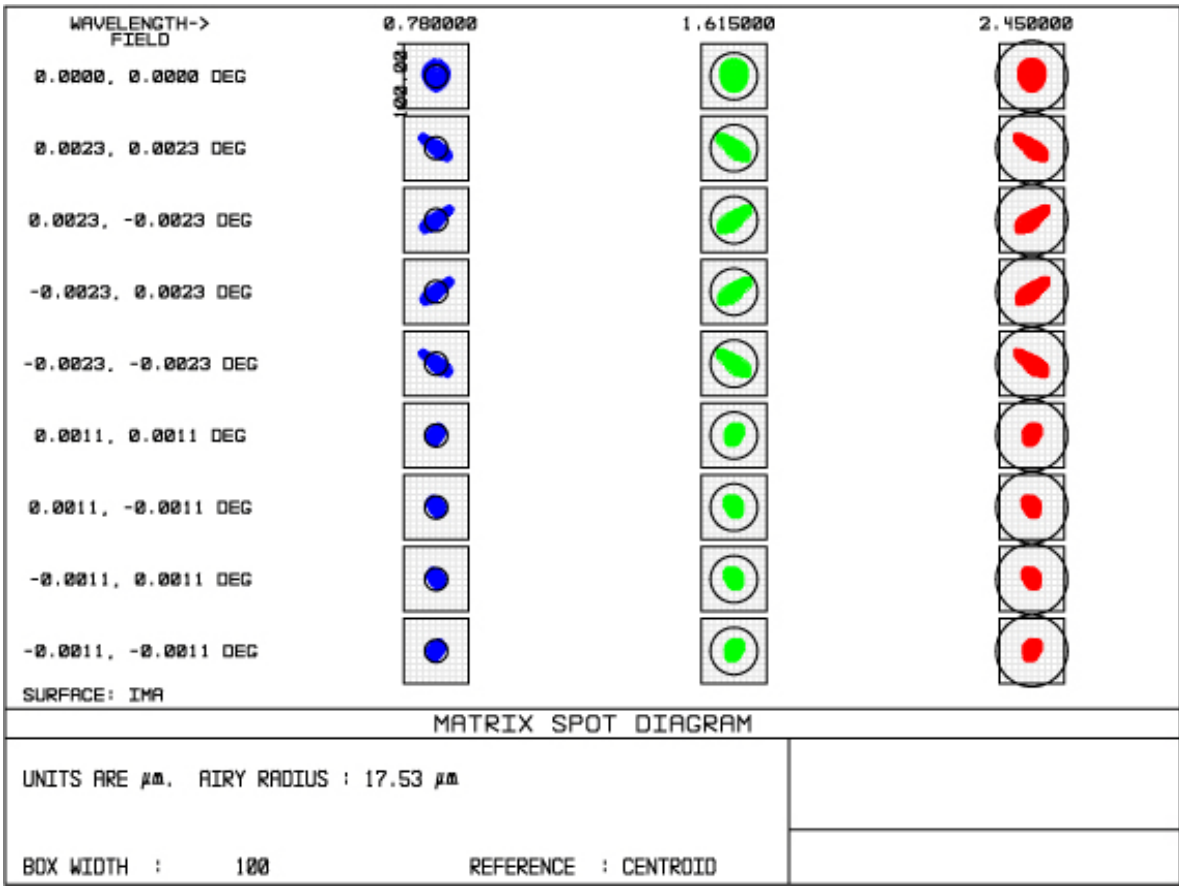

Figure 29: Spot diagrams for different wavelengths (columns) and different FOVs (rows) for the first zoom mode. Circles represent the AIRY disk at the correspondent wavelength.

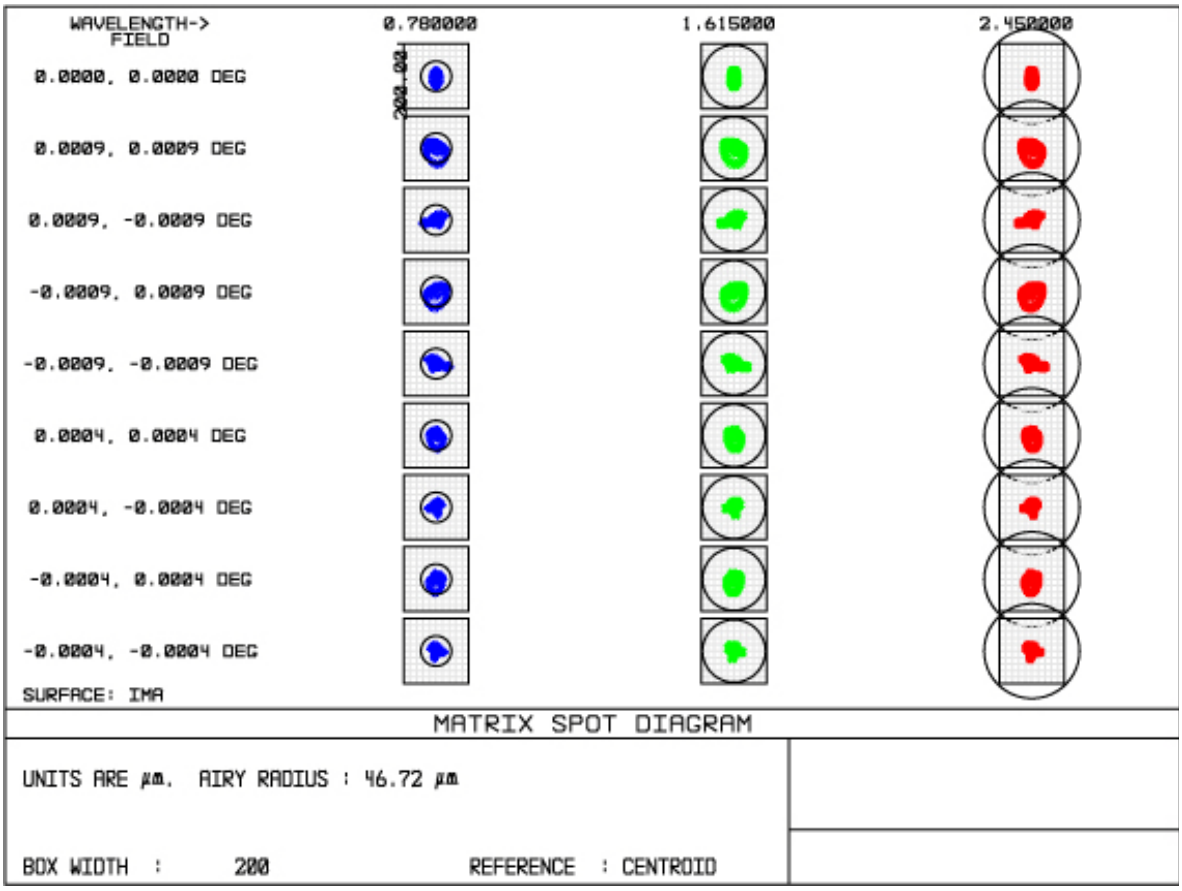

Figure 30: Spot diagrams for different wavelengths (columns) and different FOVs (rows) for the second zoom mode. Circles represent the AIRY disk at the correspondent wavelength.

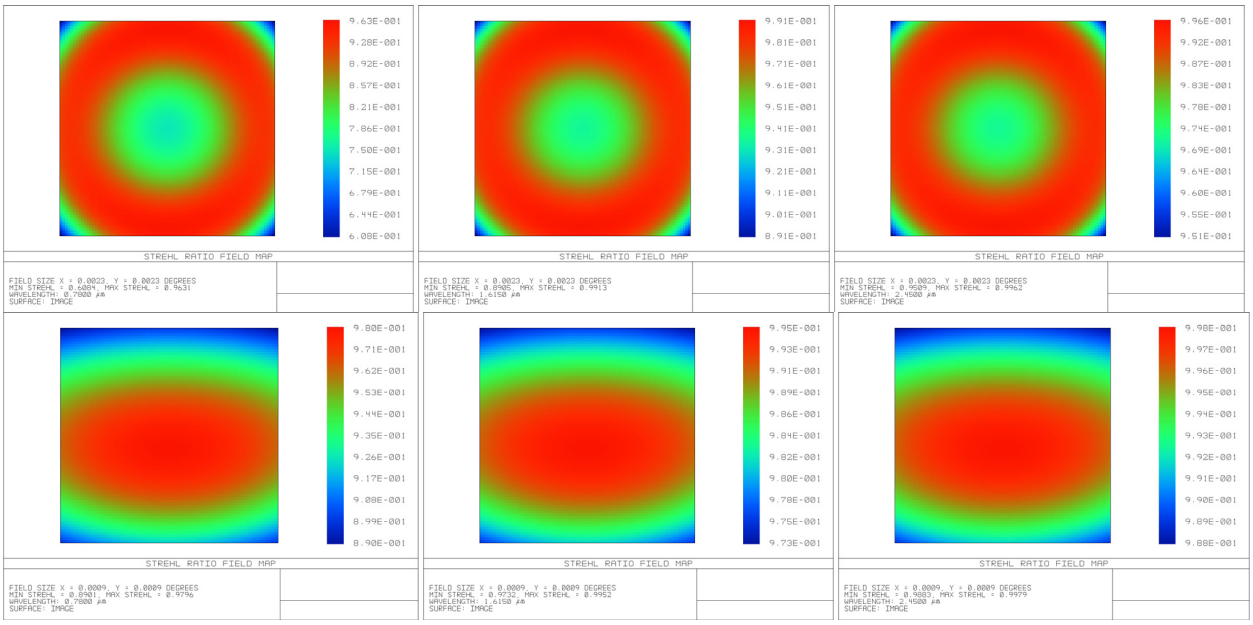

Figure 31: Strehl ratio map over the entire field of view at 0.780, 1.615 and 2.450 µm for the first zoom mode (top) and second zoom mode (bottom).

In Figure 32 the footprints of the beam at the common pupil image location for different off-axis fields are superimposed. The maximum circular aperture diameter is 86.3 mm. The shape of the cold is circular. The pupil shape varies with field position so cold stop must be undersized at 85.572 mm (i.e. all the light for the on-axis field is unvignetted). The maximum fraction of light blocked is 0.42% for corner field (worst case).

The distortion over the entire field of view has a maximum value of -0.39% and 0.03% for the first and second mode respectively. The grid distortion and the footprint over the detector surface are shown in Figure 33.

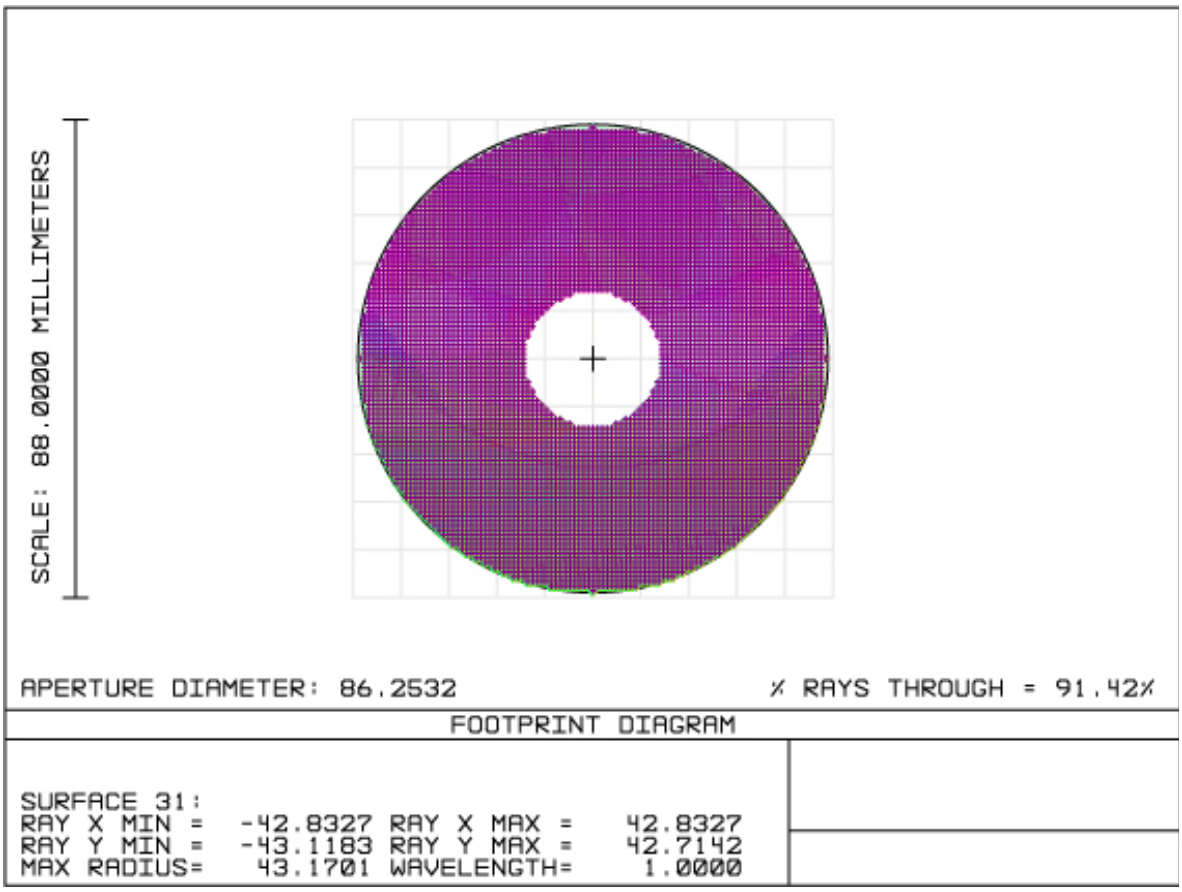

Figure 32: Footprint at the common cold stop.

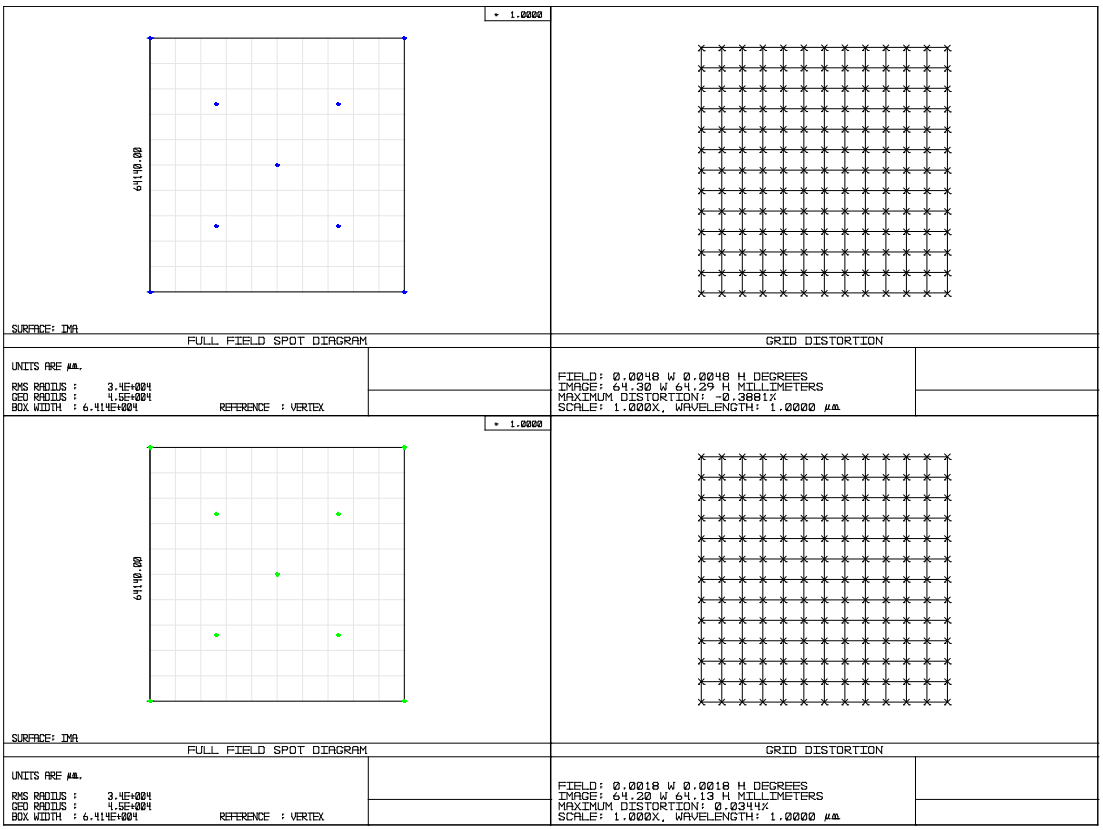

Figure 33: Footprint over the detector surface (left) and the grid distortion over the entire field of view (right) for the first (top) and second zoom mode (bottom).

The field curvature and the field distortions along two orthogonal field directions are shown in Figure 34 and Figure 35 for the first and second mode respectively.

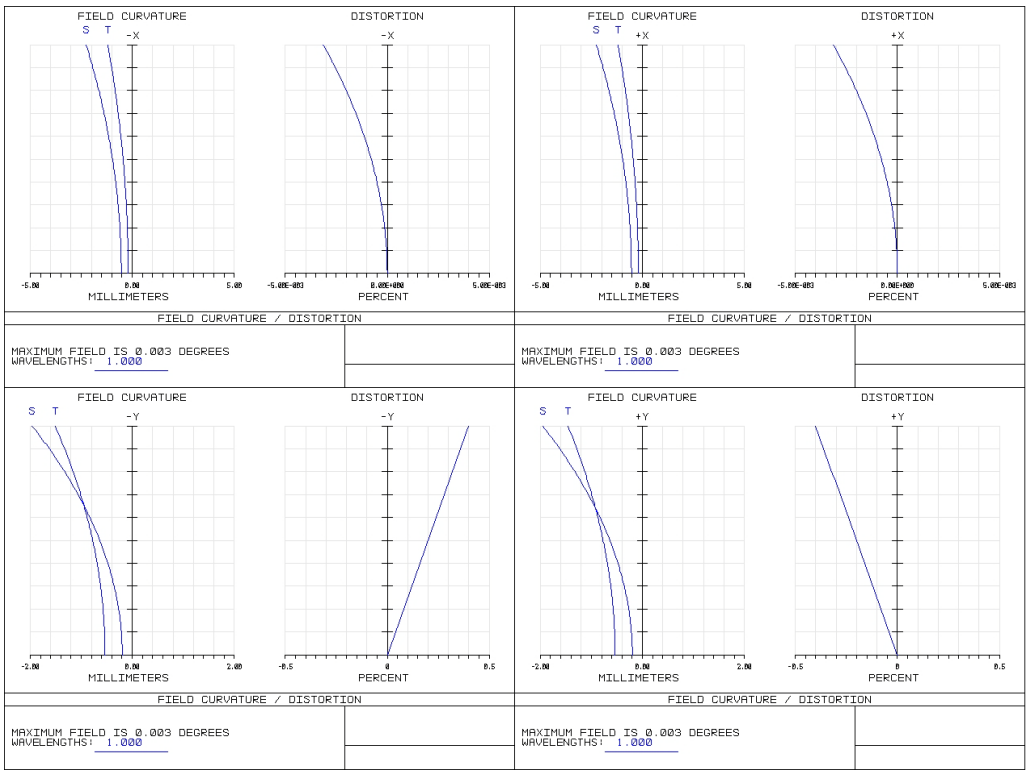

Figure 34: Field curvature (left curve) and absolute distorsion (right curve) vs. fields in different field directions (-x top left, +x top right, -y bottom left, +y bottom right) for first zoom mode.

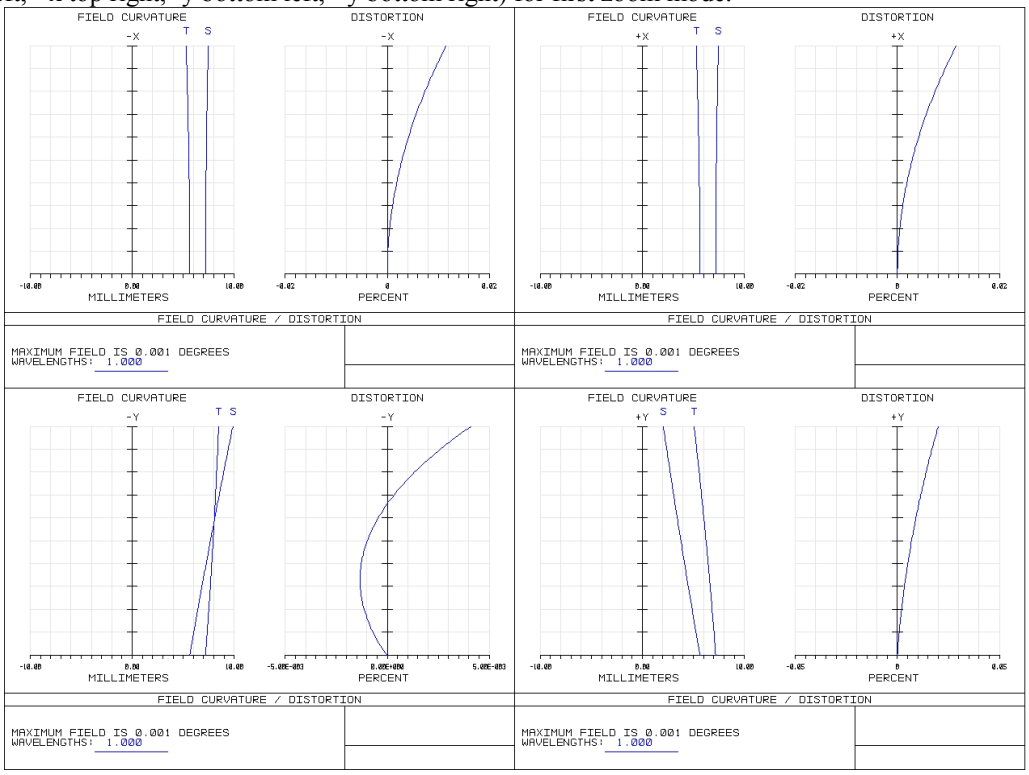

Figure 35: Field curvature (left curve) and absolute distorsion (right curve) vs. fields in different field directions (-x top left, +x top right, -y bottom left, +y bottom right) for second zoom mode.

4.3.1 Auxiliary Arm Folding and Mirror Parameters

The auxiliary arm has been folded in order to have a common entrance optical bench with the main arm (collimator), to allow the accommodation of a dedicated filter wheel(s) and to have a separate optical bench for the two cameras with a common detector.

The switch between the main arm and the auxiliary arm is allowed thanks to the insertion of the auxiliary arm collimator (M1) on the common optical path.

The layout of the folded auxiliary arm is shown in Figure 36. The radiation incoming from the entrance focal plane has a first reflection on the double-pass fold mirror MF1, the same used for the main arm. The auxiliary arm selection has done through the insertion of the collimator M1 th0at reflect the radiation back toward MF1 till the second fold mirror MF2. All these mirrors lay on the same optical bench (that mounts also the main arm collimator M1 and fold mirror MF2). The intermediate pupil is formed between the fold mirror MF2 and MF3, and in this position will be allocated the cold stop and the filters and grisms wheel. The fold mirror MF3 feeds the two cameras (zoom modes). The first zoom mode has compound by an off-axis parabolic mirror (M2(1)) and by a fold mirror MF4(1). The second zoom mode has compound by a Ritchey-Chretien mirror system (M2(2) and M3(2)) and by a couple of fold mirrors (M4(2) and M5(2)) that allow the radiation to reach the same detector of the first zoom mode. To switch between the first and the second zoom mode, it is necessary to move out from the beam the parabolic mirror M2(1) and to insert the fold mirror M5(2) and vice versa. A 3D image of the folded main channel is shown in Figure 20.

The main parameters for all the mirrors are given in

Table 5. In the Table, the vertex to center distance has been computed assuming as mirror center the intersection between the chief ray of the on-axis field of view and the mirror surface. The positions of the mirrors have been given in global vertex coordinates assuming a coordinate reference linked to the ELT focal plane.

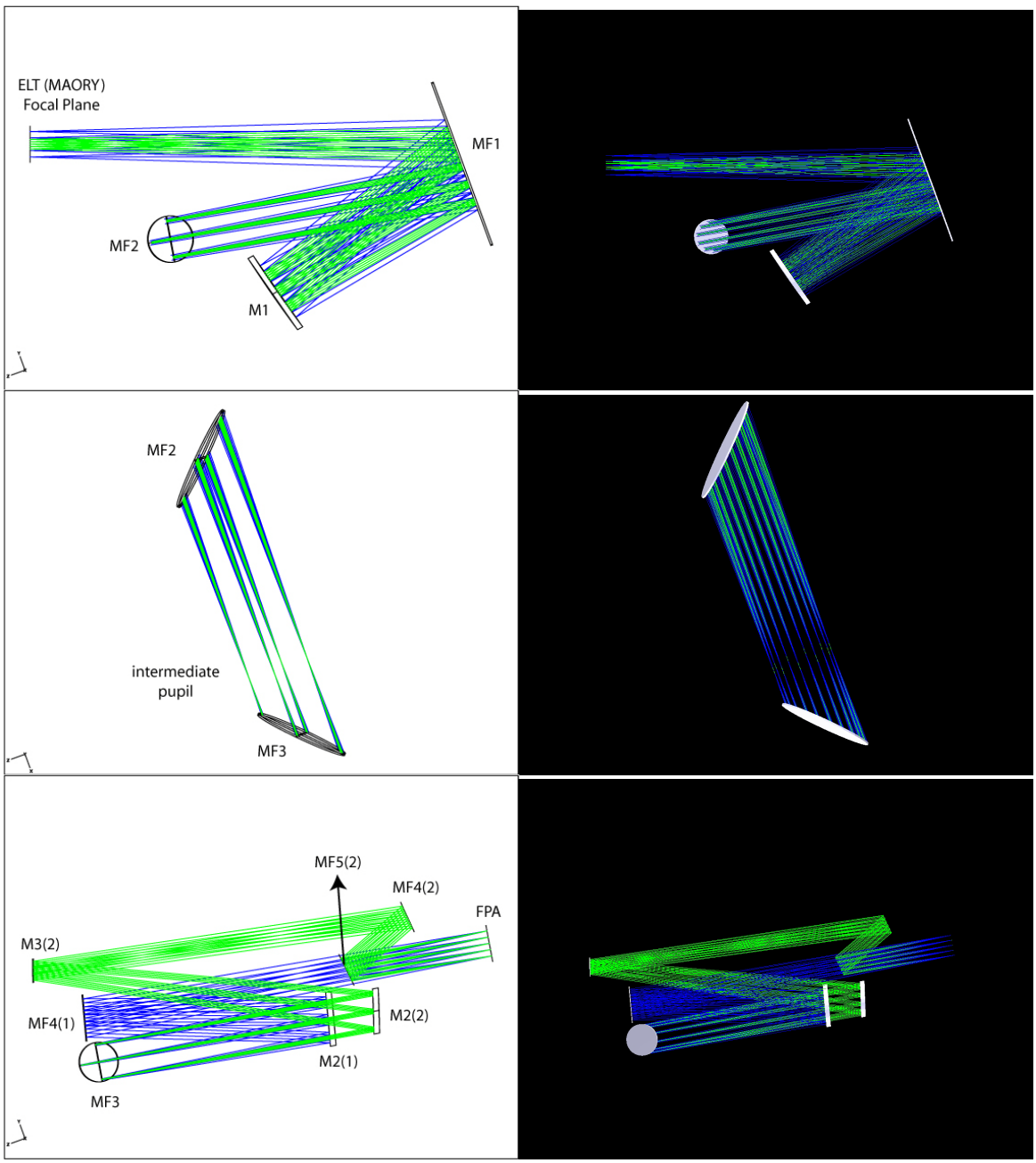

Figure 36: Layout of the folded auxiliary channel. Collimator optical bench (top), cold stop position (middle) and camera optical bench (bottom). The zoom mode 1 rays are in blue while the zoom mode 2 in green.

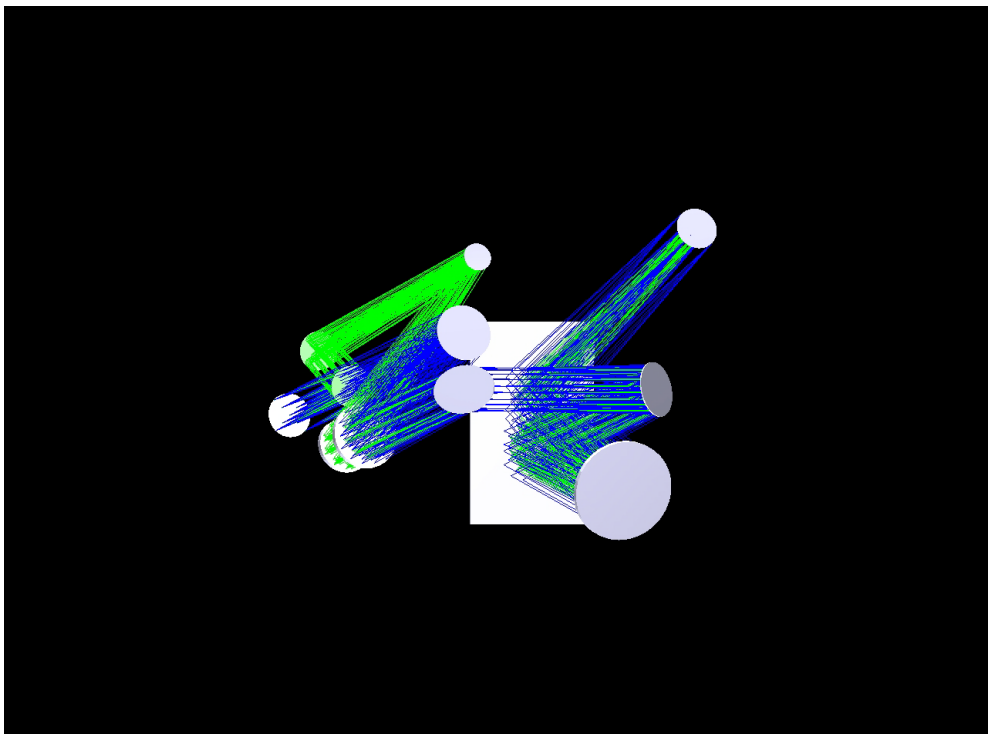

Figure 37: 3D layout of the folded auxiliary channel.

Table 5: Main parameters (upper) and global vertex coordinates (lower) for the auxiliary arm optical elements.

	R mm	K	Aperture Shape	Clear Aperture mm × mm	Vertex/Center mm
MF1	infinity	-	rectangular	260×380	-
M1	-3000.000	-1	circular	200	-275
MF2	infinity	-	elliptical	148×108	-
MF3	infinity	-	elliptical	132×96	-
M2(1)	-3119.689	-1	circular	130	-297
MF4(1)	infinity	-	circular	112	-
M2(2)	-2459.474	-1.0168	circular	108	-375.7
M3(2)	-1221.144	-2.1639	circular	56	-115.8
MF4(2)	infinity	-	circular	78	-171.2
MF5(2)	infinity	-	circular	82	-178.4
FPA	infinity	-	rectangular	64× 64	-

	Tilt X degree	Tilt Y degree	Tilt Z degree	Decenter X mm	Decenter Y mm	Decenter Z mm
ELT Focal Plane	0	0	0	0	0	0
MF1	15.000	0	0	0	50.000	-980.000
M1	29.500	0	0	0	-108.703	-425.190
MF2	10.500	-45.000	0	0	-220.045	-325.382
MF3	169.500	-45.000	-180.000	401.955	-220.045	-325.382
M2(1)	179.588	0	-180.000	401.955	177.722	-836.453
MF4(1)	-174.956	0	-180.000	401.955	-112.918	-191.271
M2(2)	-169.500	0	-180.000	401.955	258.662	-846.877
M3(2)	-173.934	0	-180.000	401.955	113.041	-63.001
MF4(2)	-155.373	0	-180.000	401.955	267.941	-897.186
MF5(2)	-154.249	0	-180.000	401.955	145.264	-744.351
FPA	-169.5	0	180.000	401.955	49.112	-1065.505

4.3.2 Auxiliary Arm Tolerance Analysis

A preliminary tolerance analysis has been performed using as a merit function the PSF Strehl ratio > 70% at wavelength 1 micron. A list of parameters have been defined corresponding to the errors in positioning (tilts and decenters) and manufacturing for all the mirrors. All the mirrors are assumed to be independent. The location of the detector has been assumed to be adjustable to the best focus position, allowing one to relax the tolerances.

The sensitivity analysis provides for each parameter the change in RMS wavefront errors and underlines the most sensitive parameters. The criteria of the PSF Strehl ratio > 70% has been checked *a posteriori* on the worst case of a Monte Carlo simulation of 100 trials.

For tilts and decenters, tolerances have been computed with respect to the center of each mirror and not to its vertex. More precisely, the local coordinates system has the origin in the intersection between the chief ray of the central field with the optical surface, the local Z axis parallel to the ELT optical axis and X and Y axes parallel to the main directions of the mirror shape.

Details on the results are given in Table 6. In Figure 38, the nominal, the best and the worst cases over 100 Montecarlo simulations of the Strehl ratio map over the whole field of view at 1 micron are shown for the first and the second zoom mode. The 3σ level worst case has minimum Strehl ratios of 71.0% and 78.6% for first and the second zoom mode respectively.

Table 6: Optical sensitivities for the Auxiliary Arm.

			min	max
MF1	radius of curvature	(mm)	lambda/10	lambda/10
(double)	decenter z	(mm)	-0,050	0,050
	decenter x	(mm)	-0,500	0,500
	decenter y	(mm)	-0,500	0,500
	tilt x	(degree)	-0,010	0,010
	tilt y	(degree)	-0,010	0,010
	tilt z	(degree)	-1,000	1,000
M1	radius of curvature	(mm)	-0,4	0,4
(parabolic)	conic constant		-0,001	0,001
	decenter z	(mm)	-0,100	0,100
	decenter x	(mm)	-0,100	0,100
	decenter y	(mm)	-0,100	0,100
	tilt x	(degree)	-0,010	0,010
	tilt y	(degree)	-0,010	0,010
	tilt z	(degree)	-0,010	0,010
MF2	radius of curvature	(mm)	lambda/10	lambda/10
	decenter z	(mm)	-0,100	0,100
	decenter x	(mm)	-0,100	0,100
	decenter y	(mm)	-0,100	0,100
	tilt x	(degree)	-0,010	0,010
	tilt y	(degree)	-0,010	0,010
	tilt z	(degree)	-1,000	1,000
MF3	radius of curvature	(mm)	lambda/10	lambda/10
	decenter z	(mm)	-0,100	0,100
	decenter x	(mm)	-0,100	0,100
	decenter y	(mm)	-0,100	0,100
	tilt x	(degree)	-0,010	0,010
	tilt y	(degree)	-0,010	0,010
	tilt z	(degree)	-1,000	1,000
M2(1)	radius of curvature	(mm)	-0,4	0,4
(parabolic)	conic constant		-0,001	0,001
	decenter z	(mm)	-0,050	0,050
	decenter x	(mm)	-0,100	0,100
	decenter y	(mm)	-0,100	0,100
	tilt x	(degree)	-0,010	0,010
	tilt y	(degree)	-0,010	0,010
	tilt z	(degree)	-0,010	0,010
MF4(1)	radius of curvature	(mm)	lambda/10	lambda/10
	decenter z	(mm)	-0,050	0,050
	decenter x	(mm)	-0,100	0,100
	decenter y	(mm)	-0,100	0,100
	tilt x	(degree)	-0,010	0,010
	tilt y	(degree)	-0,010	0,010
	tilt z	(degree)	-1,000	1,000
M2(2)	radius of curvature	(mm)	-0,2	0,2
hyperbolic	conic constant		-0,001	0,001
	decenter z	(mm)	-0,100	0,100
	decenter x	(mm)	-0,100	0,100
	decenter y	(mm)	-0,100	0,100

	tilt x	(degree)	-0,010	0,010
	tilt y	(degree)	-0,010	0,010
	tilt z	(degree)	-0,010	0,010
M3(2)	radius of curvature	(mm)	-0,4	0,4
hyperbolic	conic constant		-0,001	0,001
	decenter z	(mm)	-0,100	0,100
	decenter x	(mm)	-0,100	0,100
	decenter y	(mm)	-0,100	0,100
	tilt x	(degree)	-0,010	0,010
	tilt y	(degree)	-0,010	0,010
	tilt z	(degree)	-0,010	0,010
MF4(2)	radius of curvature	(mm)	lambda/10	lambda/10
	decenter z	(mm)	-0,100	0,100
	decenter x	(mm)	-0,100	0,100
	decenter y	(mm)	-0,100	0,100
	tilt x	(degree)	-0,010	0,010
	tilt y	(degree)	-0,010	0,010
	tilt z	(degree)	-1,000	1,000
MF5(2)	radius of curvature	(mm)	lambda/10	lambda/10
	decenter z	(mm)	-0,100	0,100
	decenter x	(mm)	-0,100	0,100
	decenter y	(mm)	-0,100	0,100
	tilt x	(degree)	-0,010	0,010
	tilt y	(degree)	-0,010	0,010
	tilt z	(degree)	-1,000	1,000
Detector	decenter x	(mm)	-0,100	0,100
	decenter y	(mm)	-0,100	0,100
	tilt x	(degree)	-0,100	0,100
	tilt y	(degree)	-0,100	0,100
compensator	decenter z	(mm)	-2,000	2,000

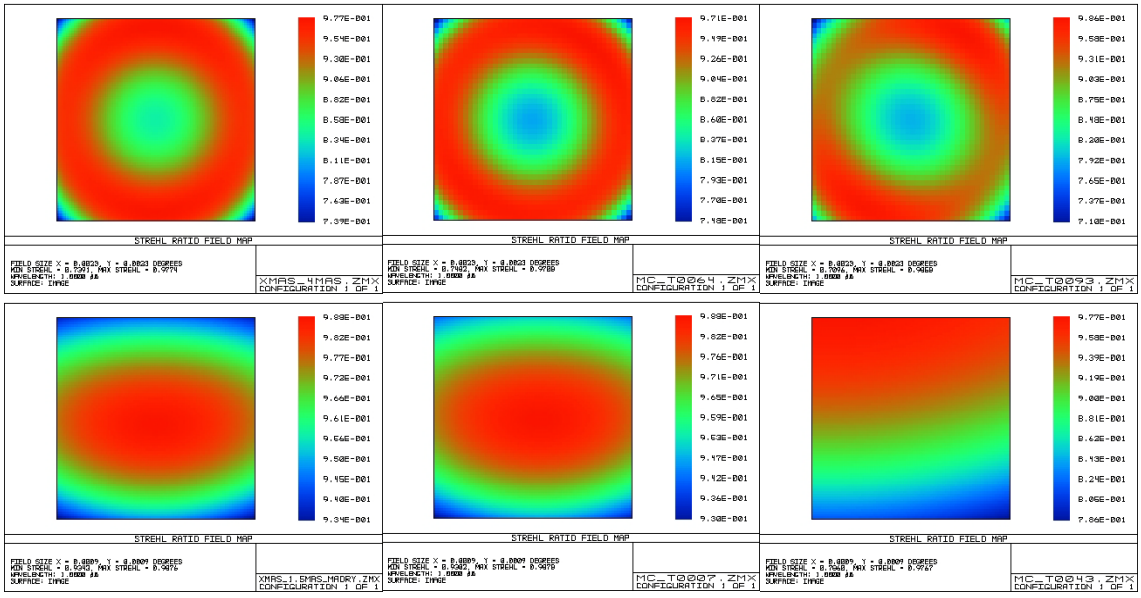

Figure 38: Strehl ratio map of the nominal, best and worst cases at 1 micron over the whole field of view for the first (top) and second zoom mode (bottom).

4.3.3 Verification of Optical Quality with the SCAO Module

The SCAO module provides to the auxiliary arm a corrected flat focal plane over the whole FoV. The optical quality for the main arm in this configuration has been verified.

The spot diagrams for the fields covering the whole FPA (rows) and wavelengths at 0.780, 1.615 and 2.450 μm (columns) for the first and second zoom mode are shown in Figure 29 and Figure 30 respectively; the Strehl ratio over the entire field of view at the three wavelengths for the first and second zoom mode are shown in Figure 31.

For the for zoom mode, the worst case is about 77.8% Strehl ratio at 0.780 μm that is largely better than the expected performance of SCAO module at this wavelength. The worst case for the second zoom mode at the same wavelength is 81.7%, i.e. it is diffraction limited over the whole spectral range.

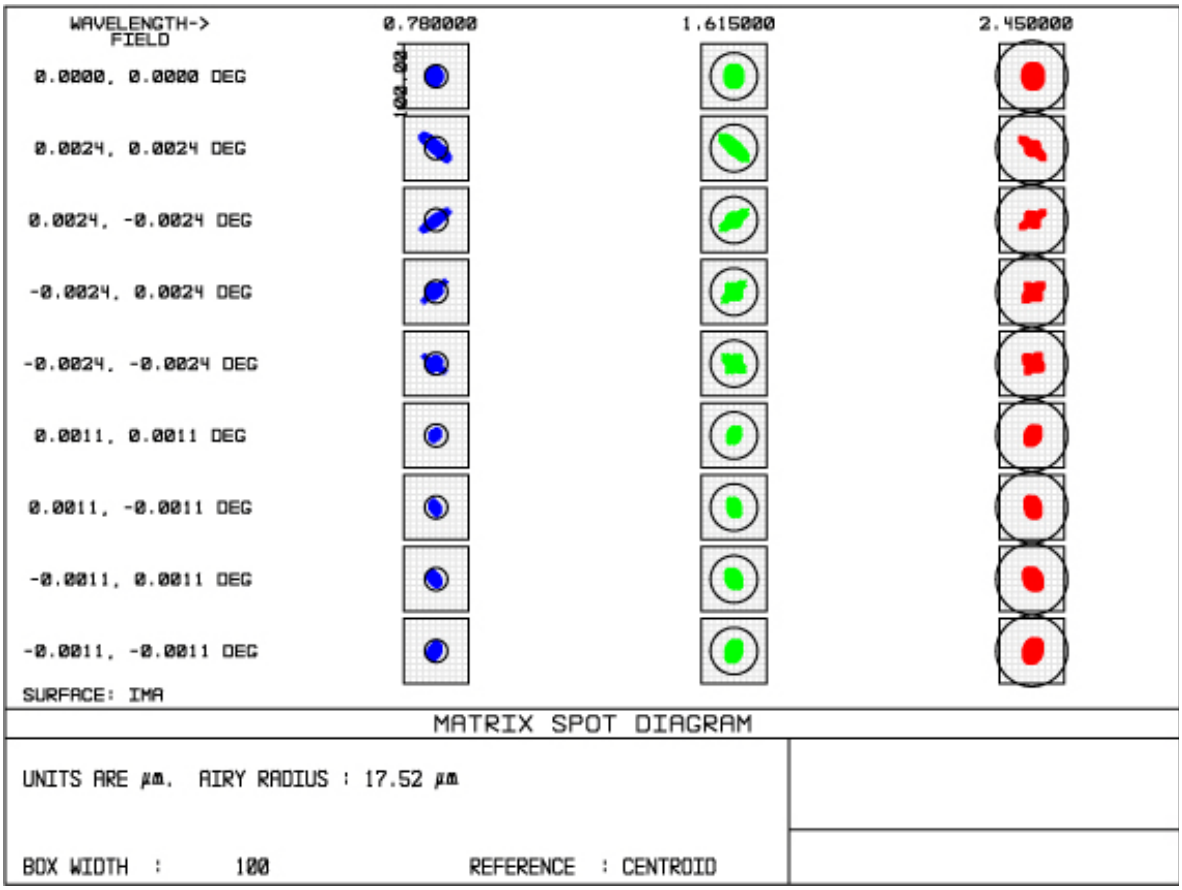

Figure 39: Spot diagrams for different wavelengths (columns) and different FOVs (rows) for the first zoom mode. Circles represent the AIRY disk at the correspondent wavelength.

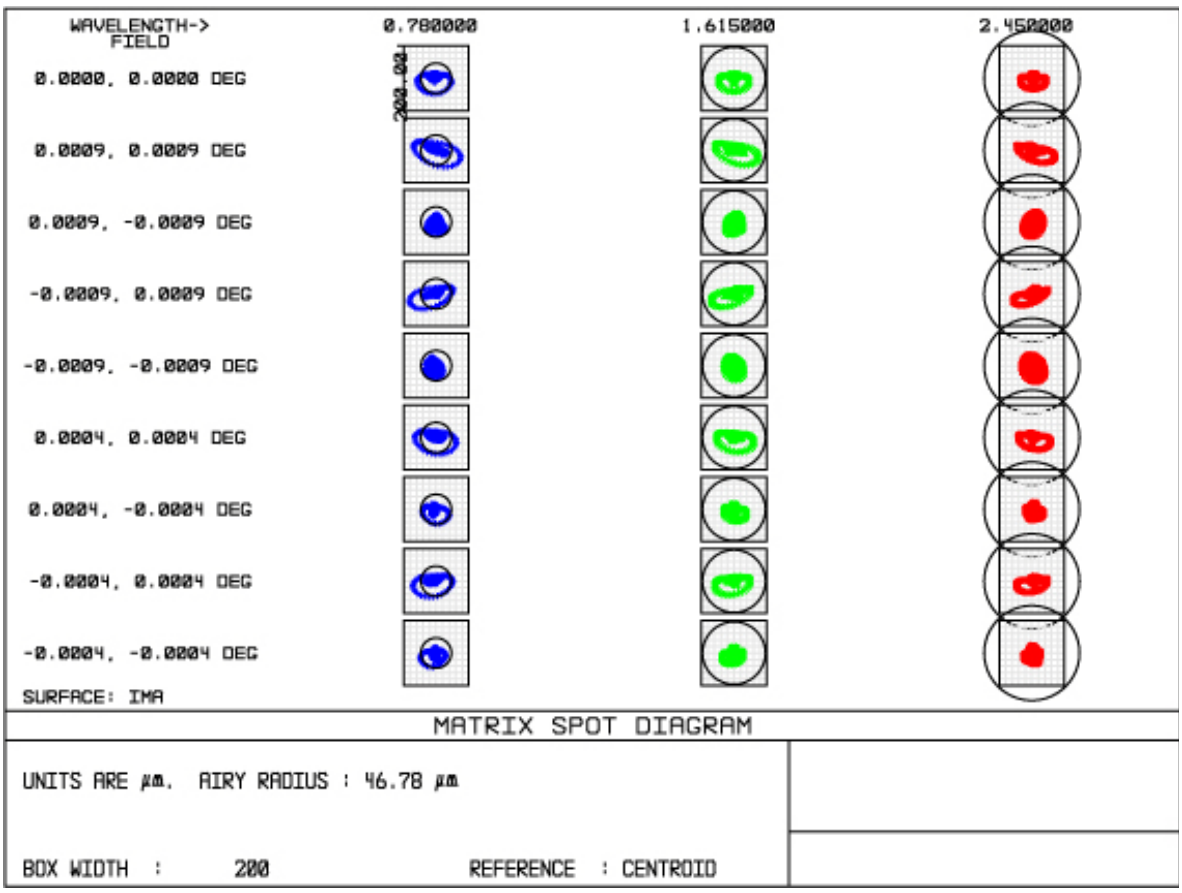

Figure 40: Spot diagrams for different wavelengths (columns) and different FOVs (rows) for the second zoom mode. Circles represent the AIRY disk at the correspondent wavelength.

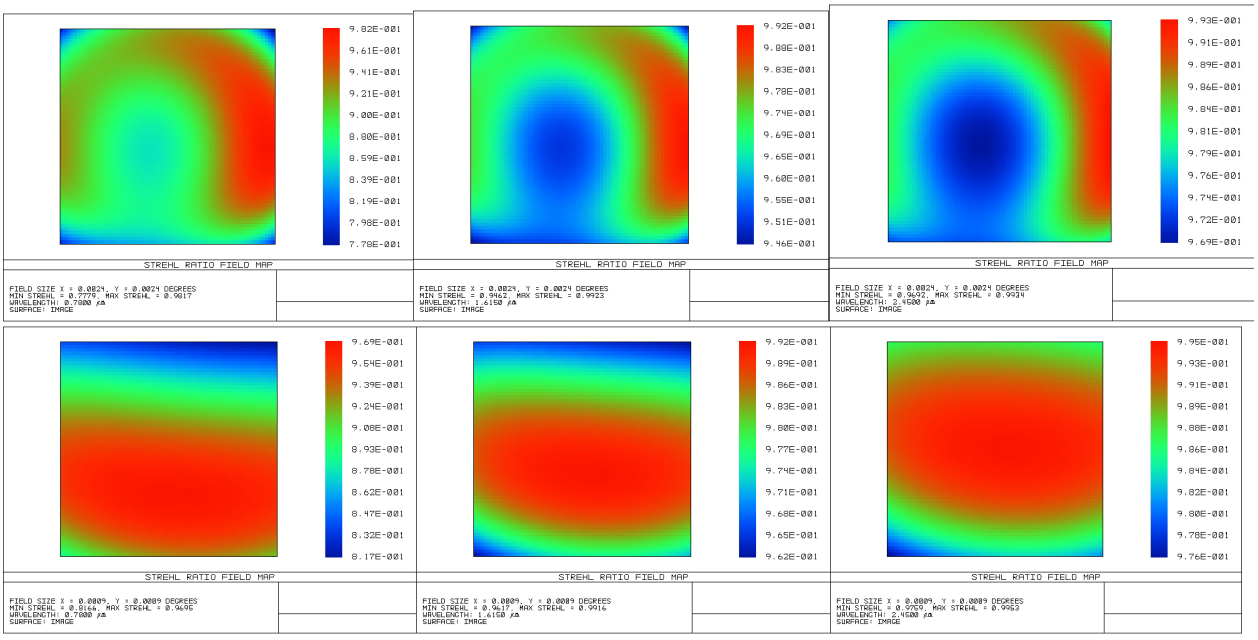

Figure 41: Strehl ratio map over the entire field of view at 0.780, 1.615 and 2.450 µm for the first zoom mode (top) and second zoom mode (bottom).

4.3.4 Auxiliary Arm Spectroscopic Mode

The auxiliary arm in the first zoom mode has to provide spectroscopic capability. The required resolution is R=3000-5000 over the full spectral range with a slit width of 12 mas (i.e. 3 pixels). Preliminary simulations have been carried out based on grisms as dispersion elements. These elements can be located in the filters wheel (near the intermediate pupil; the current solution) or in a dedicated wheel (see Figure 42). The grism materials normally used for K band are KRS5 (can be directly ruled, high transmission, high refractive index), Si and Ge (high transmission, high refractive index, but technical problems in direct ruling) and ZnSe (can be directly ruled, transmission ~80%, high refractive index). For the simulations, we have selected ZnSe. The whole spectral range has been divided into 4 sub-spectral bands covered each one by a dedicated grism. The grism parameters are given in Table 7.

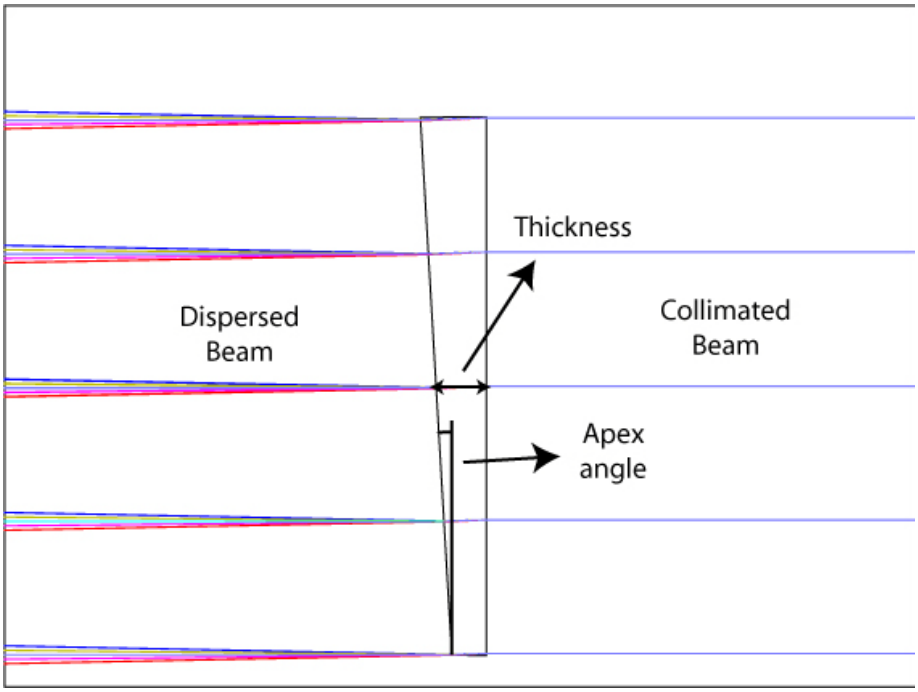

Figure 42: Grism location near the intermediate pupil.

Table 7: Grisms parameters.

	Wavelength bands	Material	Thickness (mm)	Diameter (mm)	Apex angle (degree)	Line /micron	Theoretic resolution
Grism1	I-z	ZnSe	8	90	2.98	0.080	3000
Grism2	y-J	ZnSe	8	90	3.11	0.070	3000
Grism3	H	ZnSe	8	90	4.35	0.067	4000
Grism4	K	ZnSe	8	90	4.44	0.051	4000

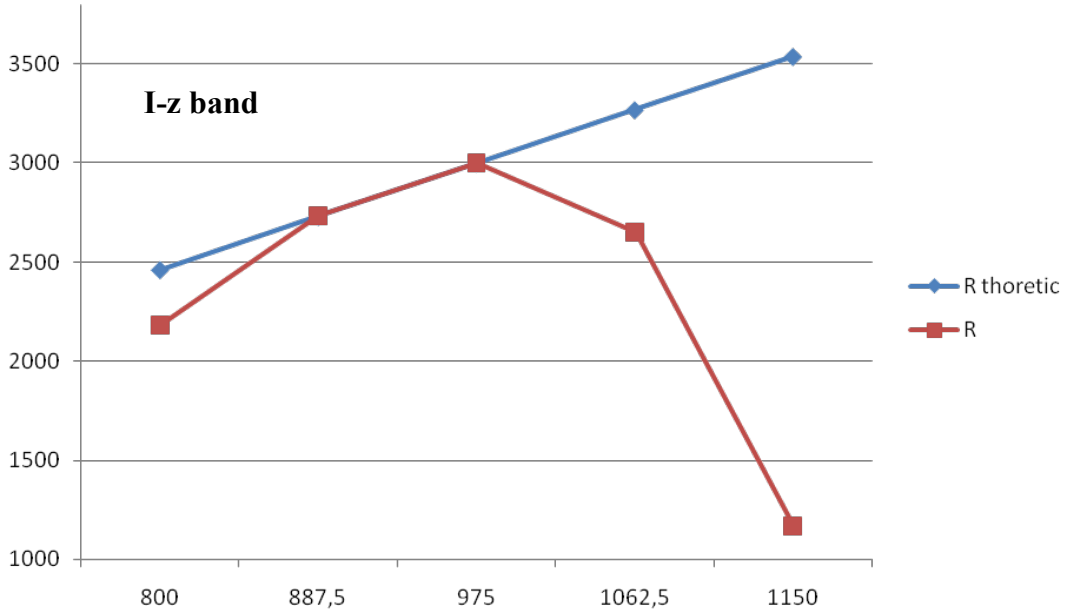

Figure 43: Resolution vs wavelength in the i-Z band.

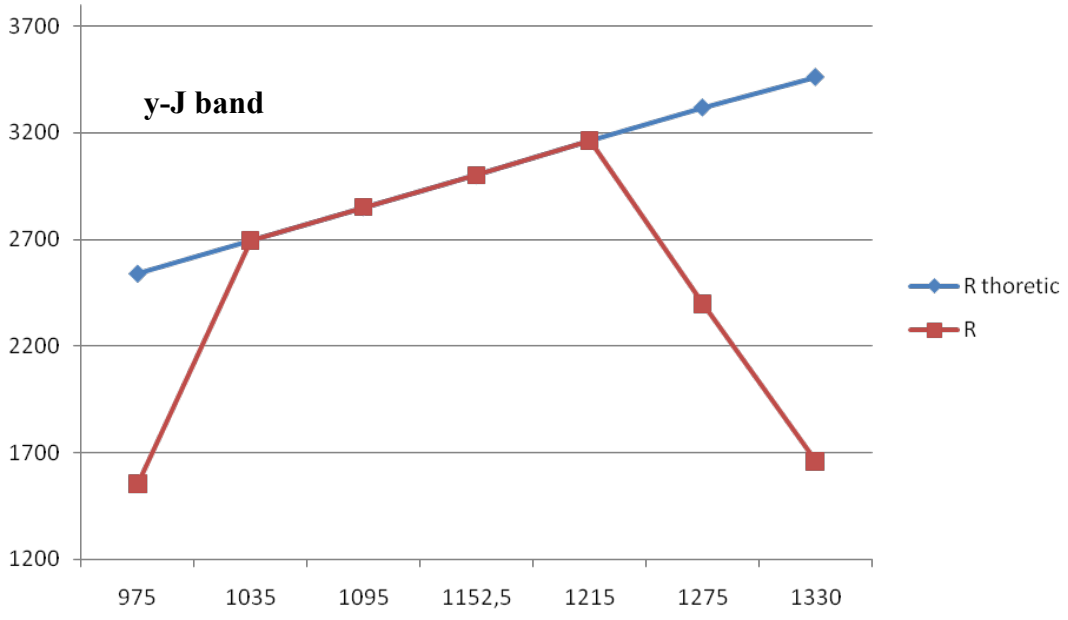

Figure 44: Resolution vs wavelength in the y-J band.

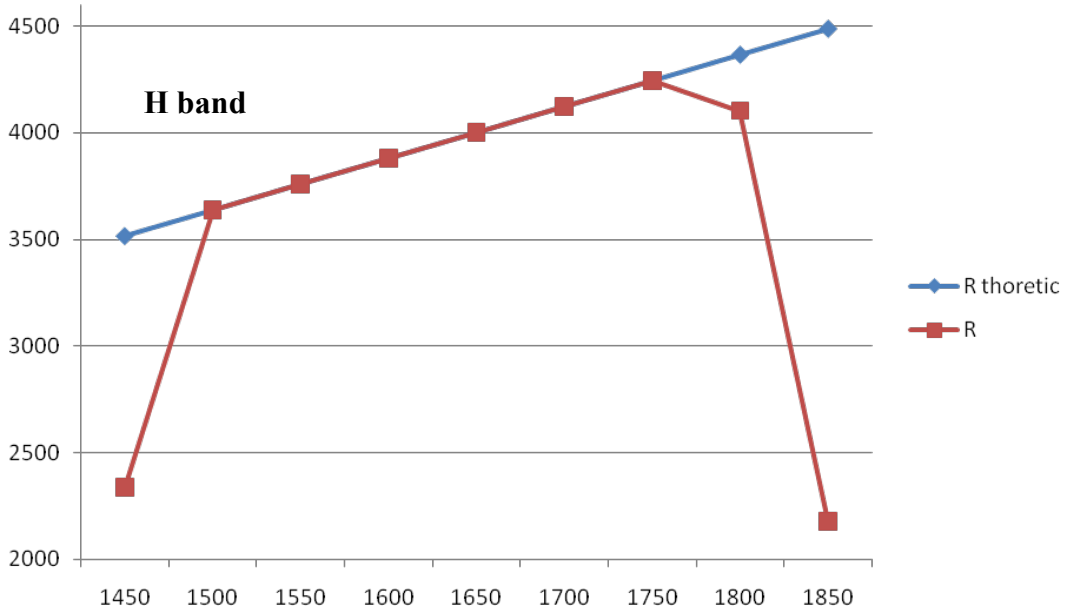

Figure 45: Resolution vs wavelength in the H band**.**

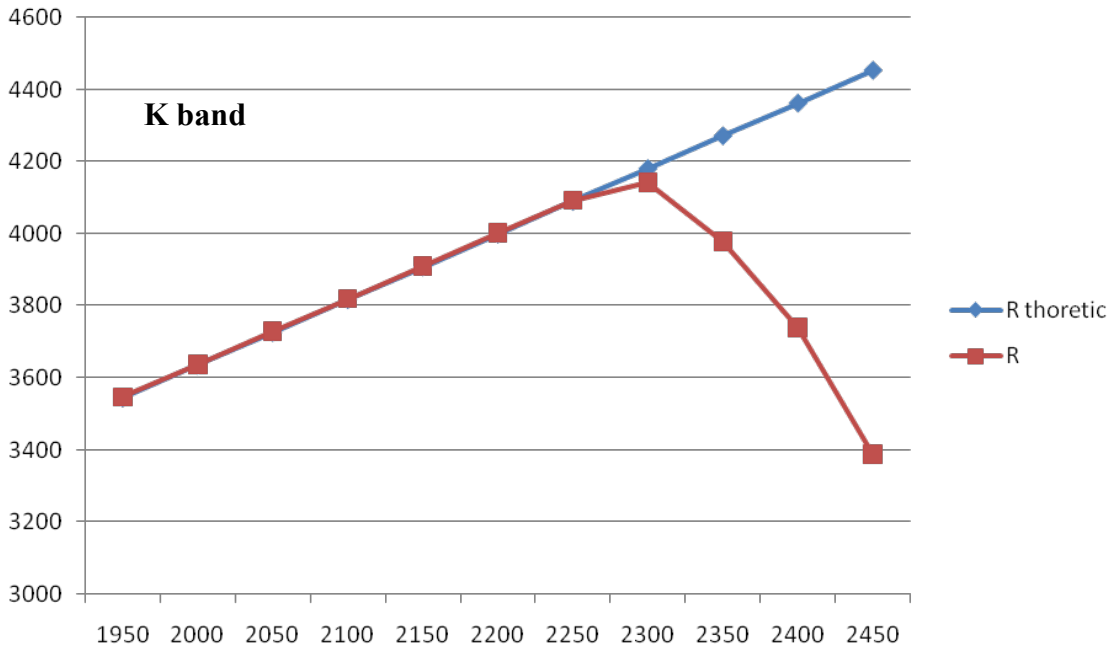

Figure 46: Resolution vs wavelength in the K band.

In Figure 43, Figure 44, Figure 45 and Figure 46 are shown the simulated resolutions for the four bands respectively of four representative cases. For the first two bands the camera optical quality restricts the resolution with a range of about 1500 to 3000. For the second two bands the resolution can be improved to 2500-4000 with the limitation mainly given by the diffraction size of the PSF. This result has been considered acceptable by the science team. If a higher resolution is required the bands can be divided further or the camera performance can be improved (Ritchey-Chretien configuration)

In case of poor performance of MAORY or slightly extended sources, a slit having width 48mas (16 pixel) is foreseen. In this case the resolution is determined only by the slit size being the optical quality of the camera much better. The resolutions that can be achieved are 1100 for K band, 900 for H band, 750 for y-J band and 500 for I-z band.

4.4 Calibration Unit

For the calibration of the instrument, internal (calibration unit, Figure 47) and external (sky) sources are used. So far the internal calibration is foreseen for flat-field and PSF measurements, and wavelength calibration. The calibration unit is located outside the MICADO cryostat, nearby the telescope focus, on the same optical bench as the SCAO module.

When the calibration unit is used together with the MAORY module, the beam must be additionally folded to fit the agreed design volume available within MAORY (the details of the folding scheme will be addressed in Phase B).

An integrating sphere from Labsphere is used as illumination source. It includes arc-lamps for the wavelength calibration and flat-field lamps to measure the pixel-to-pixel gains. The intensity of the lamps can be adjusted.

At the output (~50mm diameter) of the sphere, a filter wheel with 6 positions is mounted. It is driven by a DC motor, e.g. Faulhaber 3257 024CR with gear (i=25), equipped with an encoder on the output shaft. Besides an open port, it holds neutral density and other filters, corresponding to the requirement of measurements in different bands.

A projection system consisting of 2 lenses made of fused silica (Infrasil) and a mirror creates an image of the sphere exit on the simulated focal plane. The 2 lenses system is necessary to deliver the same F/# as the telescope beam.

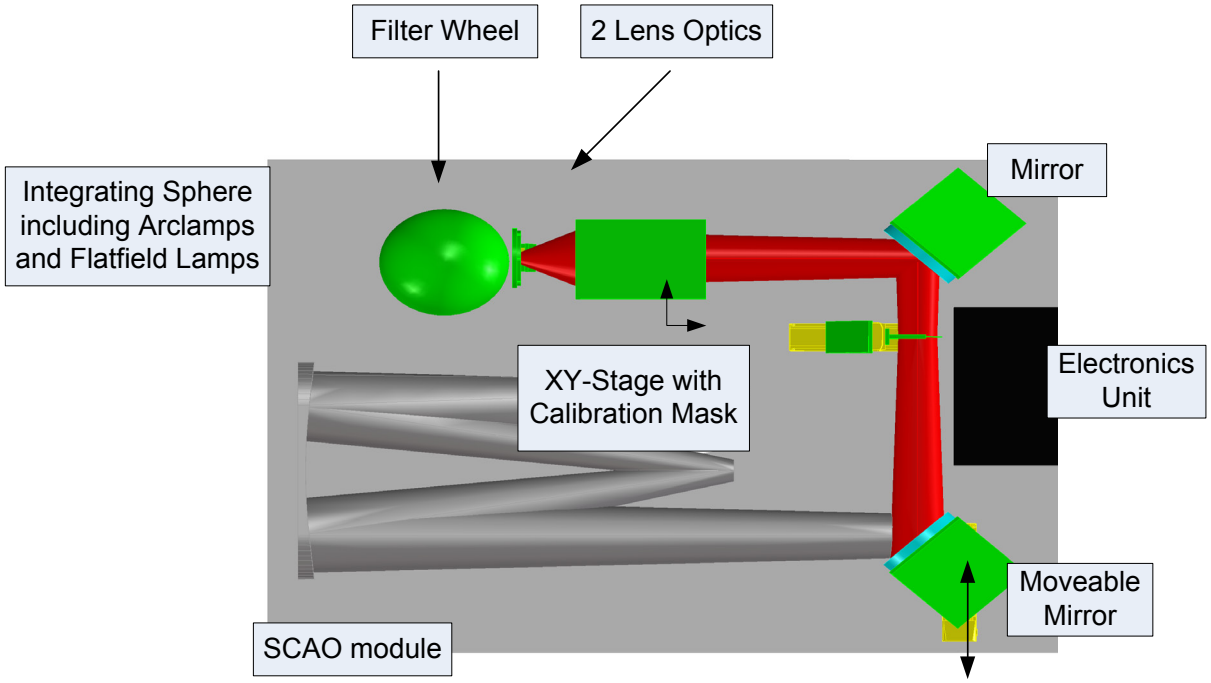

Figure 47: Basic design and location of the MICADO calibration unit

An exchangeable mask mounted on a xy-stage can be moved into the focus of the calibration unit. It will be used for astrometry calibrations, estimation of PSFs and the measurements of instrument distortions. The xy-stage is consisting of 2 linear stages from PI, a M-531 and a M-511 drive for the movement in x- and y-direction, respectively. Both stages have DC motors without gear and linear encoders with reference. The calibration mask can be manufactured using optical lithography to create holes with a diameter of 10-50µm and a position accuracy of 40nm in a 100nm thick chrome layer. The substrate would be quartz glass with a thickness of ~3mm.

To switch between the telescope beam and the beam of the calibration unit, a movable mirror is used. The mirror is mounted on a linear stage (M-531) from PI.

The electronics for the calibration unit is located nearby the components on the same optical bench. It supplies and regulates the lamps of the sphere, controls the filter wheel and the linear stages of the mask and the movable mirror.

4.5 Advanced Filter Design

There is considerable room for improvement in the (already good) performance on MICADO using advanced filter designs. This includes high throughput broad and narrow band filters, as well as OH suppressing filters:

Broad band filters: the near-IR filters used in GROND, an instrument for optical and near-IR ground based follow-up of gamma-ray bursts, each have an mean transmission of 98% and sharp long and short wavelength cutoffs (see Günster et al. 2008, SPIE, 7101, 71011).

OH suppressing filters: the possible gains one can achieve using interference filters to suppress OH emission lines was known already more than a decade ago (Offer & Bland-Hawthorn, 1998, MNRAS, 299, 176). Since then, improvements in technology have made such filters a realistic option.

To address both of these in the context of MICADO we have initiated a research project with Laser Zentrum Hannover. The initial step of this is to design and manufacture a small prototype set of filters for the J-band. The broad-band filter consists of separate low-pass and high-pass filters, coating opposite sides of a substrate in order to reduce the bending stress that occurs with thick single-side coatings. As shown in Figure 48, the mean transmission of the combined filter is about 98%. Short wavelength suppression continues to 0.7μm (consistent with the cutoff from the optical/IR dichroic in the AO systems), while long wavelength suppression extends to 2.5μm (consistent with the detector cutoff).

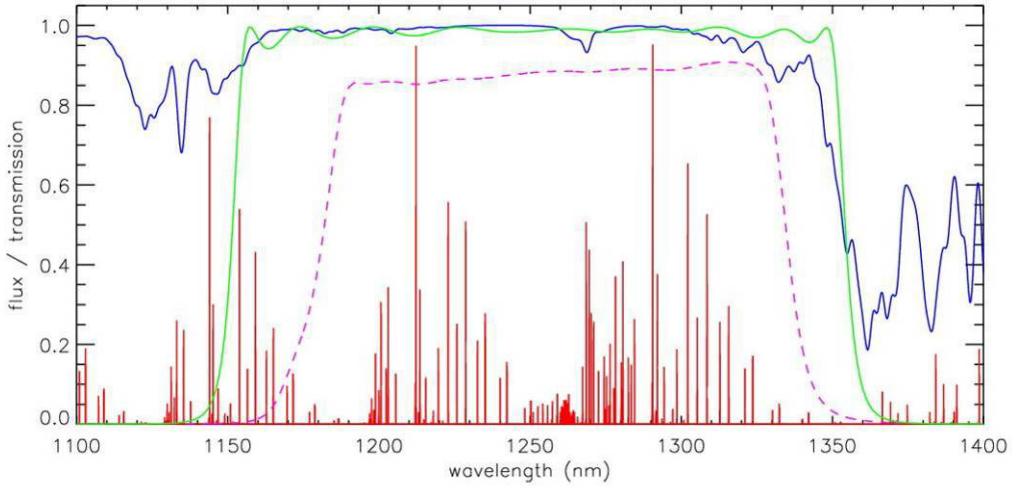

Figure 48: comparison of the J-band filter developed by LZH (solid green curve) and that used in HAWK-I (dashed magenta curve). The LZH bandpass has a higher throughput, leading to improved sensitivity, and steeper edges. For comparison, the atmospheric transmission is shown in blue and the scaled background (including continuum, OH lines, and O_2 lines) is in red.

Three options for simple OH suppression (in effect mimicking the narrow bandpasses already identified by Offer & Bland-Hawthorn 1998) have also been developed. This filter will be used as a coating for both sides of a second substrate which would be used in parallel (perhaps mounted in the same filter wheel slot) with the new J-band filter. When combined together, the total throughput is as shown in Figure 49. We note that because the background is considerably reduced, it will take loner to reach background limited performance. With the HAWK-I filter, the background is ~6e-/sec; with the new filter set, this is reduced to 0.5e-/sec. As a result individual exposure times have to be increased: typically from a few seconds to 30-60sec.

These filters described here yield an increase in the signal-to-noise of a factor 1.3 – equivalent to 0.3mag greater depth or reaching the same signal-to-noise in only 60% of the integration time. This is already a substantial saving of telescope time.

In order to verify the filter characteristics at cryogenic temperatures, and to assess the lifetime of the filters, we will procure 2.5cm diameter prototypes in the near future.

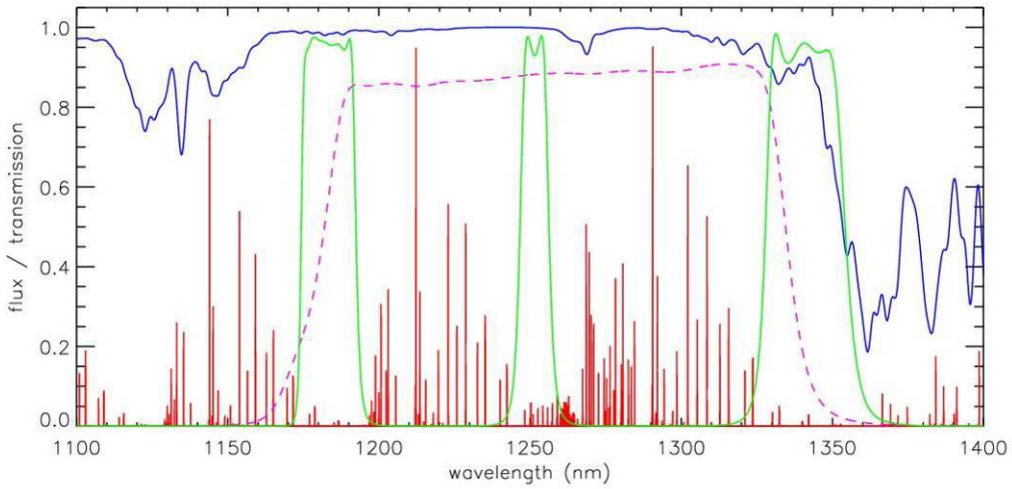

Figure 49: total throughput of the combined J-band and OH suppressing filters designed by LZH (solid green lines): in effect this comprises several narrow bandpasses within the J-band, where there are very few emission lines. For comparison, also shown are the HAWK-I J-band filter (dashed, magenta), the atmospheric transmission (blue) and the scaled background (red).

There is considerable potential for future development. The research project with LZH therefore contains a longer (~2year) development, which will address the following issues:

Optimisation of filter design: the filter described above is very simple; more complex filters which can have many more narrow bandpasses require a far more sophisticated optimisation method (e.g. based on genetic algorithms, using the definition of the filter layers as input and the signal-to-noise as output). This is particularly important for the H-band.

Process: because the filters will inevitably be thick (perhaps up to 50µm), careful control and optimisation of the deposition process must be achieved. The process must be stable for the long time periods (hours) required to build up these extreme filter thicknesses.

Homogeneity: typical substrate sizes are 25mm, while the requirement for a MICADO pupil filter would be 100mm diameter. In order to maintain the exact bandpass across this diameter, high homogeneity is required. Currently about 0.5% can be guaranteed over 50mm; this needs to be improved to 0.1% over 100mm. This can be achieved by a variety of techniques. In increasing complexity these are (i) installation of a shadowing mask, (ii) integration of a simple planetary rotation system, (iii) installation of full planetary rotation, together with adaption of the on-line optical monitoring system.

Coating Stress: a mismatch between the substrate and mechanical stress will induce surface bending and distort the wavefront. In addition, adhesion and thermal properties of the coating will be influenced by the dense layer systems. These effects must be characterised and controlled by (i) determination of the stress level, (ii) methods of stress compensation, (iii) qualification of long term adhesion properties, (iv) thermal and humidity cycling tests.

Coating Characterisation: the available characterisation techniques need to be adapted with respect to the size and complexity of the coatings required.

The methods and technology required to address all these issues is known, and we are optimistic about the ability to develop, characterise, and manufacture high throughput broad and narrow band filters, as well as OH suppressing filters, for MICADO.

5 DETECTORS

5.1 Focal Plane Array and Detectors

The baseline detector for MICADO is the HAWAII-4RG, the basic properties of which are summarised in AD6. These have a number of important advantages for MICADO: (i) they are large format, so that relatively few detectors need to be characterised and mosaiced, (ii) they have been designed for the stringent requirements of space astrometry missions and so are ideal for MICADO astrometry applications, (iii) the readout speed can be adjusted (even on multiple sub-regions), greatly reducing the impact of saturation due to bright targets.

The major disadvantages are the persistence and electronic ghosts. However, tests with HAWAII-2RG in XShooter (G. Finger, priv. comm.) have shown that electronic ghosting can be very significantly reduced by reading the array out slower. While this has an obvious on the brightness limit, it is mitigated by the ability to read out multiple sub-arrays at a faster rate. During future project phases, the optimal compromise in this respect will be investigated. Post-processing to remove electronics ghosts will be considered if necessary. In terms of persistence, improvements in the manufacturing process are continually reducing the persistence effect (R. Blank, priv. comm.); and in addition the effects can be largely mitigated by keeping the array in 'reset' between exposures (G. Finger priv. comm.).

That the detectors are not directly buttable is not an issue for MICADO. The size of the gaps is relatively small (each a few millimetres compared to the 25cm width of the focal plane). Indeed, this can be considered an advantage since it provides a quasi-coronograph, allowing one to position a bright star out of the field of view even in dithered exposures. That the MICADO focal plane is curved also means that gaps between the active areas of the detectors are inevitable.

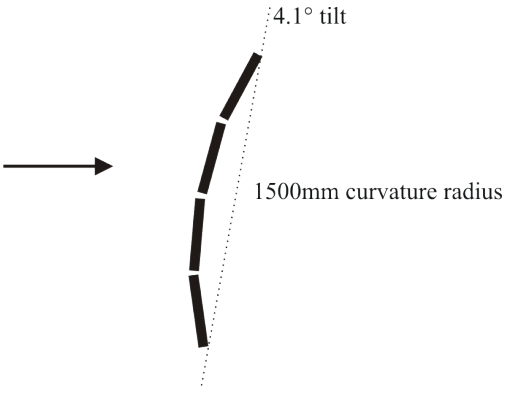

Figure 50: illustrations of how the detectors (thick black rectangles) will tile the curved and tilted MICADO focal plane (primary imaging field). The diagram is highly exaggerated, in order to show these effects clearly.

The focal plane is tilted by 4.1° and in addition curved, with a 1500mm radius of curvature (this is a direct result of the curved focal plane from MAORY). The maximum tilt of any detector with respect to its neighbours is only 4°. Due to the finite thickness of the detector units, this needs to be taken into account when designing the focal plane array. Because the

60mm wide detectors are flat while the focal plane is curved, there will be a small defocus across each detector due to the ±0.32mm relative mismatch. We have estimated the impact, and this has relatively little impact on the spot diagrams, while the Strehl ratio at 0.78µm remains above 88% across the whole field (i.e. significantly larger than the minimum Strehl used for tolerancing).

In order to optimise stability of the focal plane array, all the detectors will be mounted on a single baseplate, as shown in Figure 51. The firm G.L.Scientific has a good reputation for manufacturing baseplates for mosaic arrays (and produce that used for HAWK-I).

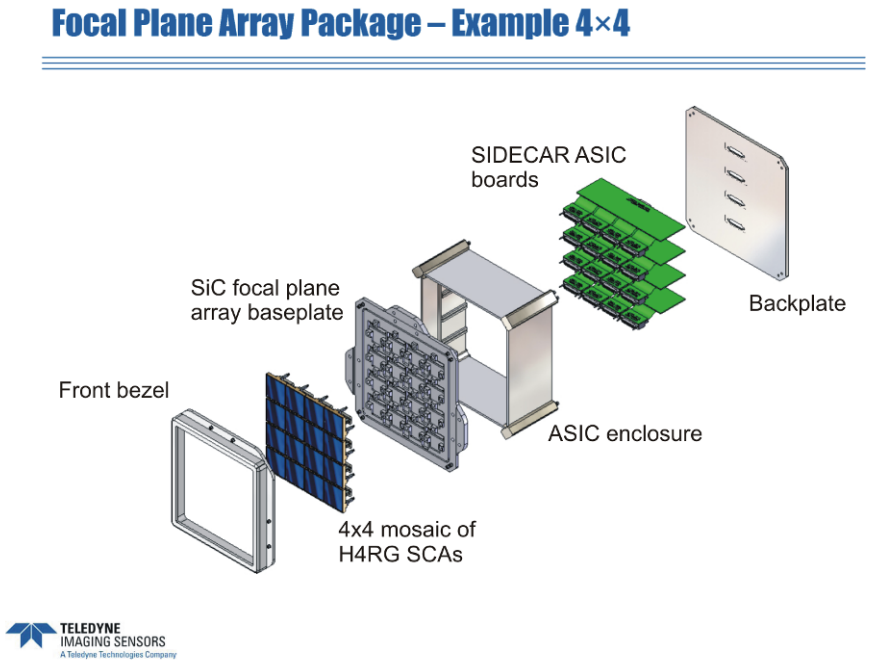

Figure 51: illustration of how an array of 4×4 detectors could be mounted onto a monolithic focal plane array in a single package. Figure provided by R. Blank of Teledyne.

6 MECHANICS

6.1 Summary of Major Design Choices

The next paragraphs describe the major design choices of the opto-mechanical and general instrument layout development related to the various mentioned subjects.

6.1.1 Impact of Space Envelope

This limited height as described in 3.2.2 was a major driving force in the folding of the cold optics optical model and general layout of MICADO as presented in more detail in 6.4.

6.1.2 Derotator

To keep the torque loads on the derotator as low as possible, it is paramount to design MICADO in such a way that the Center of Gravity (CoG) would stay close to the rotation axis, i.e. the optical entrance axis. This is a driving force in the folding of the cold optics optical model.

6.1.3 No Internal Adjustment

After only a single iteration of the Monte Carlo analysis it became clear that it would certainly be possible to assemble the cold optics without any adjustments. This means that direct milling of accurate interfaces of parts (or an assembly of parts) would be sufficient enough to achieve the static positional and angular tolerances. This will greatly simplify the mechanical design and reduce AIT time.

6.1.4 Placement of Instrument Operational Equipment

To keep the data cable length from detector to electronic rack as short as possible, and without the electronics racks presenting a load on the derotator, it was decided to place all the necessary electronics racks on top of a dedicated rotating platform mounted to the Nasmyth platform (see Figure 52).

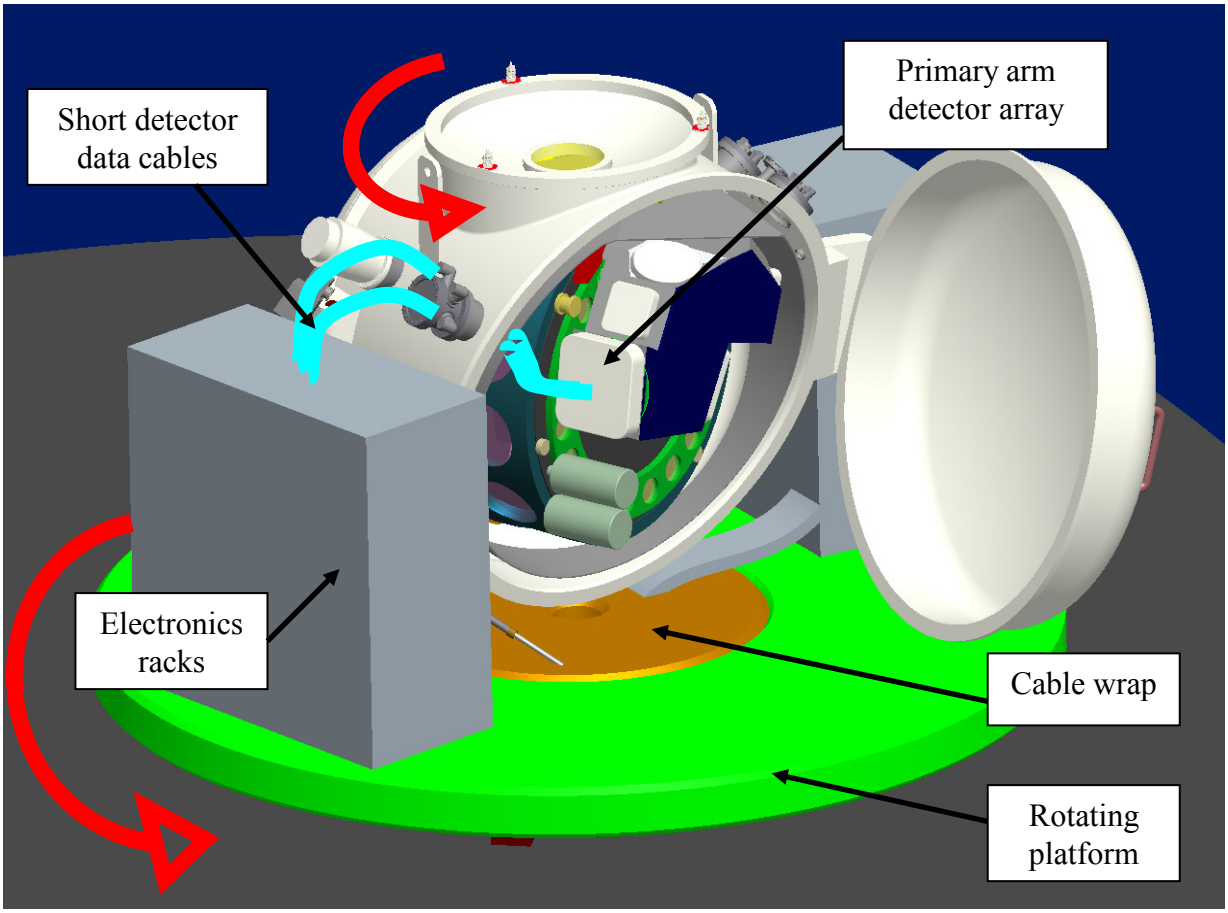

Figure 52: Low electronics racks on rotating platform, minimal detector cable length.

This platform will rotate along with the derotator but without a direct mechanical coupling.

As the derotator needs a support structure close by to support the 3ton cryostat + instrument, space for the electronic racks is limited. The electronics racks are therefore not the usual 2m high type but the shorter 1.3m variant. To prevent collisions or stress on cabling, the rotating platform co-rotates with the cryostat in a master-slave configuration.

Another advantage of the rotating platform supporting the electronics racks is the possibility of incorporating the cable wrap in the centre of this platform resulting in a short route for cabling and piping from the cable wrap to the cryostat (see Figure 53).

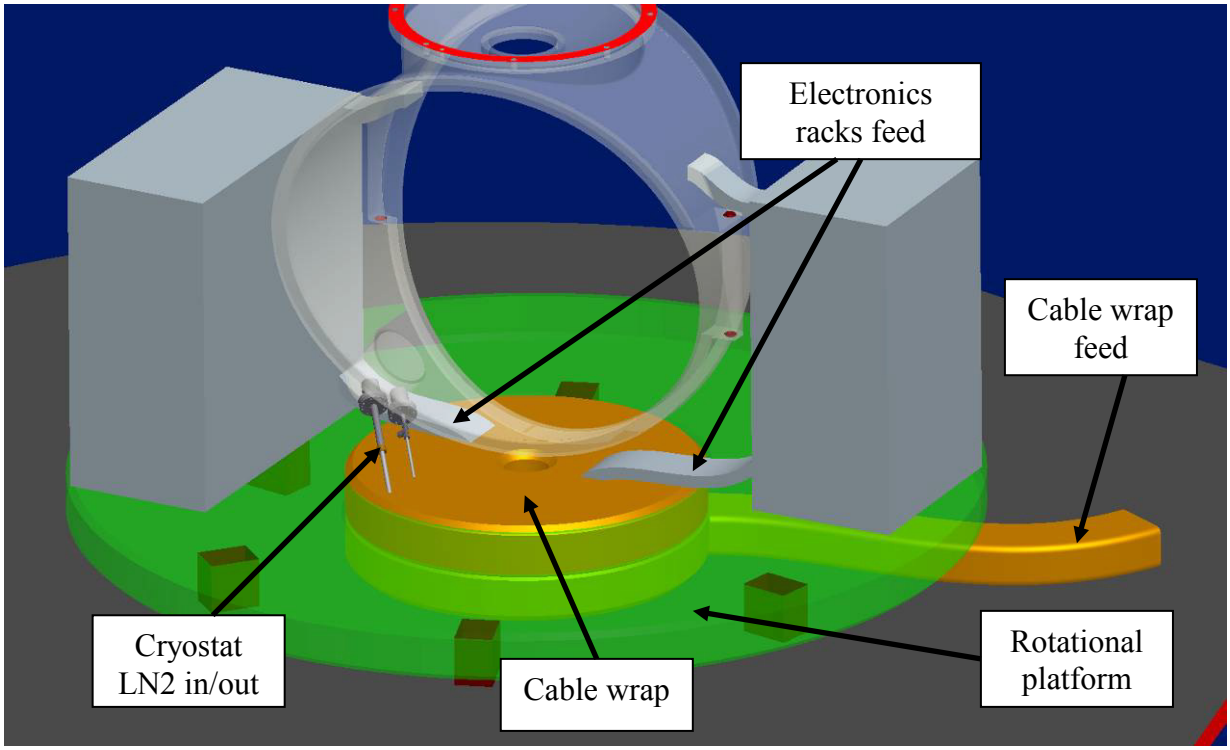

Figure 53: Cable wrap in centre of rotating platform. Platform and cryostat center wall semi-transparent, instrument not shown.

Having the cable wrap coupled to the platform reduces the load on the derotator and significantly simplifies the interfaces between MICADO and SCAO/MAORY (no cabling/piping, minimal load). Power and data cables and LN2 piping feeding the cable wrap will enter the cable wrap in between the Nasmyth platform and the rotating platform.

6.1.5 Accessibility/Servicing

Due to its location, tucked away beneath SCAO/MAORY, the removal and reattachment, plus possible realignment, of the MICADO instrument is likely to be elaborate, time consuming and risky. Therefore the focus during the cryostat design was to service the instrument on the spot with a minimum use of heavy, bulky equipment. Elements that are likely in need of service such as detectors, mechanisms and filters are designed to be located at the outside of the cold structure and well accessible using a cryostat design with two large doors (see Figure 54).

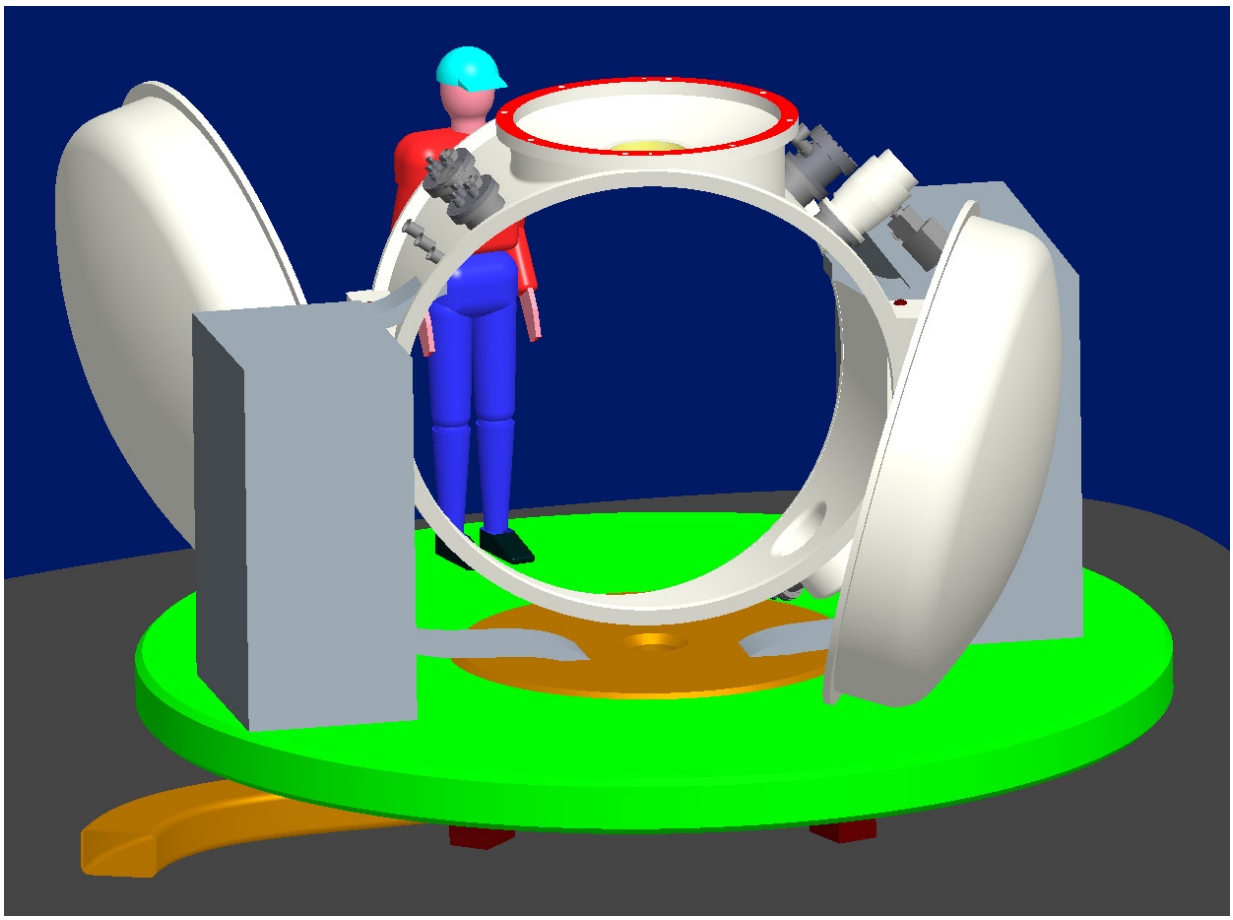

Figure 54: Cryostat with two large doors. Instrument operation equipment is shown for reference.

During the optical folding process it became clear that the obvious vertical cylinder cryostat would not match at all regarding accessibility and the demand for an on-axis CoG. Instead, a horizontal cylinder fits much better and is also easy to cap off with two large doors creating excellent accessibility. This accessibility could attribute to keeping the amount of time for AIT and commissioning to a minimum.

A bonus of the horizontal cylinder approach is the static centre part of the cryostat wall that can be intersected from many directions by, for instance, the entrance beam, cabling, piping, pumps etc. which all could stay connected or in place while servicing.

6.2 Summary of Mechanical Tolerances

The manufacturing tolerances of all structural and optical parts and assemblies are large enough to be able to assemble the MICADO cold optics without adjustments. Based on Monte Carlo analysis and current mounting interface size and positions, the strictest tolerance on any optical surface is ±0.05mm on position and ±0.01deg on orientation. Milling in assembly[1] (MIA) and

[1] Milling in assembly: assemble a number of relatively inaccurate parts and mill all accurate assembly interfaces in one setup. This approach improves overall accuracy of the assembly.

smart shared interfaces (short interface chain) will guarantee that these specifications are achievable. See the Appendix in Section 9 for the breakdown of Monte Carlo analysis data into mechanical tolerances.

6.3 Subdivision of MICADO

6.3.1 Cold Optics Instrument

The cold optics instrument is comprised of a structures, mirrors, mechanisms and detectors all partly visible in Figure 55. This assembly is connected to a cooling circuit, a harness (both not shown) and a support structure mechanically coupling it to the cryostat.

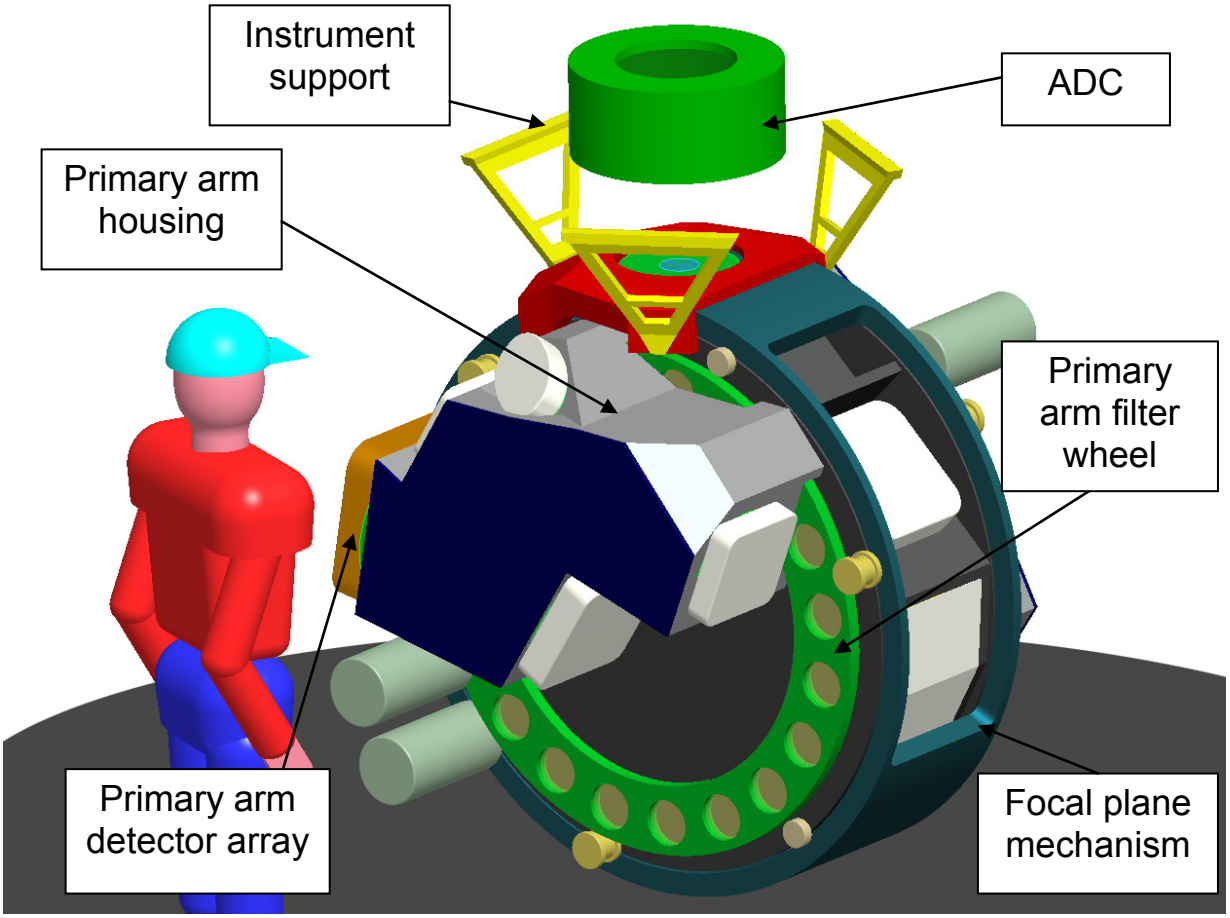

Figure 55: Cold optics, primary arm view (auxiliary arm housing not visible). The ADC is a warm unit and not part of the cold optics; it is shown here for its relative position.

6.3.2 Mechanisms

All cold optics mechanisms are rotational mechanisms with motors and gears that are positioned inside the cryostat.

Accurate (re)positioning of all mechanisms is done using the proven indent method used in MIDI (see Figure 56): a spring loaded cryogenic roller bearing snaps into a V-shaped groove repositioning the mechanism within micron range.

Driving of the mechanism is done using a cryogenic motor, a rack and pinion and a reduction gear if necessary.

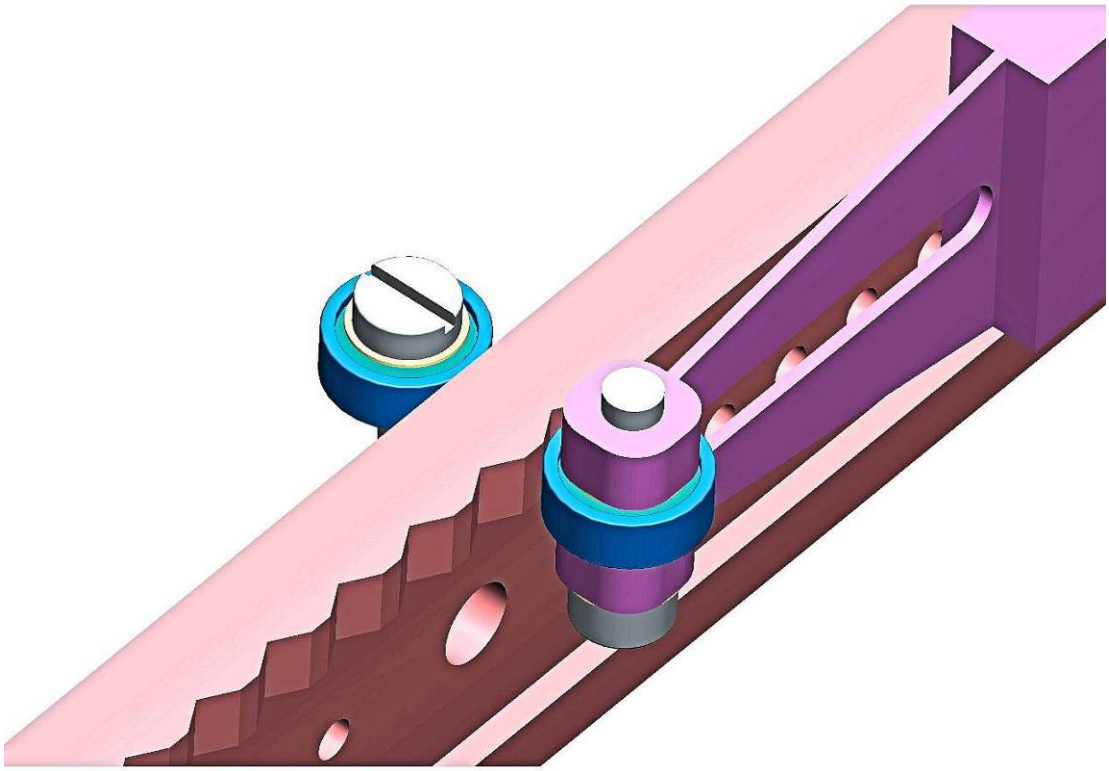

Figure 56: Accurate cold mechanism (re)positioning using a spring loaded roller bearing locking into a V-groove.

6.3.3 Cryostat

The cryostat provides the vacuum space for the instrument and hangs off SCAO or MAORY via an intermediate support structure. The top part of the cryostat supports the instrument inside. The cryostat wall, visible in Figure 57, is intersected by the window, several throughputs for cabling, LN2, etc. and also supports the vacuum pump. It has two large doors that allow ample access.

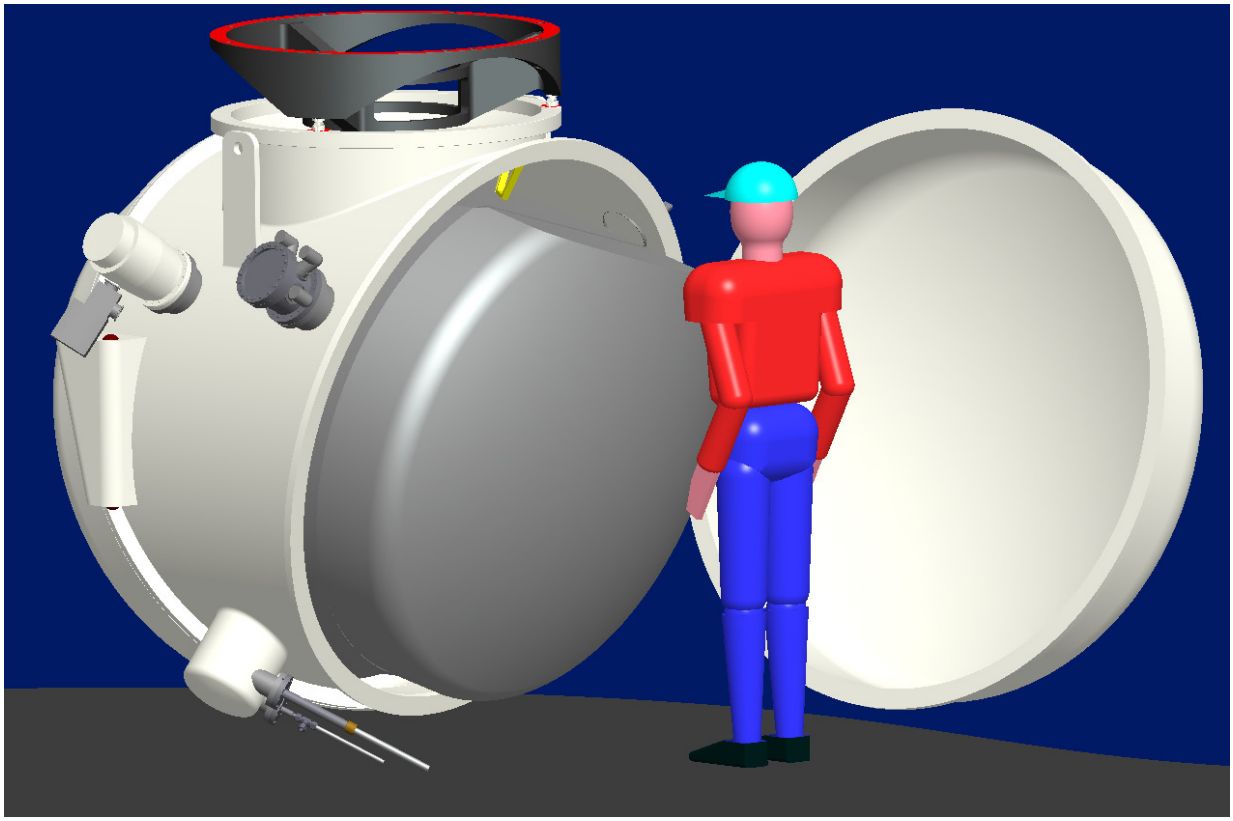

Figure 57: Cryostat with extensions and its inside MLI covered heat shield.

6.3.4 Intermediate Support Structure

Currently the MICADO cryostat is supported by a 200mm high intermediate structure shown in Figure 58. This is a result of the decision to place the ADC unit at room temperature effectively pushing the cryostat interface down.

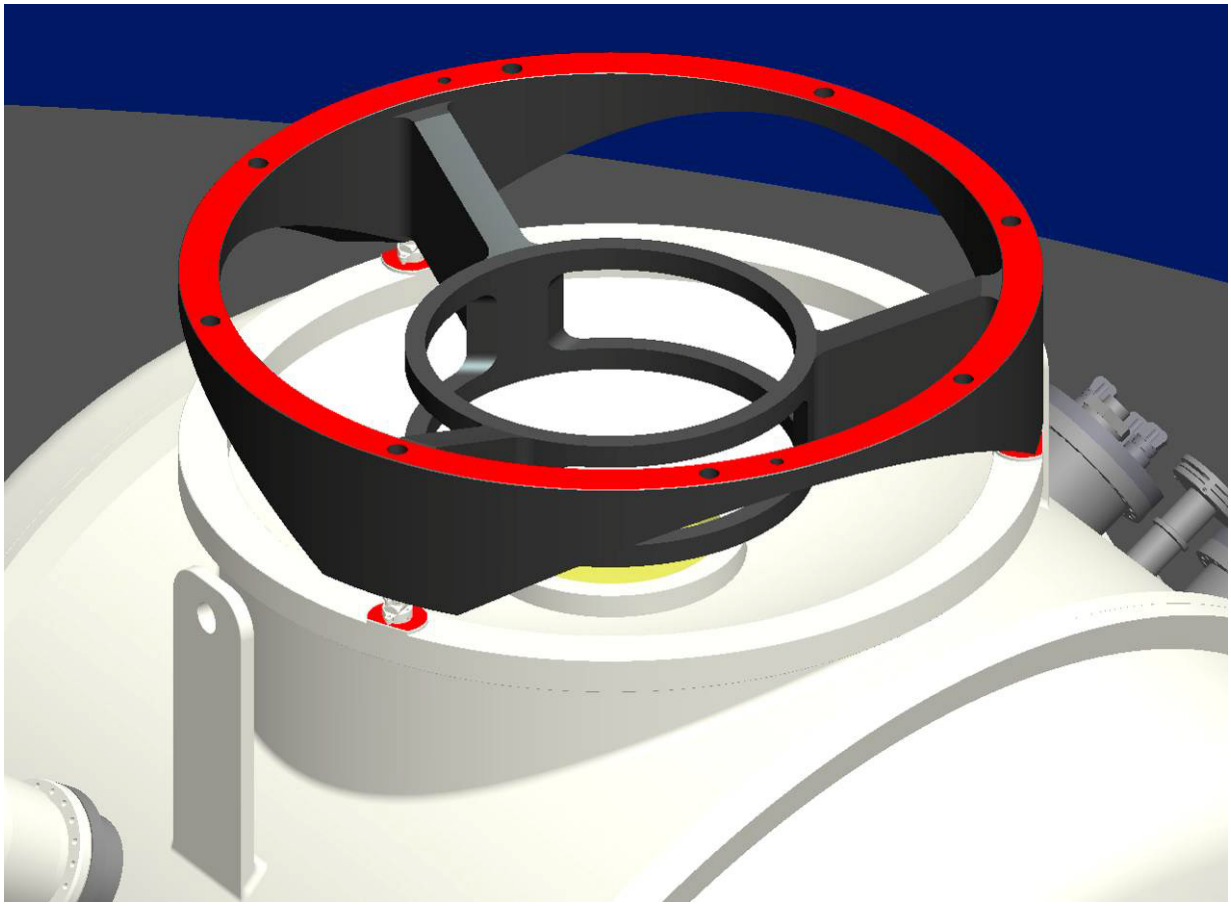

Figure 58: Intermediate support structure coupling the cryostat to the MICADO mounting interface.

6.3.5 Support Equipment

To assemble MICADO, and its operational equipment, beneath SCAO/MAORY a rolling crane will be used. It's a lifting trolley on two rails which are only temporarily put in place and bolted to the Nasmyth platform, see also Figure 10.

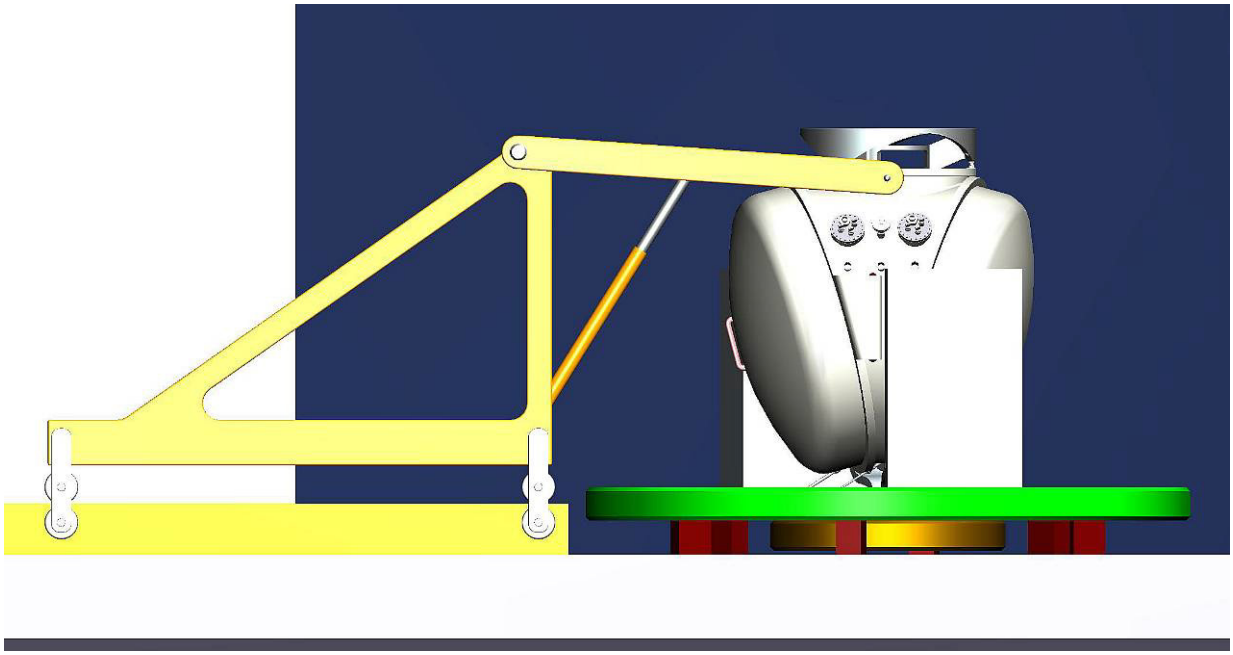

Figure 59: MICADO in the trolley lift, side view

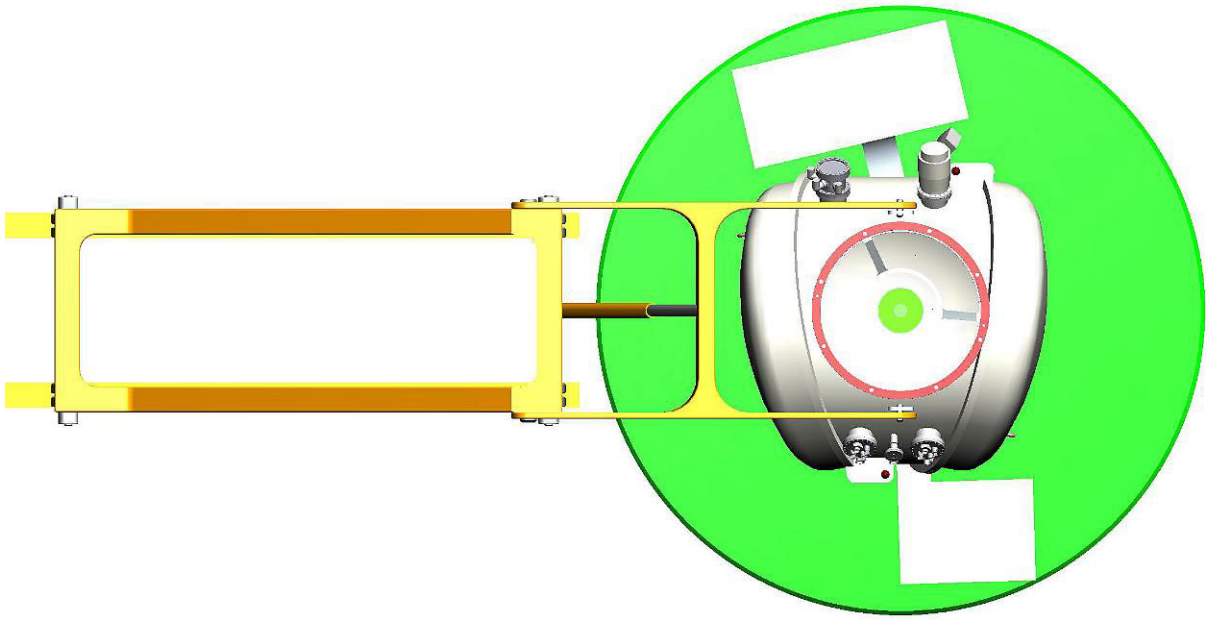

Figure 60: MICADO in the trolley lift, top view

The trolley has two movable arms that can hold and lift the cryostat (with instrument inside) akin to a pallet trolley.

A manpowered lifting device is feasible for lifting the 3 tonne cryostat + instrument. To get the MICADO on the trolley the cryostat could be lifted from the platform lift by the available crane and placed on the lifting arms of the rolling crane.

6.4 Optical Layout

The incoming beam comes down vertically (green arrow in Figure 61). The original unfolded optical models of both arms as shown are by far too big to fit in the available 2.5m space envelope.

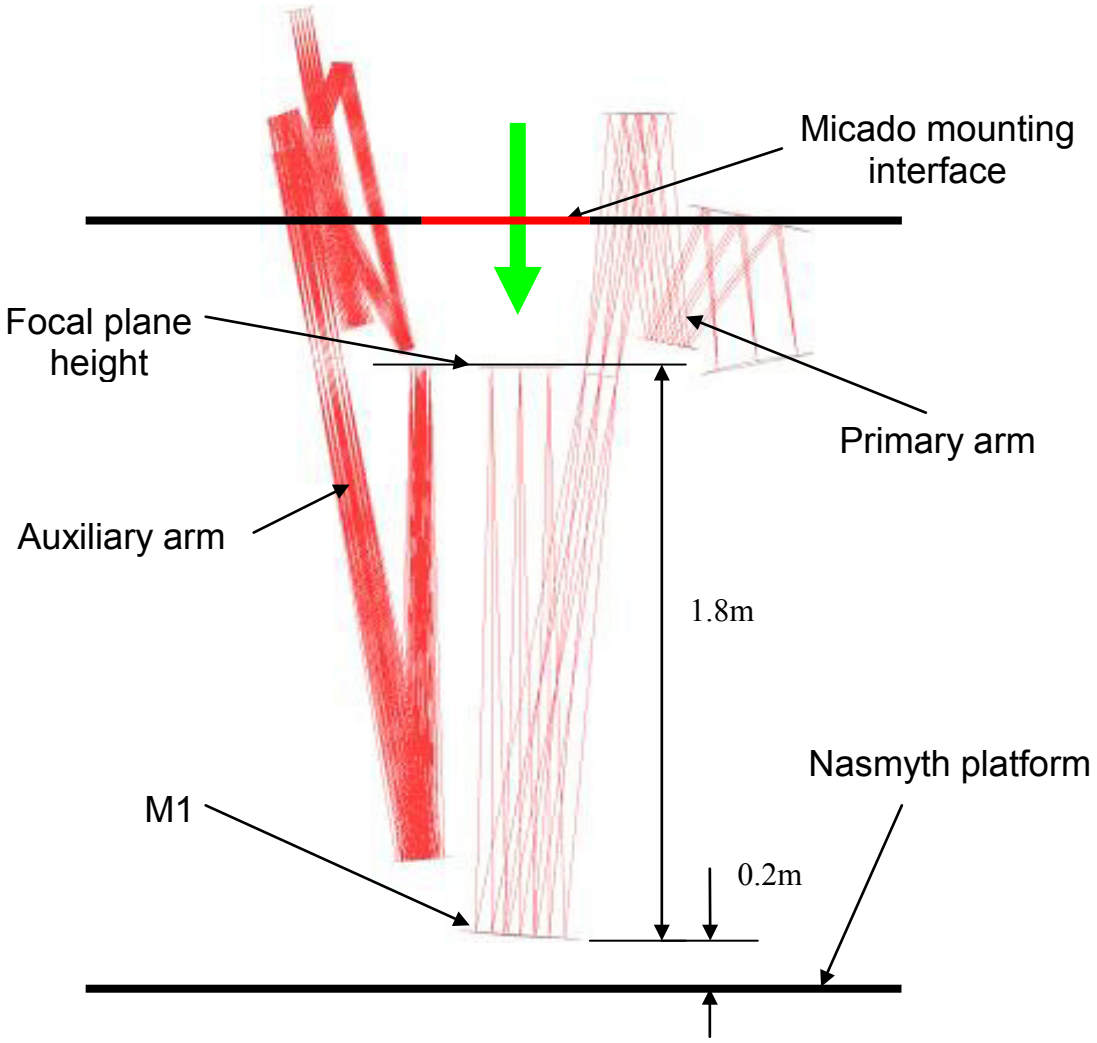

Figure 61: Unfolded optical arms projected onto the available space envelope (front view). Arms shown side by side for clarity reasons (They will share the same focal plane position).

The lowest mirror of the primary arm (M1) is too close to the Nasmyth platform and will intersect the cable wrap keeping in mind the extra space necessary for the cryostat + heat shield. On the top side both arms intersect with the SCAO/MAORY space envelope. A more complex folding of the optical model was necessary.

When folding the combined optical model of both arms into one compact opto-mechanical design, several key aspects were taken into account:

Envelope

- Overall height should be well within 2.5m.
- A compact on axis cryostat for a small rotational diameter (minimize interference with SCAO/MAORY support structure).

Use

- Good overall accessibility for servicing on final location, without loosing alignment.
- Good accessibility to mechanisms (locate mechanisms on outer perimeter of instrument).

Optical

- Insert as few folding mirrors as possible (optical performance, tolerance chain length).

Mechanical

- Transfer of loads: in- and external mounting point layout.
- Locate detectors close to the cryostat wall to keep detector cabling as short as possible.
- Try to compartmentalize both arms to reduce complexity in interfaces and design and to serve AIT.
- Minimize the number of interfaces, or share them, to be able to achieve the strict positional and angular specifications of the optical model (see Appendix).
- Find common mechanical approach strategy for simple design/MAIT and low cost/time.

Mechanism Space

- The focal plane is large (diam. 250mm) and has 6 positions; therefore the focal plane selection mechanism will consume a large area/space inside the cryostat.
- Accommodation of two large filter wheels of ~1.1m diameter (each 20 positions, filter diameter ~100mm).
- Sufficient space for the primary/auxiliary arm selection mechanism.
- Sufficient space for the auxiliary arm scale change mechanisms.

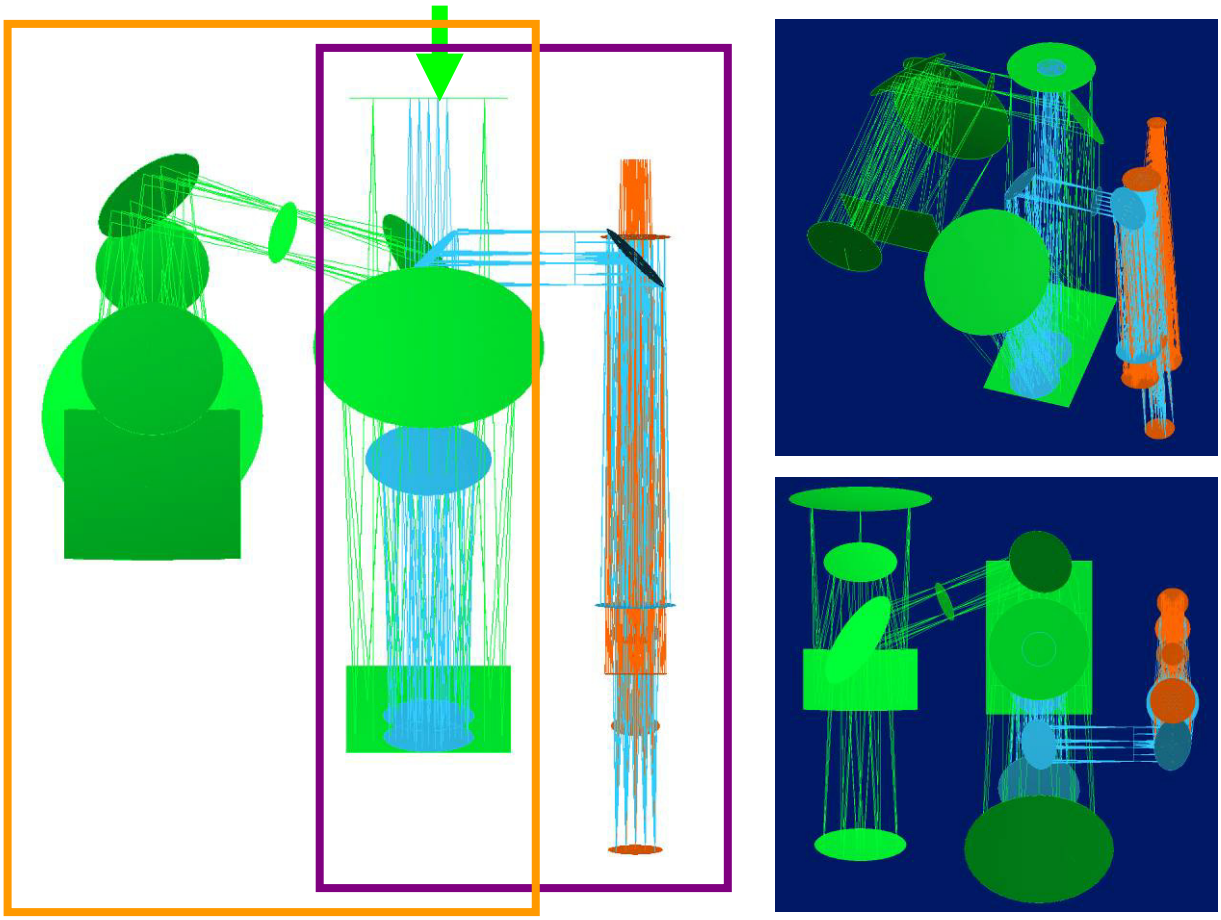

Figure 62: Folded optical model, both arms combined, primary arm in green, auxiliary arm in violet/orange. Left: front view, right top: 3D view, right bottom: top view.

After several iterations the chosen folding concept, shown in Figure 62, suits all requirements best. The MICADO optical layout can roughly be split up in three sections: a common core section and two separate side sections. The logical separation between the core and side sections is near both arm pupils where the filter wheels will be located. This separation allows separate AIT of each section, reducing overall project time as the various disciplines (design, production, AIT) can work in parallel. Another advantage of this left-right separation between the two arms is the independency, allowing a partly separate development of both arms with limited cross impact.

6.5 Cold Optics Instrument Layout

The cold optics instrument is thus roughly split up in three parts, a logical approach looking at Figure 62:

1. The core sub-assembly
2. The primary arm sub-assembly
3. The auxiliary arm sub-assembly

The two filter wheels will sit in between.

The general design approach of these main structures (the core and both arm housings) is to assemble them from plate material (in the range of 2 to 20mm) to keep part complexity and accuracy low and as much as possible '2D' thus allowing easy outsourcing. The many smaller walls panels supporting the optics are sandwiched between two side panels. This ensures a simple but rigid boxed structure. All accurate mounting surfaces will then be milled during the last stages of production using milling in assembly.

6.5.1 Core Sub-Assembly

The dark gray core structure visible in Figure 63 supports the primary/auxiliary arm selection mechanism, the largest mirrors belonging to both arms up until the intermediate pupils, and is surrounded by the focal plane selection mechanism which it also supports. Both arm housings are mounted to the core on its flat sides, partly through the hollow filter wheels. The core sub-assembly is coupled to the cryostat via a transfer structure basically transferring a stiff 4-point support on the instrument side into a 3 point support for a kinematic correct connection to the cryostat.

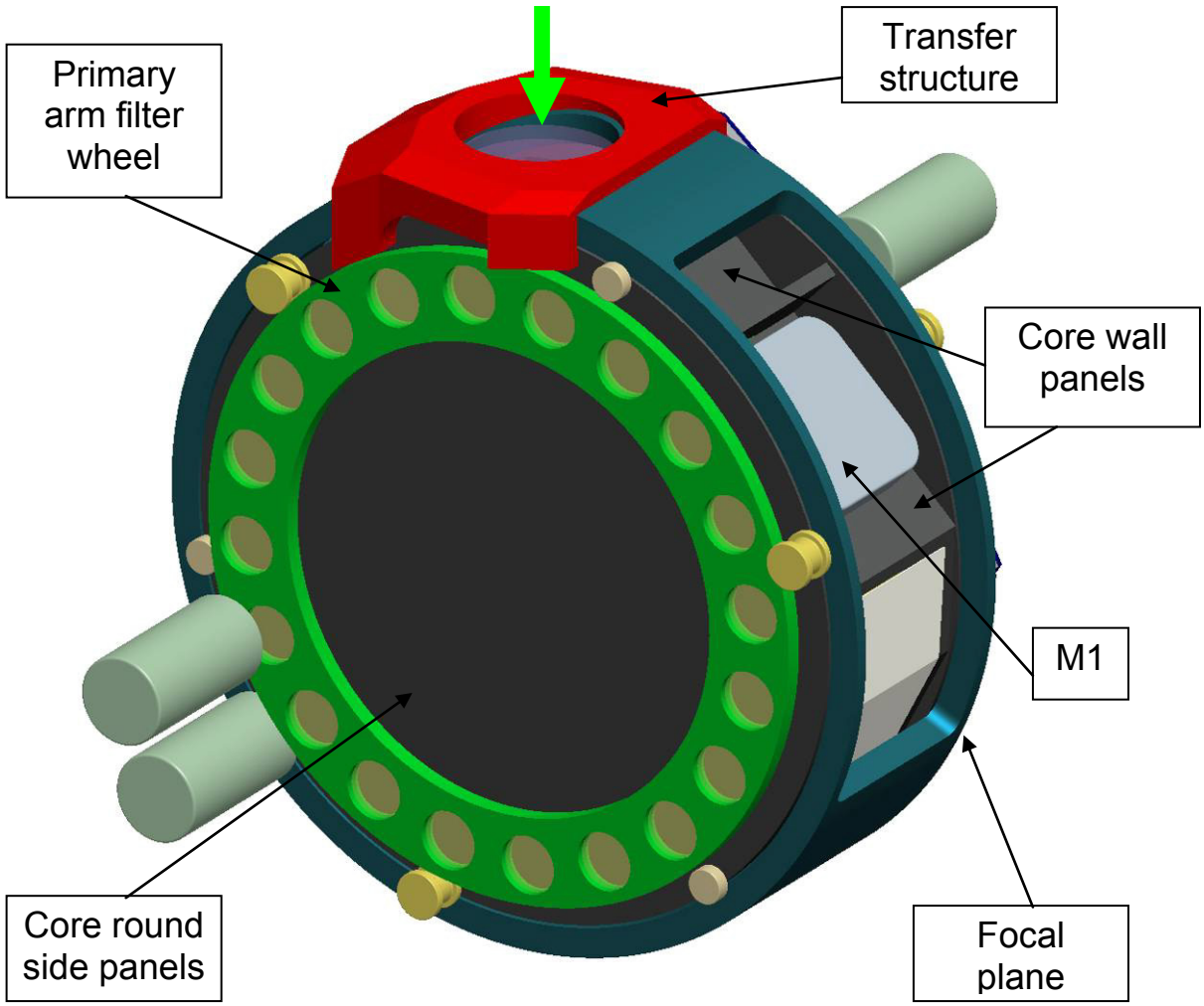

Figure 63: Core sub-assembly. The internal primary/auxiliary arm selection mechanism is not visible.

The filter wheels for both arms are mounted on the core's round side panels. These wheels will be hollow to allow direct mounting of the arm housings to the core to create an overall stiff and accurate mechanical structure. The three point mounting interface layout between the core and both arm housings is defined in such a way that both arm housings are connected to the round side panels with direct support underneath from core wall panels. The relatively thin round side panels therefore won't bend due to the external loads minimizing global deformation.

The wheels will be supported on their perimeter. They will be covered by a simple plate cover to protect and shield them from residual heat radiation coming off the heat shield (plate cover not shown).

6.5.2 Primary Arm Sub-Assembly

The primary arm housing supports the second half of the primary arm optics and its detector array visible in Figure 64 below.

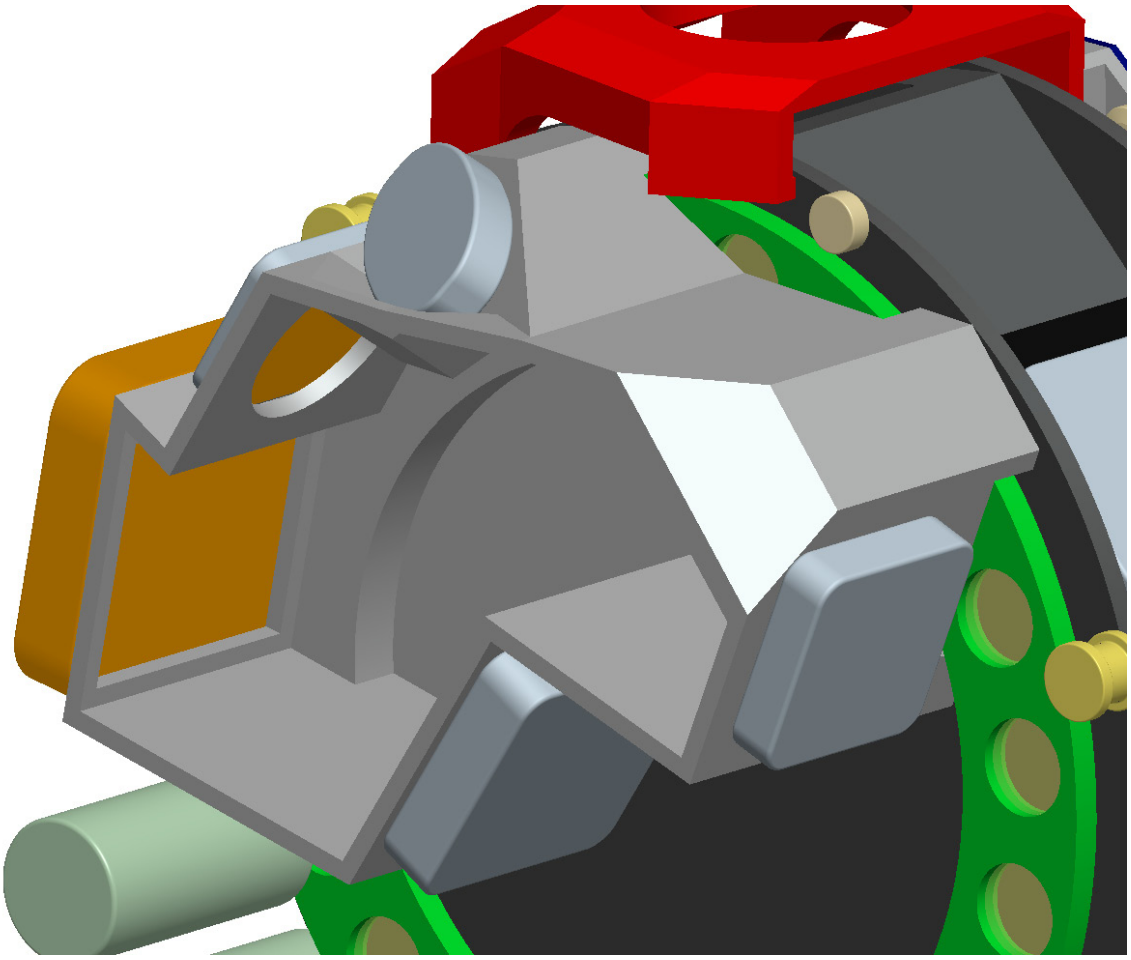

Figure 64: Primary arm housing attached to the core structure (housing cover removed).

It is assembled of plate material and closed by a simple plate cover (not shown). The detector array will be mounted semi-insulated to be able to control the detector array temperature separately from the primary arm housing.

6.5.3 Auxiliary Arm Sub-Assembly

The auxiliary arm housing supports the second half of the auxiliary arm optics, the scale change mechanisms and one detector all visible in Figure 65.

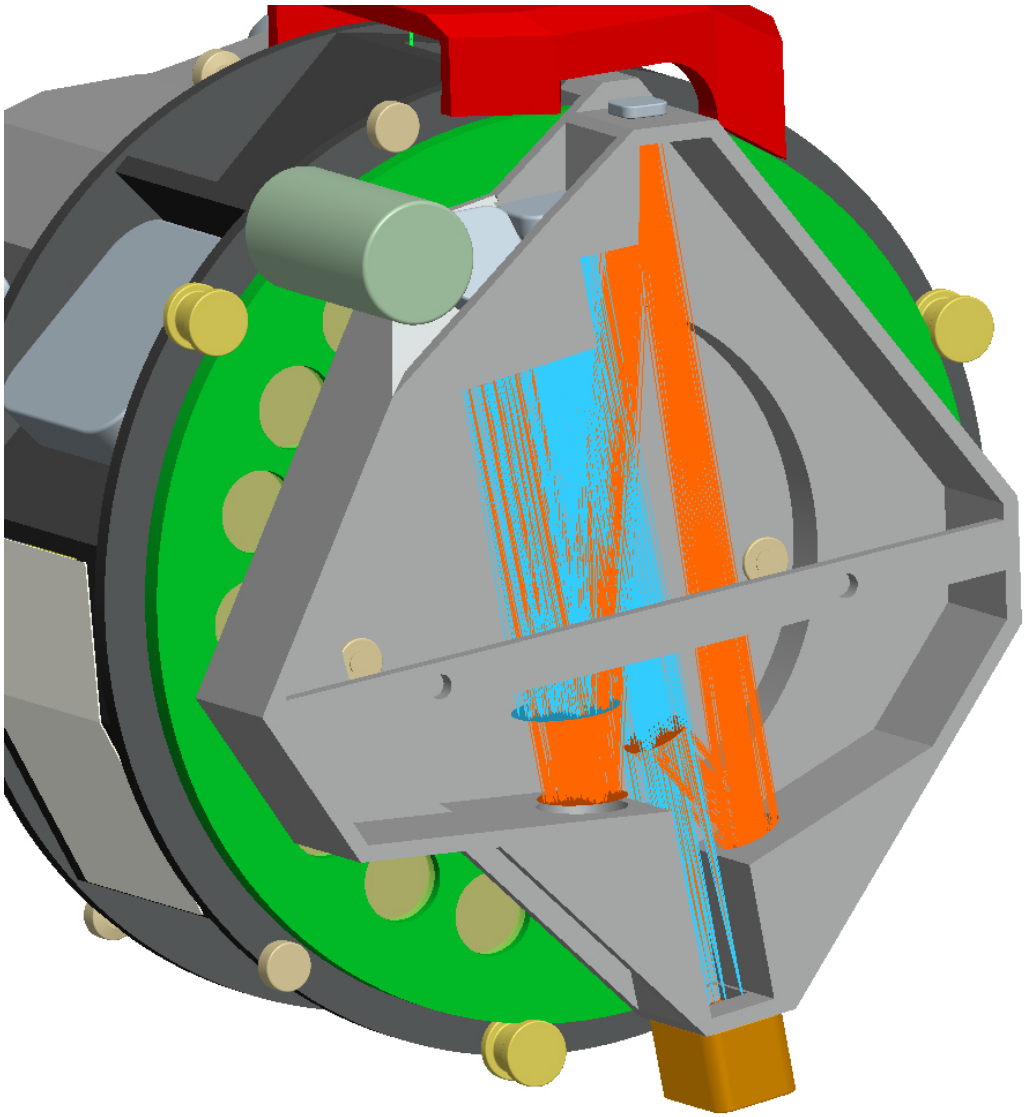

Figure 65: Auxiliary arm housing attached to the core structure (housing cover removed). The optical paths of both scaling options are visible (blue & orange). Scaling selection mechanisms not shown.

It is assembled of plate material and closed by a simple plate cover (not shown). The detector will be mounted semi-insulated to be able to control the detector temperature separately from the auxiliary arm housing.

6.5.4 Instrument Support Assembly

The instrument core is supported by the cryostat using three V-rods and a transfer structure, both visible in Figure 66. The V-rods are coaxially positioned around the incoming beam ensuring that when operational (i.e. shrunk) the instrument stays aligned properly.

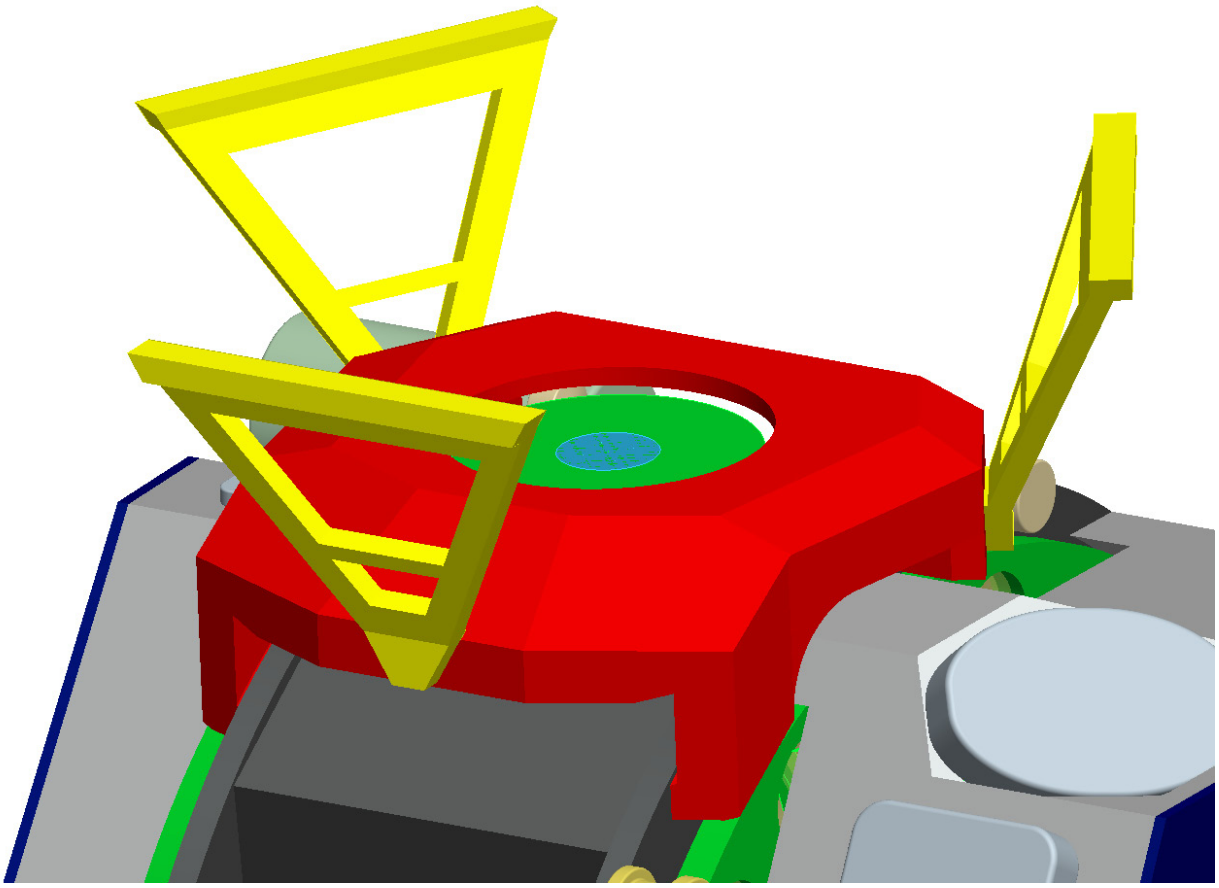

Figure 66: Instrument support assembly: three V-rods (yellow) and a transfer structure (red). The focal plane selection mechanism is not shown.

The V-rods will have elastic hinges on both ends (not shown) allowing the necessary deformation of the V-rods. Material used will be either stainless steel or titanium based on thermal and mechanical demands. This concept has successfully been used in X-Shooter in which is even stiff enough to allow tilting + rotation of the whole instrument. For MICADO this setup will be stiff enough around the optical axis to minimize any rotational wobble of the image on the detectors.

The transfer structure exists because of the choice of rotating the focal plane selection mechanism around the core (see also 6.6.1). This excluded an easy 3 point mounting on the core structure and, as the core has parallel side walls that are very well suited to carry vertical loads, a 3-to-4 point transfer structure was designed.

6.5.5 Known Issues

There are still two minor intersection issues between optics/beams/housing, in both cases around the folding flat following the intermediate pupil of both arms (see Figure 67).

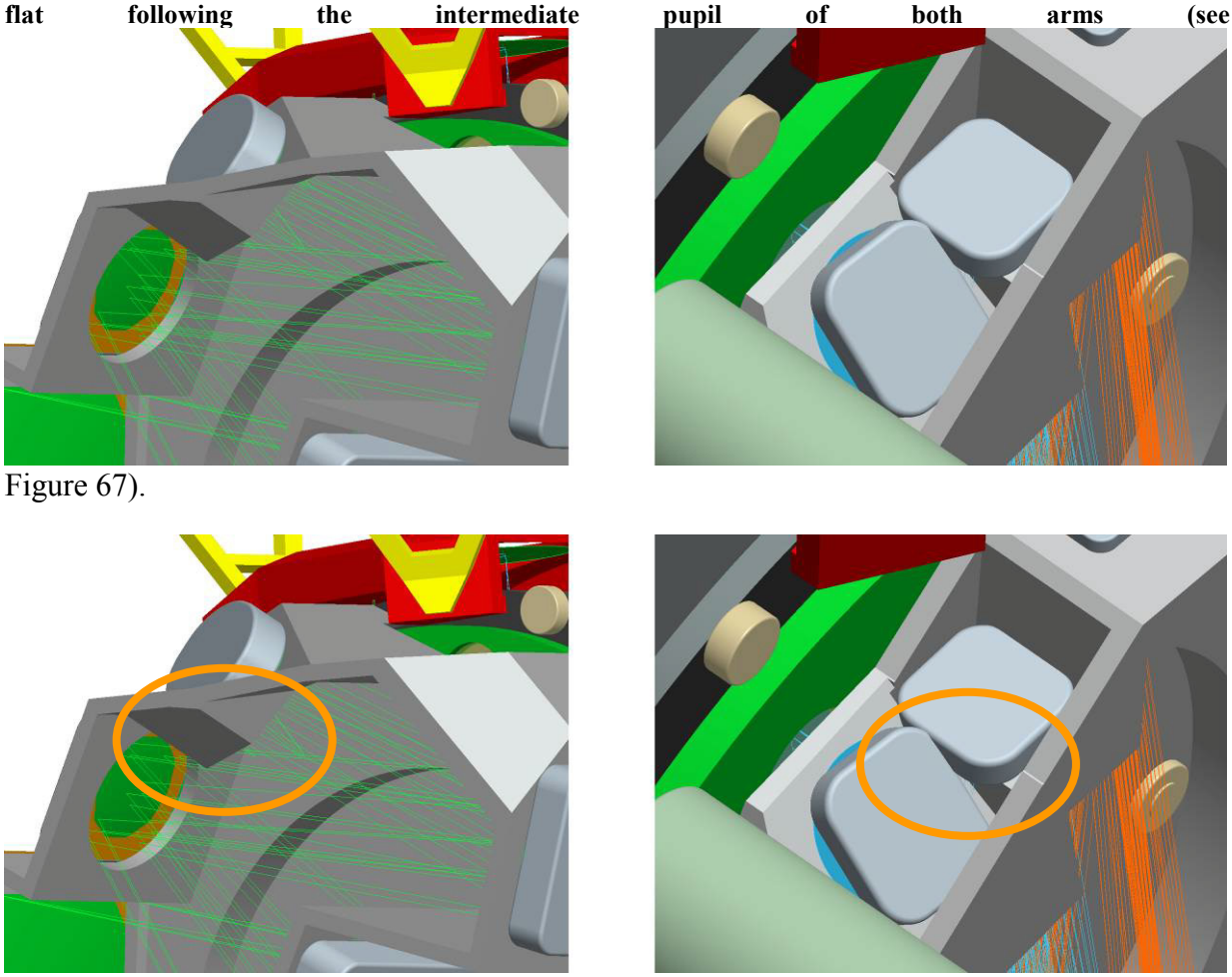

Figure 67: Intersection issues around the folding flat following the intermediate mirror. Left: primary arm, right: auxiliary arm.

These can be solved by altering the angle of the mirror following each folding flat. A quick optical check has revealed that the necessary ~3° extra tilt is found to have a negligible impact on performance and only limited impact on position and surface shape of the following optics. There is sufficient space margin around the arm housings to deal with this alteration without any impact on the cryostat dimensions.

6.6 Mechanisms

6.6.1 Focal Plane Selection

The focal plane selection mechanism has 6 positions containing the various plane masks. Due to the horizontal cylindrical layout of the optical model plus the filter wheels, and thus cryostat, adding a selection wheel for the focal plane was only possible if the wheel would rotate around the core structure only slightly increasing the cryostat centre wall diameter (see Figure 63). As this wheel would block the access to the core mirrors and primary/auxiliary arm selection mechanism a large slot opening was added to the focal plane wheel.

The wheel is supported on the rim by three sets of bearings. One set is spring-loaded to allow shrinkage and maintain contact. The wheel is driven by a motor drive on the rim.

6.6.2 Primary/Auxiliary Arm Selection

The core has only one internal mechanism which selects the optical arm in use (see Figure 68).

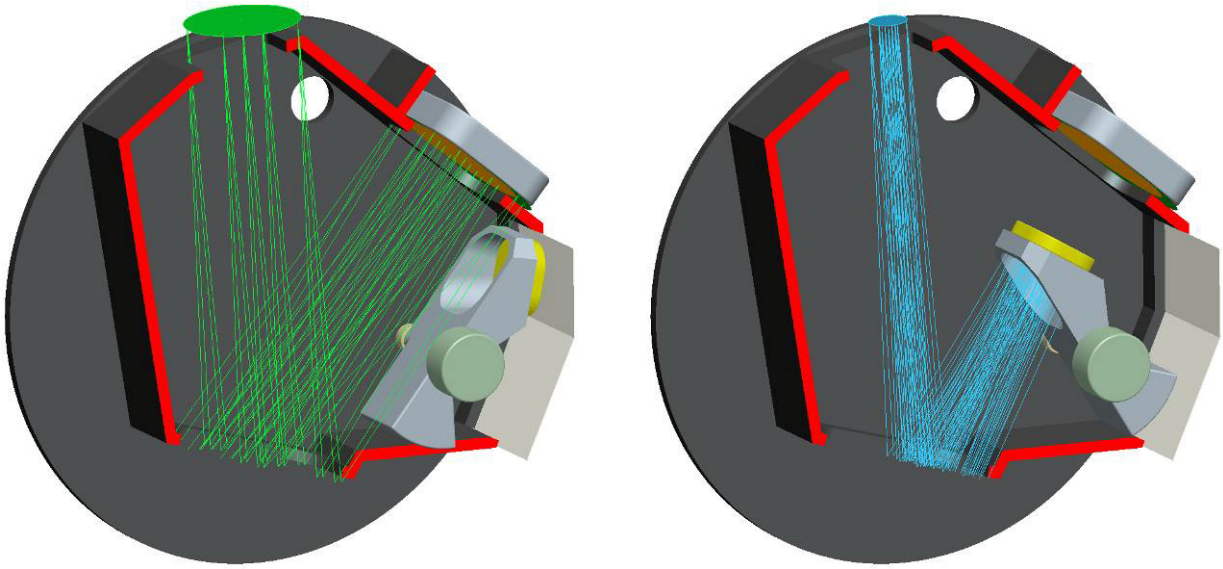

Figure 68: Primary/auxiliary arm selection mechanism inside the core structure. Two positions are shown. Left: primary arm active, right: auxiliary arm active.

This rotating mechanism is recognised as being the most delicate one inside the cryostat; it switches a curved mirror (parabola, 165x165mm), is located inside the core of the instrument (normally limited access) and is functionally critical as it switches between two halves of the complete instrument.

As the core wall layout is partly dictated by the mounting points for the optimum support of both arm housings, the available space for this mechanism was limited. Several mechanism configurations were considered (other rotation point locations, using a sliding mechanism

instead, etc.) but, taking into account the other mirror moving mechanisms, a common rotational approach for all these mechanisms turned out to be the best overall solution.

As mentioned in 6.6.1, the focal plane selection mechanism already has a large slot opening to increase accessibility to the primary/auxiliary arm selection mechanism. The two wall panels directly behind this mechanism have a large access opening allowing the complete removal of this mechanism. This opening will be covered by simple plate material. Accessibility of this mechanism turns out to be quiet good; opening one cryostat door, removing the heat shield side panel behind it, and removing the wall cover are the only three steps to gain access.

In the design of the mirror support special care will be taken to ensure that any g-forces acting on the mechanism while clicking in position will not lead to any permanent dislocation of the mirror. See for mechanism positional locking 6.3.2.

6.6.3 Filter/Grism Wheels

The filters wheels are mounted to the sides of the core structure (see Figure 63).

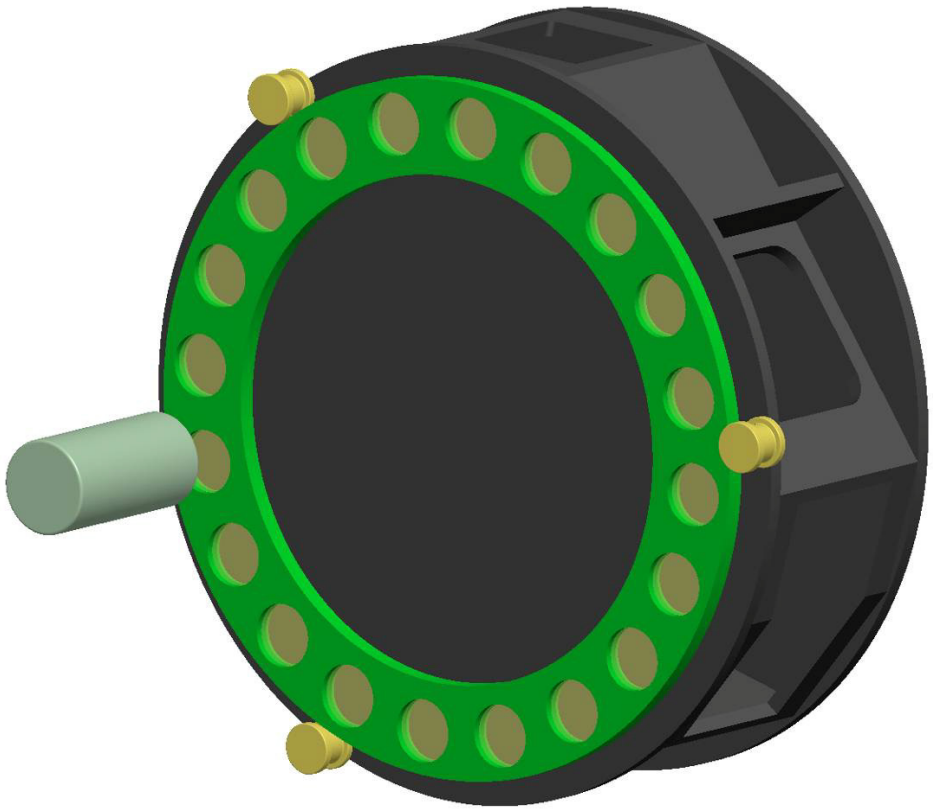

Figure 69: Image filter wheel mechanism with bearings and motor

As each wheel contains 20 filters, this high glass volume will dictate the minimum cool down time. On a small mechanism a braid could be added to bypass the bearings to improve thermal contact but as these two wheels are large and hollow, the braid would become impractically long negating any thermal contact improvement.

What might be considered to improve thermal contact is radiative cooling. For this a large surface area is necessary that could be created by adding axial standing ribs on the wheels that would run in grooves in the core side panels, TBC by thermal modelling.

Another solution would be to use a thermal switch; one might think of a standing rib made from a different material mounted on the core side panel that would, due to CTE differences, shrink onto the circumference of the wheel (at above operational temperatures), thus creating a large contact surface facilitating excellent cooling. This is a simple, effective and reliable solution. The only worry would be not to stress the wheel support. Adding some elastic movement ability in the standing rib could keep shrinkage forces to an acceptable minimum.

6.6.4 Scale Change Mechanisms

The auxiliary arm has two mechanisms to insert/remove mirrors for the scaling of the image, both visible in Figure 70.

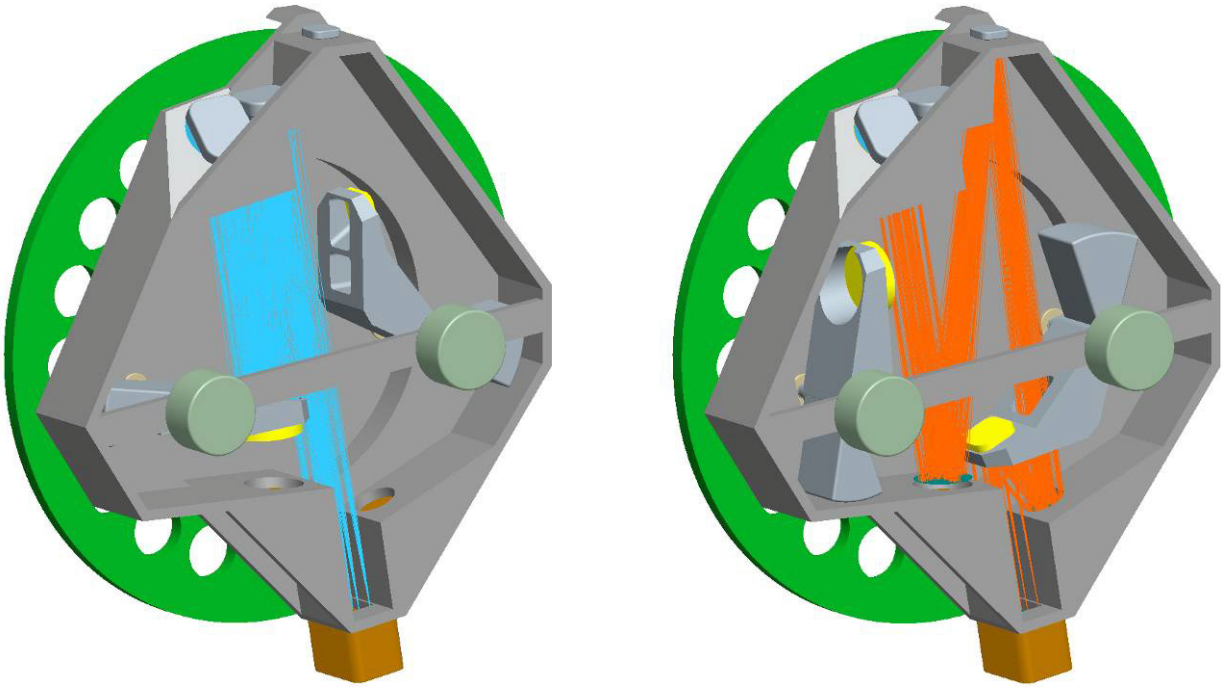

Figure 70: Auxiliary arm scale mechanisms. Left: scale change position A, right: scale change position B.

The mechanism design is very similar to the primary/auxiliary arm selection mechanism.

The goal for Phase B is to change this part of the optical design in such a way that both scaling positions can be selected using only one mechanism and, at the same time, locate the detector on a similar level and instrument side as the detector array of the primary arm. Reducing the mechanism count reduces risks and improves reliability. Moving the detector will shorten the cable length toward the cryostat feed-through and will enlarge the detectors surrounding space improving accessibility.

6.7 Cryostat

6.7.1 Vessel/Heat Shield

The vessel is made up of three parts: a short large diameter centre ring closed off by two large doors (see Figure 54). To improve accessibility, the doors are hinged so no crane is necessary for opening and closing. The hinge has enough play to not dictate the doors final location when closed. Conical pins (or something similar) on the flange will define the doors final location.

The flange between a door and the centre ring is circular for easy manufacturing of the doors. As the doors are slanted to improve accessibility, the cross section of the centre cryostat wall is a slight ellipse. The centre will be made of rolled plate material and welded so the slight elliptical shape is unlikely to present a major manufacturing issue.

On top of the centre ring there is a circular extension that houses the internal support structure and is closed off by a concave cover that supports the window and the internal instrument support.

As visible in Figure 71, the orientation of the instrument is rotated by about 25 degrees in relation to the cryostat, which might seem unusual.

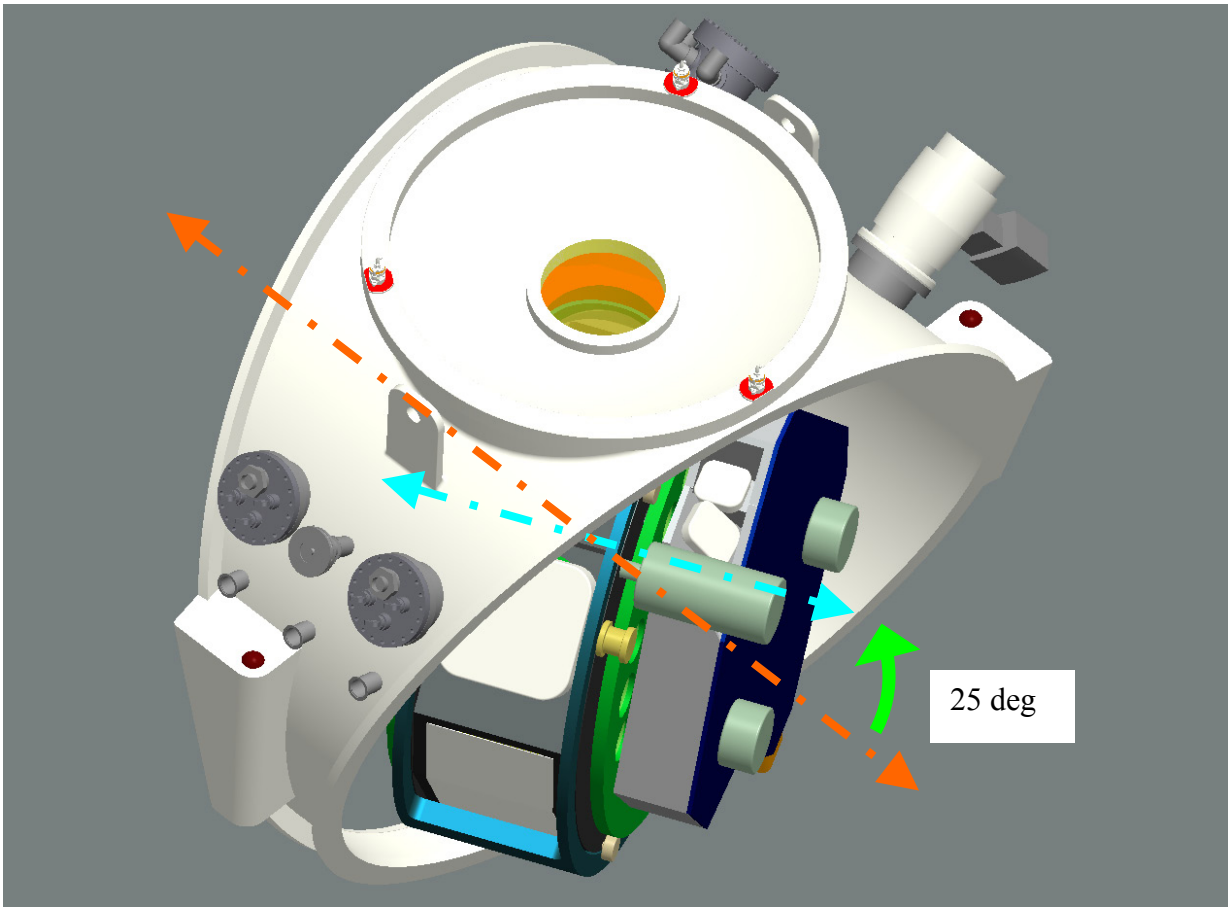

Figure 71: Offset angle between instrument and cryostat orientations. The main axis of rotation is shown for the cryostat wall (orange) and the core sub assembly (blue).

This has been purposely done to increase accessibility to:

- The primary arm detector array, while keeping the length of the cable to the feed-through to a minimum
- The primary/auxiliary arm selection mechanism, as this is tucked away inside the core sub assembly
- The focal plane selection mechanism
- The filter wheels
- The core optics

6.7.2 Cooling

Pre- and steady state cooling will be done by a constant flow liquid nitrogen system (for further detail see chapter 8 Cryogenics).

Internal cooling gear has not been added to the model due to time constraints. However, in the design of the instrument and cryostat clearance has been built-in to ensure sufficient space is available for LN2 tubing and cooling pads. Cold optics to heat shield clearance and heat shield to cryostat clearance is about 50mm, sufficient to deal with pad height, swagelock couplings and tubing.

The mounting area for cooling pads will be milled to a stricter than usual flatness/roughness specification for a lower thermal resistance. Final cooling pad locations will depend on the necessary amount of pads, the maximum allowed gradients inside the instrument and the preferred routing of tubing.

6.8 Intermediate Support Structure

The intermediate support structure (see Figure 58), coupling the cryostat to the SCAO/MAORY derotator, is just a simple ring type structure, its existence explained in 6.3.4. It allows a somewhat limited but crucial access to the ADC, to be able to adjust it, even when the cryostat is mounted.

Furthermore, the intermediate structure can easily cope with possible future changes in derotator or cryostat interfaces without the need to alter either cryostat or derotator design. This is especially critical if future design updates mean that, for whatever reason, the derotator interface of MAORY eventually turns out to be different than that of the SCAO module.

6.9 Operational Equipment

The operational equipment is just the set of electronics cabinets, cable wrap and rotating platform as shown in Figure 52. These parts all need further detailing during Phase B.

6.10 Support Equipment

6.10.1 Rolling Trolley

Several different lifting-and-removal methods have been reviewed: e.g. a stationary crane, a crane hanging on rails attached to SCAO or MAORY, moving the entire derotator etc. After examining all advantages and disadvantages only one option remained: the rolling trolley on temporary rails on the Nasmyth platform.

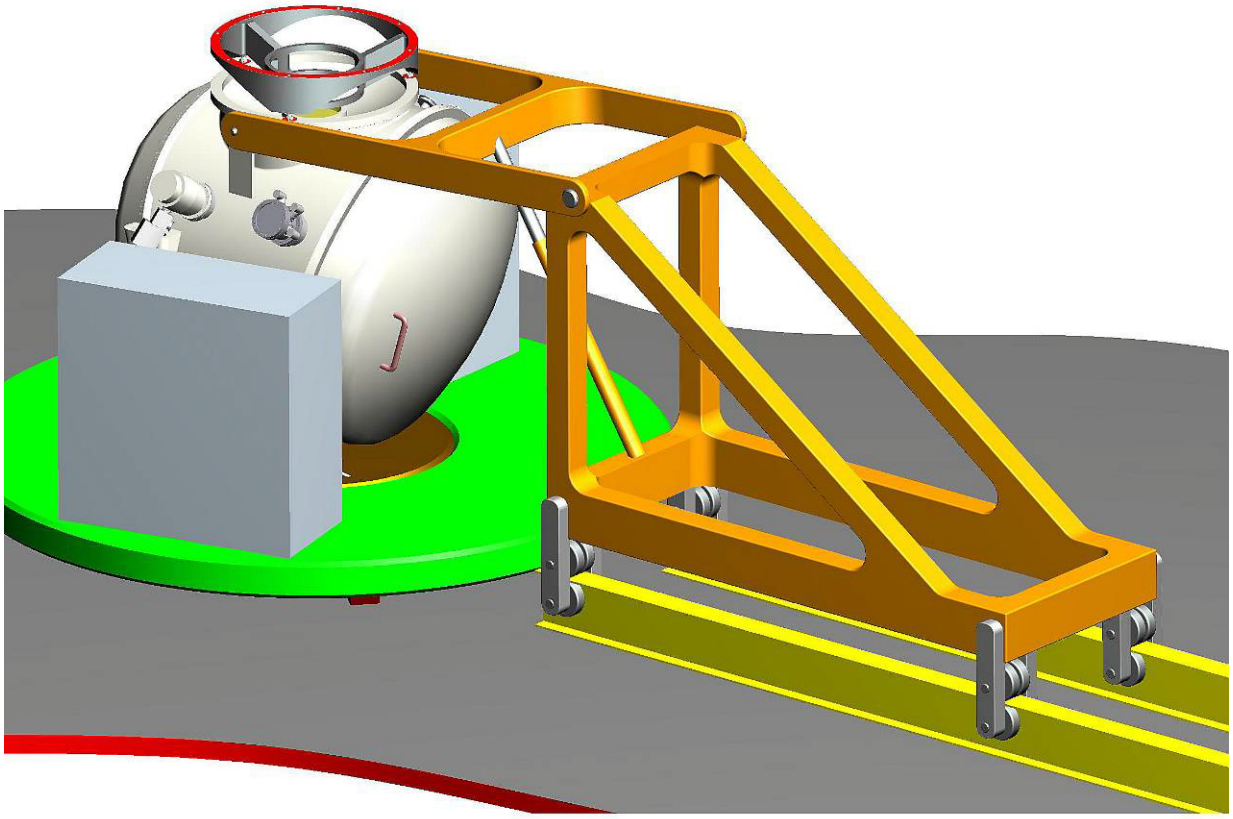

Figure 72: Rolling trolley with lifting device

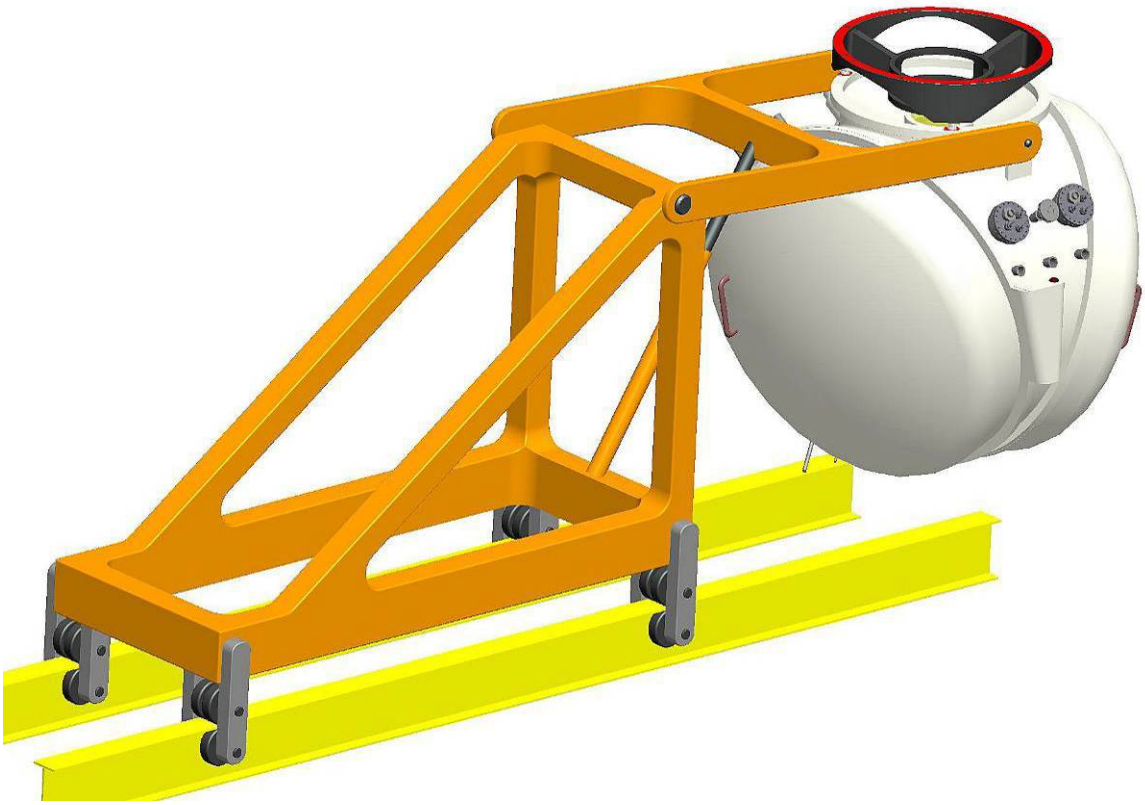

Figure 73: the MICADO cryostat supported by the trolley

Advantages of a rolling trolley are:

- No interface with SCAO/MAORY, reducing overall complexity
- Low mass but sturdy
- Simple and safe
- Incorporating a lifting device is easy
- One of the smallest space envelopes/low impact on SCAO/MAORY support structure

Disadvantages:

- Likely needs to be removed and stored after use
- Temporarily uses up a large area of the Nasmyth platform (the exact space required and its availability need to be ascertained during Phase B)

7 MECHANICAL DESIGN PRINCIPLES

7.1 Reliability

Proven designs from experience with other cryogenic instruments are used where possible. This saves time and effort, and improves reliability. For MICADO these proven design principles are adopted from: MIDI, VISIR, SPIFFI, JWST-MIRI, X-Shooter and MATISSE.

7.2 Monolithic Design

It is well known that mounting techniques like welding or brazing introduce stresses in materials. A bolted connection in itself introduces stresses, can result in slip-stick effects and poor thermal connections. However, a minimum amount of bolting is inevitable so care will be taken with regard to location, local material distribution and necessary torque values. To prevent those sources of mechanical instability and improve the thermal behaviour, parts and structures are manufactured from one monolithic piece of material wherever possible.

7.3 Homogeneity and Shrinkage

All materials shrink during cool-down. Due to the use of different materials, shrinkage differences will occur. In order to avoid CTE effects as much as possible all structures, mechanisms and curved cryogenic mirrors will be made out of the same material as much as possible. In the case of purely reflective optics this provides the important advantage of temperature invariance: the change in curvature radius of these curved mirrors due to thermal shrinkage is exactly compensated by the reduction of focal distance in the structure and the overall image quality is therefore temperature-independent (scaling).

Although temperature-invariance can be achieved for almost the complete MICADO cold optics, there remain many places where CTE differences will play a role (e.g. mounting of filters, grisms). Interfaces with CTE-differences will be dealt with in CAD design software. As the optical design is primarily made at operational temperature, which is quite different from the actual part production and assembly temperature (at ~293K), it is important to resize the 3D optical model output data from, usually, Zemax. Zemax itself has the resize functionality but it is known for years now that the resizing of the optical file in Zemax is not always correct, especially when using different materials in one optical model and/or different temperature levels. This problem exists by the nature of object positioning in Zemax: a sequential positioning of individual optical surfaces, from center to center on the optical axis. However, in reality a lens is normally not mounted on its center point but somewhere near its perimeter; the real mounting interfaces are not present in Zemax. This can lead to offset errors.

To solve this issue the resizing of the optical model will be performed in a CAD environment where the actual mounting interfaces are present. This resizing strategy works on part and assembly level and can cope with different material and temperature levels based on real mounting interface locations. However, this dictates that in an early phase of the final design there must be a detailed plan on where mounting interfaces and temperature borders will be positioned. An advantage of this early focus on interfaces will be the available input into and

interpretation of the Monte Carlo analysis data possibly to the advantage of the optical performance and/or ease of MAIT.

7.4 Adjustments

After only one iteration, the Phase A Monte Carlo data on static positional and angular errors allows for a design, production and assembly approach that excludes the necessity for any adjustments. By minimizing the amount of interfaces, and using milling in assembly[2], it is possible to produce and assemble a complete substructure and only in the end verify its performance.

The grisms in the auxiliary arm are the only parts considered for alignment. This is due to the angular error between ruling and its outer edges. This will be solved implementing a once-only compensation milled in the wheel using the measured angle deviation.

7.5 Straylight

The optical beams are separated and shielded as much as possible. Properly designed baffles will be used and all other structure material will be kept as far off the beams as possible to reduce unwanted reflections. If beams inevitably come close to the wall, and effective baffling is not possible, the wall surfaces will be shaped in a wave-like finish (see Figure 74) which was effectively used in SPIFFI and X-Shooter.

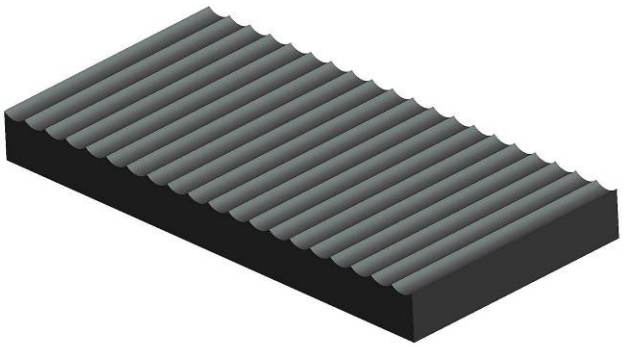

Figure 74: Anti straylight surface shape as used in X-shooter, depth 1 mm pitch 5 mm. Surface is coated to further reduce straylight.

All interior surfaces of the instrument will be coated with low-reflective black paint coating called PUK, applied by MAP in France. This surface coating has successfully been used in X-shooter, one of the darkest instruments at the VLT, and is also very effective at longer wavelengths. Measured PUK test samples show reflections of 2 % at 10 micrometer, 0.6 % at 5

[2] Milling in assembly: assemble a number of less accurate parts and mill in one setup all accurate interfaces so the end result is one large accurate part. Successfully used in JWST-MIRI and MATISSE on, for instance, the optics housing. Improves overall accuracy and performance and significantly reduces alignment and verification time.

micrometer and 0.35 % at 3 micrometer wavelength. These values were measured at an incident angle of 30 degrees.

To reduce straylight and hotspots, gaps between parts will be shaped like a labyrinth where necessary.

7.6 General Material Selection

7.6.1 Structural Materials

Structural material selection for cryogenic purposes is based on:

- Mechanical properties
- Thermal properties
- Machinability
- Ease of coating
- Retaining its shape in time and in different temperature environments (low initial internal stress level/ease of stress relieving)
- Predictability of shrinkage
- Ease of cleaning
- Outgassing behaviour
- Availability
- Ease of part outsourcing
- Cost

Aluminium alloy Al 6061-T651 suits these requirements very well and has successfully been used in many astronomical cryogenic instruments. There is extensive experience with all manufacturing aspects of this material.

Titanium and stainless steel are common alternatives in areas of high stress and/or areas that need conductive insulation, such as the instrument support struts inside the cryostat.

7.6.2 Mirror Materials

The curved mirrors will be machined out of optical grade aluminium alloy Al 6061 as their parabolic shape is easier to produce in aluminium using Single Point Diamond Turning (SPDT) than by polishing in a glass like material. If scattering by the residual grating like pattern is unacceptable, post polishing of the surface is a possible solution.

The flat mirrors will either be made of aluminium 6061 or a glass type material (such as Fused Silica) much dependent optical specifications (surface roughness and shape), mass and cooling time constraints.

7.7 Surface treatment

All aluminium surfaces will have an alodine protective coating which is also a good primer layer for the PUK. PUK will not be applied on mounting surfaces to eliminate the risk of flaking and for optimal heat transfer. Sharp edges will be chamfered for the same reason.

If aluminium gears are used they will be anodized with a Teflon impregnation treatment acting as a lubricant.

Aluminium mirrors will be gold coated for maximum reflection across the 0.78-2.4μm wavelength range.

7.8 Manufacturing

Main manufacturing techniques commonly used are:

- Milling/lathe
- Lapping/polishing
- Single Point Diamond Turning (SPDT)

Manufactured parts will be measured to check compliance. Al 6061 parts will be stress relieved (aged) by heat treatment to ensure a non-deforming part during cool down and operation. This heat treatment is applied near the end of the production stage just before the final production of all the accurate features and has proven its worth in many cryogenic projects.

Dependant on surface specifications, the aluminium mirrors could undergo another heat treatment procedure to recrystallize the material structure after rough milling. This can lower the micro roughness of the optical surface.

7.9 Isostatic Mounting

A stress-free mounting is most important for positioning of the optical elements to minimize any deformation due to external forces.. The only correct way to construct a near stress-free mounting between two parts is by an isostatic connection. This means that all six degrees of freedom of an interface are defined separately and only once. In practice this means that in most cases parts will be mounted on three points and aligned using notches or dowel pins and corresponding holes for correct positioning.

The three point mounting produces a well defined shrinkage centre, guaranteeing a good alignment of, for instance, the curved surface of a mirror. Larger shrinkage differences are mostly dealt with by using leaf springs and/or by introducing a third intermediate material that shrinks even faster referred to as a differential shrinkage compensator.

7.10 Optics Mounting

As explained in Section 7.4, milling in assembly is used to mill the most important accurate mounting surfaces, especially for the mounting of the optics. This will lead to optics being mounted on the outside of the mechanical structure thereby facing inward through a hole in the wall.

7.10.1 Aluminium mirrors

The design of the curved (and perhaps flat) aluminium mirrors will be very similar to the large mirror designs used in X-Shooter:

Figure 75: M7 mirror usedin X-shooter. Diameter ~0.35m

To reduce the transfer of deforming forces from structure to mirror to a minimum, leaf springs are part of the structure while the mirror has labyrinth grooves that centralize any deformation.

7.10.2 Glass type mirrors

If this material is chosen for flat mirrors the mounting method will be quite different. In that case the mounting strategy will be similar to the one used in SPIFFI:

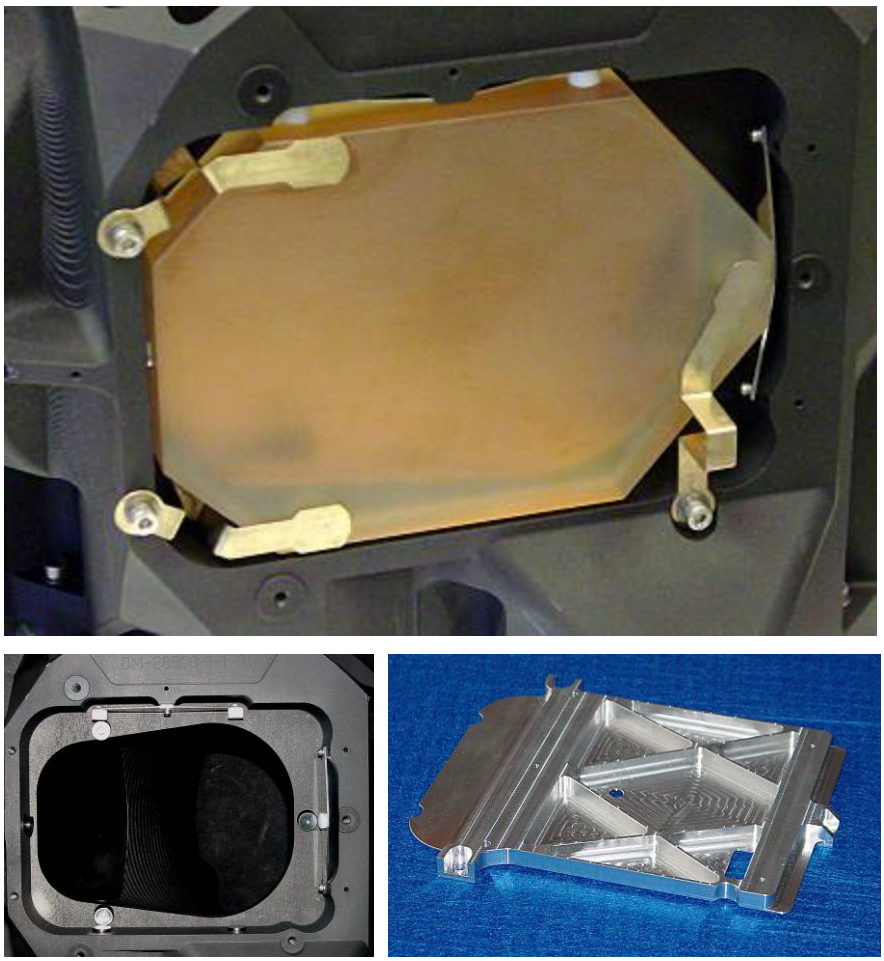

Figure 76 : Mounting of large flat non-aluminium optics, as used, for example, in SPIFFI. Copper leads are added for lower thermal resistance.

This method is specifically suited for mounting of heavy large flat optics and at the same time assuring a minimum amount of deformation. Using 3+2+1 half balls in sockets (left lower image) it is possible to lock al degrees of freedom and to decouple any bending or torsion forces from the structure. The leaf springs compensate for the large shrinkage differences between optics and structure. The fixation plate (lower right image) pressing on the backside of the mirror uses leaf springs that also put pressure on thermal leads (copper), added to achieve an acceptable cooling time. For MICADO the amount of leads could visible in the top image be tripled adding one to each surface in contact with the mirror (except the ones on the mirror front), its necessity TBC by the cool down specification and thermal modelling.

7.10.3 Filters/Grisms

To mount the many round filters, two mounting methods are considered: either a tool-less mounting clip, like the one developed for MATISSE, or the more classical approach used in MIDI using notches and short leaf springs.

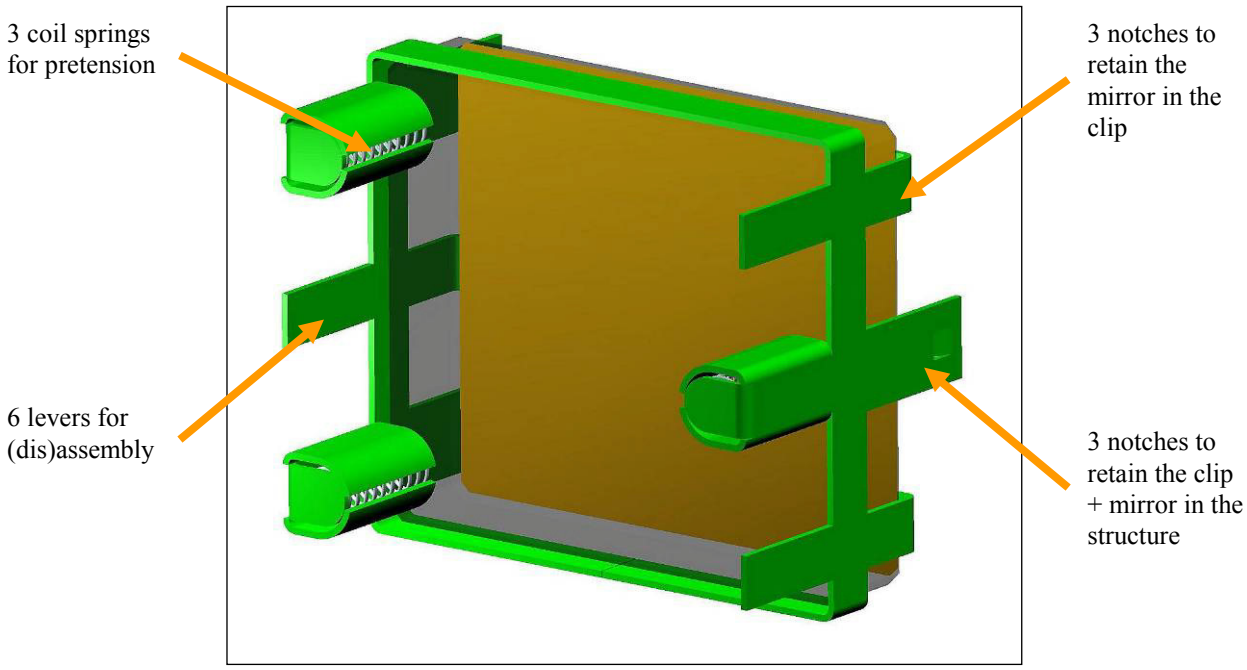

Figure 77: Filter mounting clip as designed for MATISSE. Naturally its outer shape will be round for the MICADO filters. The springs apply the fixation forces while the notches lock on the filter wheel. For MICADO the coil springs will be replaced by leaf springs to reduce the overall height so the filter wheel can be designed as thin as possible as clearance is limited.

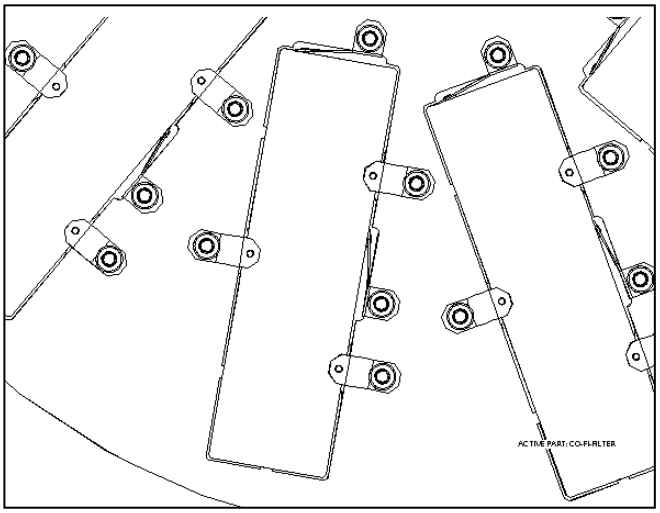

Figure 78: Filter mounting as used in MIDI.

The clip does not lend itself to mounting of a grism as the rotational position around the optical axis is not very well defined. Instead the MIDI method suits this requirement very well. As stated in Section 7.4, the as-made grism ruling angle will determine the exact position of the static mounting points in the wheel (a once-only adjustment).

7.11 Thermal Connections

At some places the isostatic mounts might not be sufficient enough for a good thermal connection of the structures. In that case flexible copper braids are used as a bypass to improve the thermal connection without loosing the isostatic principles.

7.12 Earthquake Analysis

The current design is not mature enough to carry out an earthquake analysis delivering sensible results as the results highly depend on a much more detailed design of the intermediate structure as well as the instrument support assembly, together supposed to be the weakest link regarding stiffness around the optical axis (probably the first eigenfrequency mode).

The vibration characteristics will be researched in detail in a later stage (Phase B, PDR). However, as the NOVA/ASTRON team is accustomed to designing both earth and space based instrumentation its clear any vibration constraints will be dealt with in the usual manner; using it as an input constraint when further designing MICADO.

8 CRYOGENICS

8.1 Cryogenic Requirements

8.1.1 Cryogenic Operations

The following standard cryogenic operational modes will be used:

Cool down mode

- Flushing with dry nitrogen
- Initial evacuation
- Cool down
- Stabilisation
- Sorption pump regeneration

Steady state and failure modes

- Continues supply LN2
- Defogging entrance window
- Emergency pumping when pressure and temperature are rising
- Sorption Pump regeneration

Warm-up mode

- Electric heater controlled warm-up with possibility of dry N2 warm-up stage
- Re-pressurization with interlock via a vacuum valve

8.1.2 Temperature Levels

Figure 79 shows the temperature levels and the calculated heat loads on each temperature level.

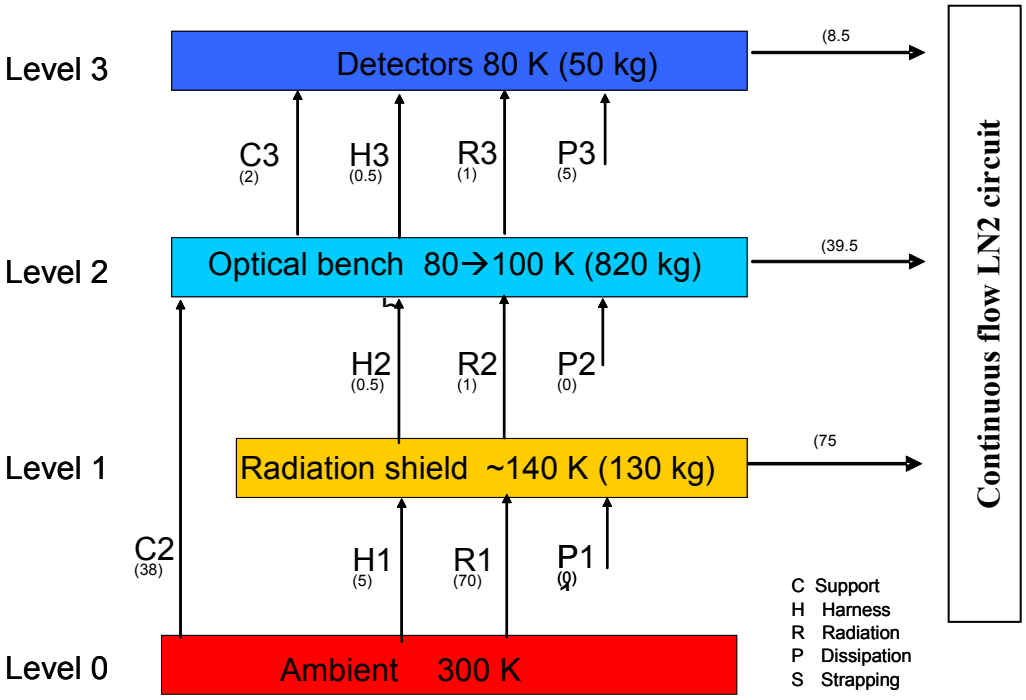

Figure 79: MICADO temperature levels and heat loads

8.1.3 Temperature Stability

Determining the needed static and dynamic temperature stability are important inputs for the cooling design. If the system needs low gradients this means that the cooling power needs to be distributed evenly over the structure. It might even be necessary to actively control the gradients over for instance the optical bench by placing heaters at the cooling points so that cooling power can be regulated.

Approach for the MICADO Phase A is to do a rough estimate of the needed stability. This is performed by the following steps:

Estimate of the Static temperature stability:

1. Build a simplified optical bench with the same overall dimensions as the MICADO design, a square box of 1x1 meter with 10 mm wall thickness

2. Apply a temperature gradient over the 1x1 meter structure and calculate de resulting deformation of this structure
3. Translate the optical bench deformation to the most demanding mirror(s) in the system which are for MICADO the parabolic and aspheric mirror
4. Compare deformation and tilt with the specified tolerance for this mirror
5. Calculate maximum allowable temperature gradient based on the given tolerance

Estimate of the Dynamic temperature stability

1. Determine the optical path length from each mirror to the detector
2. Calculate tilt angle for one pixel movement of the image over the detector
3. Calculate what temperature gradient is needed to equal the calculated tilt angle
4. Divide the smallest gradient over all mirrors in the optical path, this is the gradient which gives as result the allowed gradient variation over the whole structure
5. Calculate the heating power needed for such a gradient variation over the whole structure, this gives an indication of the difficulty to realize this gradient .

8.1.3.1 Static

Typical position tolerance specification for the MICADO main channel optical components vary from 0.5 down to 0.05mm. The allowed tilt of the optical surfaces varies from 1 until 0.01 deg, which results in respectively 4.4 and 0.04 mm tolerance in z-direction on the mounting points of the optical component over a 250mm length

Steady state temperature gradients will result in displacements of the optical components. Following types of temperature caused displacement are indentified.

- Temperature difference between the mounting points of the optical component, this will result mainly in an tilt of the optical surface
- Temperature gradients over the optical bench result in displacement of the optical components

Figure 80 shows a square box of 1000x1000x1000mm with a wall thickness of 20mm. A temperature gradient of 10 deg Kelvin is applied across the box, which results in a maximum overall deformation of about 0.032 mm between the two temperature points.

This gradient results in a displacement and tilt of the optical components. The displacement will not be larger then 0.032 mm; and tilts over 250mm length are in the order of 0.006 mm, as shown in the Y displacement Figure 81.

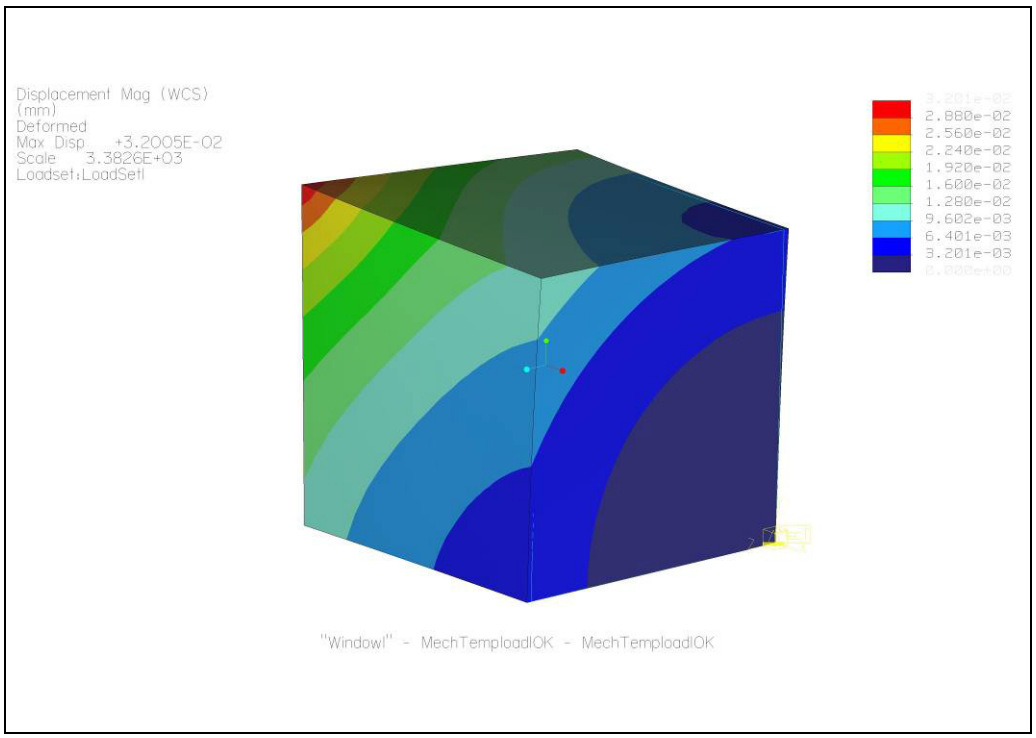

Figure 80: Deformation due to a 10 K gradient over the 1x1 meter box

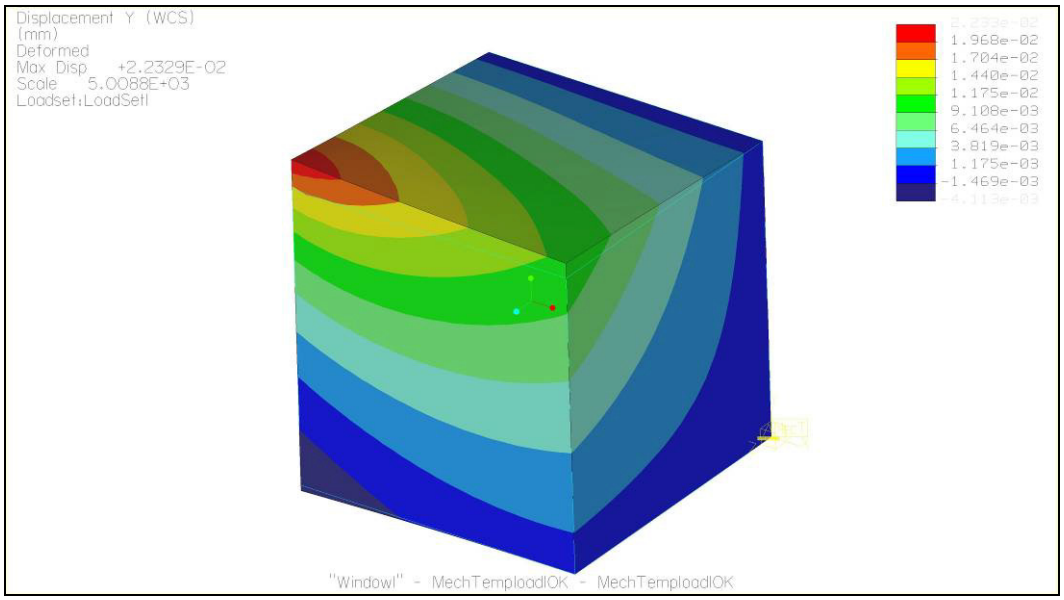

Figure 81: Deformation in Y direction due to a 10K gradient over the 1x1 meter box

In the following paragraphs, the results are compared with MICADO tolerance specification.

Table 8: Allowed static temperature gradients over the optical bench

	Specified tolerance [mm]	10 deg displ. and tilt [mm]	Allowed temp. gradient [K]
displ	0.02	0.032	6.3
tilt	0.02	0.006	33.3

Table 8 shows that the largest allowable gradient steady state over the whole optical bench shall not be larger then 6 Kelvin for a 1x1x1 meter optical bench. The actual longest distance between two optical components within MICADO is around 900 mm. The maximum allowable temperature gradient between mirror mounting points is 33.3 K. So it can be concluded that displacements due to temperature gradients result in larger errors then the temperature tilt effect. These values are based upon 100% usage of the tolerance budget however many other types of errors use the same budget, for instance the manufacturing tolerances.

The static tolerance budget is calculated by a Monte Carlo analysis. This statistical method random varies the position and tilt of all the optical components in the system within the ranges of the predefined strehl ratio of the system. For instance diffraction limited. The outcome is the maximum allowable displacement in x,y,z direction and tilt around all three axis for each optical surface in the system.

The sum of the following error types use up the static tolerances budget. The CTE, orientation and hysteresis effects are in practice close to zero percent compared to the more significant errors like temperature gradient induced displacements and fabrication errors.

Table 9: Tolerance budget distribution

Percentage of tolerance	Type of location or tilt error
80%	Fabrication and assembly tolerances
20%	Steady state temperature gradients over the optical bench
0%	CTE variations within the optical bench material
0%	Deformation due to orientation difference between fabrication/measurement en usage orientation
0%	Time and temperature dependant internal stress effects/hysteresis (heat treatment solves this error)

8.1.3.2 Dynamic

The dynamic tolerance budget is driven by the science case which needs the highest stability over time. Specifying the dynamic tolerance is done by determining how many pixels the image is allowed to move over a certain time period, for instance 1 pixel shift during 1 hour. The distance between the detector pixels in the case of the H4RG-15 detector is 15µm.

The most demanding science case derived from the Operational Concept (given in RD3) requires multiple short exposures to be directly co-added without dithering. The cadence for this is up to 30sec. In addition, the astrometry study (RD5) requires that the pixel scale is calibrated to 1/100 of a pixel. The dynamic tolerance should be such that it does not impact the calibration, and is therefore set at 1/200 pixel in 30sec. Since the baseline detector is the H4RG-15 (with a 15micron pixel pitch), this specification corresponds to 9 µm/hour.

The dynamic thermal stability is determined by the variation of the temperature gradients between the optical components and not by the overall temperature rise or drop of the instrument. This means that the temperature differences between the optical components should be constant. If the temperature gradients vary then this will result in tilts of the optical surface which then again results in image movement over the detector.

In most systems the most sensitive mirror is the one which is furthest away from the image plane. For MICADO this is fold 3 in the main image arm. However, for this worst case calculation the first mirror (M1) is used together with its distance from the detector. M1 is a 250mm wide mirror with a distance to the detector of 4300 mm, which results in a tilt of 0.57µm to realize a 9 µm movement on the detector.

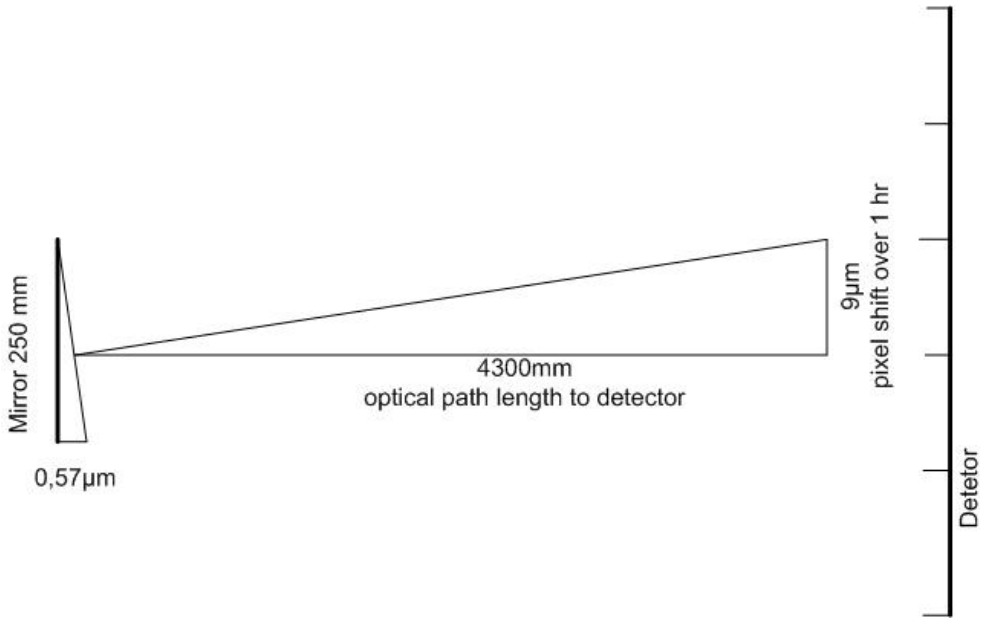

Figure 82: Image shift on the detector due to temperature induced tilting mirror

The required temperature gradient over 250mm length to realize the 0.57µm tilt is about 1 K looking at the previously calculated gradient over the 1x1 meter box. The required gradient should be divided by the number of mirrors in the system because in the worst case each mirror will add the same error. This brings the maximum gradient over the whole structure at 0.11K.

The following analysis shows the amount of power needed to create such a gradient of about 0.11K over a 1x1 meter structure with a wall thickness of 10mm.

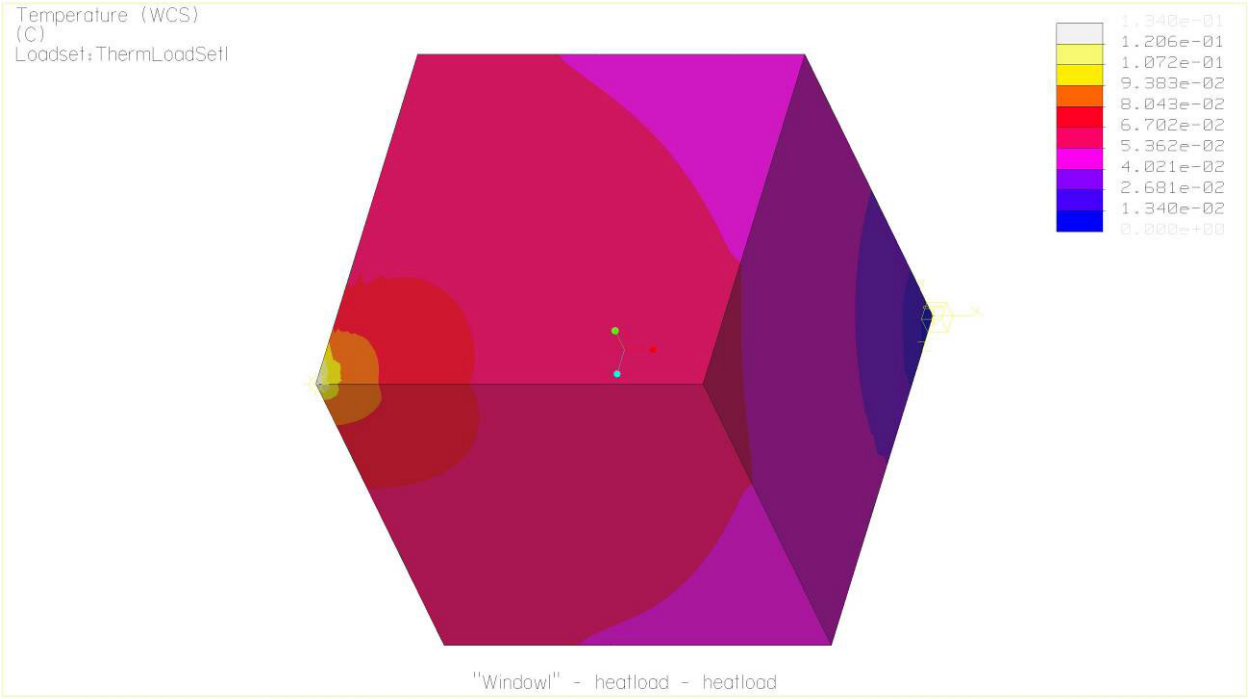

Figure 83: Temperature gradient due to 100W heat load diagonal over the 1x1x1 meter box

This results in a 100 Watt heat load to realize a 0.13K gradient over such a structure. The 100 Watt is unrealistic looking at the for instance MICADO heat loads at steady state temperatures which are significantly lower.

8.1.3.3 Temperature Stability Conclusions

The calculated static temperate gradient over the MICADO optical bench which realizes a displacement and/or tilt of the optical components which uses 100% of the main arm tolerance budget is 6 K or higher.

The calculated dynamic temperature gradient variation which results in a 10µm movement over the detector is 0.11K. The amount of heat flow needed to realize such a gradient is about 100

Watt. This is high compared to, for instance, the 20-30 Watt (TBC) heat load on the optical bench at steady state temperature.

It is assumed is that the auxiliary arm has approximately the same values because optical path length and mirror dimensions are approximately the same

Conclusion: thermal stability issues are not a high risk for MICADO. Any cooling concept should be able to realize these thermal stability levels.

8.1.4 Cool down

The cool down time of the cryostat should be < 48 h from start of cool down to operational condition only the filters are allowed to lack behind.

The cool down procedure is executed in three stages. First the system will cool the radiation shield to 160K. Then the optical bench can be cooled down. When the optical bench reaches 100K, the detector can be cooled to its operation temperature. This order is done to protect the optics from contamination. The cool down and warm-up rate of the detector must be less than 0.5 K/min.

8.1.5 Warm-up

The emergency warm-up time should be < 24 h until the instrument can be opened. The hold time of the cryostat in a stable situation should be > 24 hours with a goal of > 30 hours.

8.2 Cooling System Design

There are a number of reasons to choose a LN2 continues flow cryostat rather than a LN2 bath cryostat:

- Cooling is delivered where needed
- Detectors can be placed anywhere in the cryostat, there is no need of being close to the LN2 bath
- Mass of cryostat will be lower
- Dimensions of cryostat are smaller
- Refilling sequence is independent of bath volume
- Might be possible to combine pre-cooling and steady state cooling system. A bath cryostat needs an extra continues flow pre-cooling circuit any way to limit the cool-down time

8.2.1 LN2 Continuous Flow

This cooling method is generally used for the pre-cooling. The principle is based on circulation of liquid nitrogen through pre-cool lines and heat exchangers, also called cooling pads (see Figure 85) that are placed at strategic locations in the cryostat. An assigned pre-pressure in the storage tank is necessary to pump the nitrogen through the cooling circuit(s).

The cool down sequence for which the cooling circuit is optimized should cool down first the heat shield then the optical bench and finally the detector unit. During the steady state phase the sequence is reversed. First the detector unit is cooled then the optical bench and last the heat shield. This way the detectors will have the lowest possible temperature because they are first in the series. This series circuit concept is shown in Figure 84. Other possible circuit concepts are also shown for comparison.

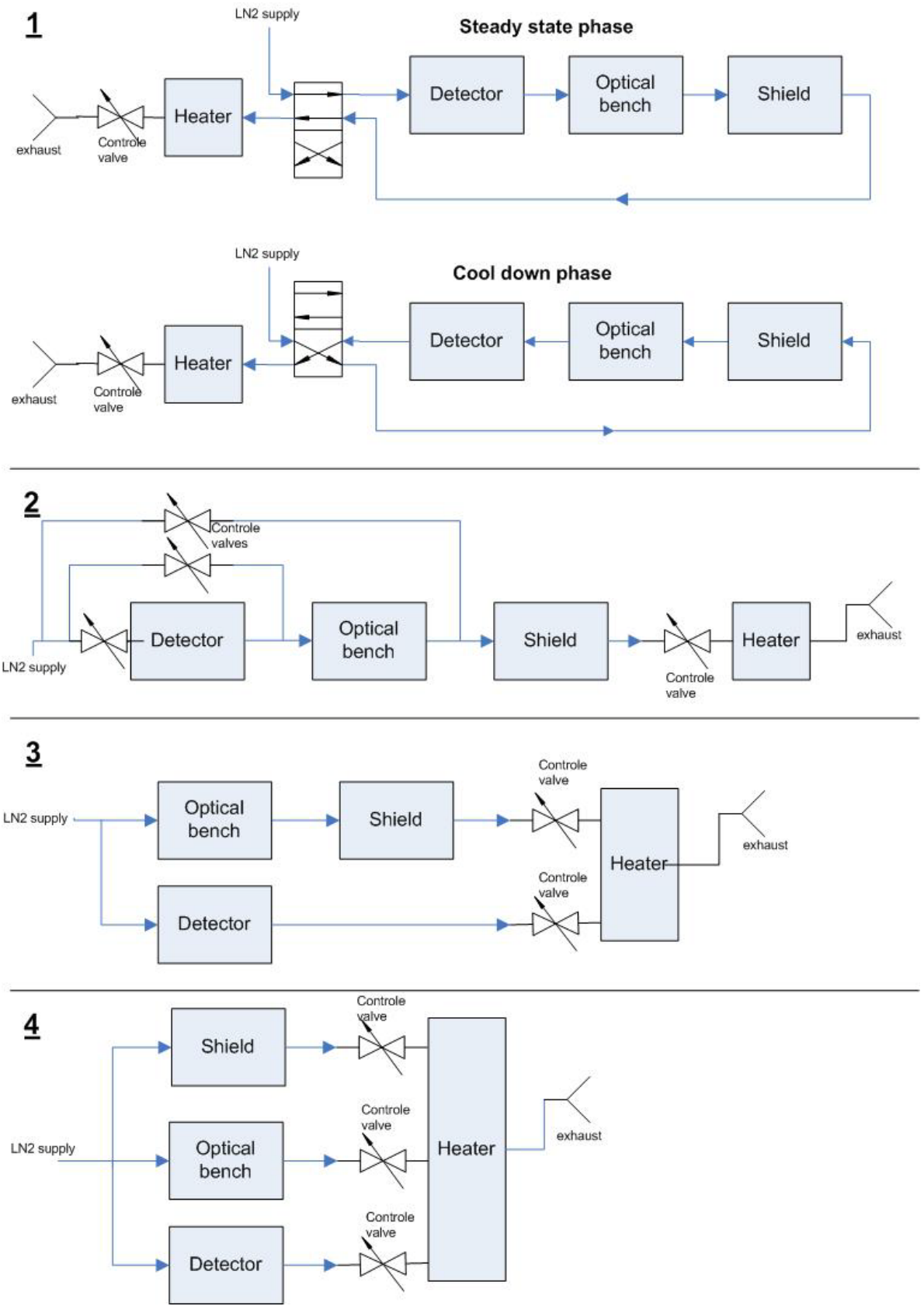

Figure 84: Serial and parallel circuit concepts

The advantage of the series concept (1) is that the LN2 flow through the circuit can be reversed so that the same circuit is used for both cool down and the steady state phase. This is only possible when the desired cool down and steady state characteristics are compatible. A concept with maximum control is shown in circuit concept 4 which is a parallel circuit. Each temperature level is now adjustable by controlling the exhaust valves.

The cooling pad arrangement within each temperature level can be divided into parallel branches where necessary. The various cooling pads are connected using flexible stainless steel tubes. The pads will be mounted in locations where the heat loads are high to minimize gradients for instance close to the V-rod support structure.

The design of the heat exchanger pads is shown in Figure 85. For the thermal modeling, the following cooling power per cooling pad is specified by ESO:

At 300 K, 80 W
At 100 K, 8 W

For cooling pads connected in series the first pad will have 100 % cooling power, the second pad 95 % and the third pad 90 %.

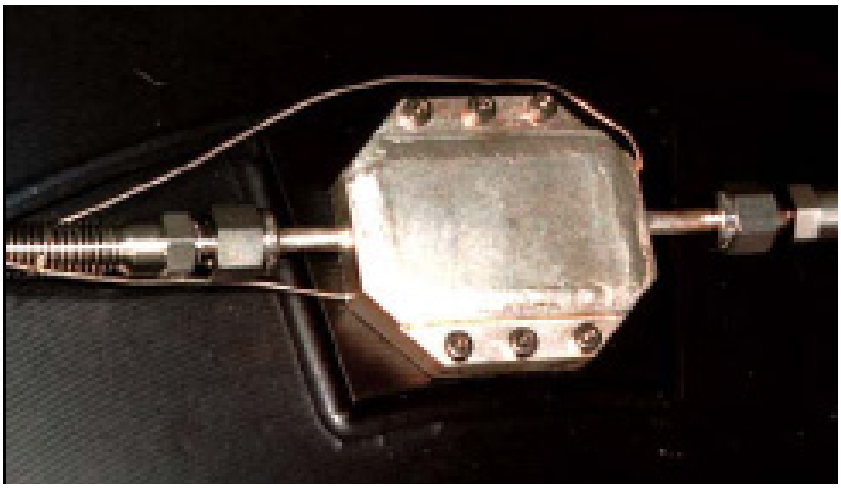

Figure 85: LN2 heat exchanger (as used in CRIRES)

8.2.1.1 Open System

The open LN2 cooling system is equipped with a control unit that contains a PT100 temperature sensor which is mounted on the outlet splitter/combiner block followed by a heater block and a controlled exhaust valve. The heater block will ensure that no liquid nitrogen can flow out of the cryostat. Additionally a second heater block could be added in the exhaust line which will warm up the cold gas to ambient temperature before it leaves the exhaust.

8.2.1.2 Closed System

The LN2 circuit could also be used in closed mode by a feed back into the dewar. In this case the LN2 transport through the circuit can no longer be realized by applying pressure on the dewar. The flow of LN2 through the circuit is realized by for instance a warm long shaft or cold submersible Barber-Nichols pump. Figure 86 shows the series circuit in a closed system.

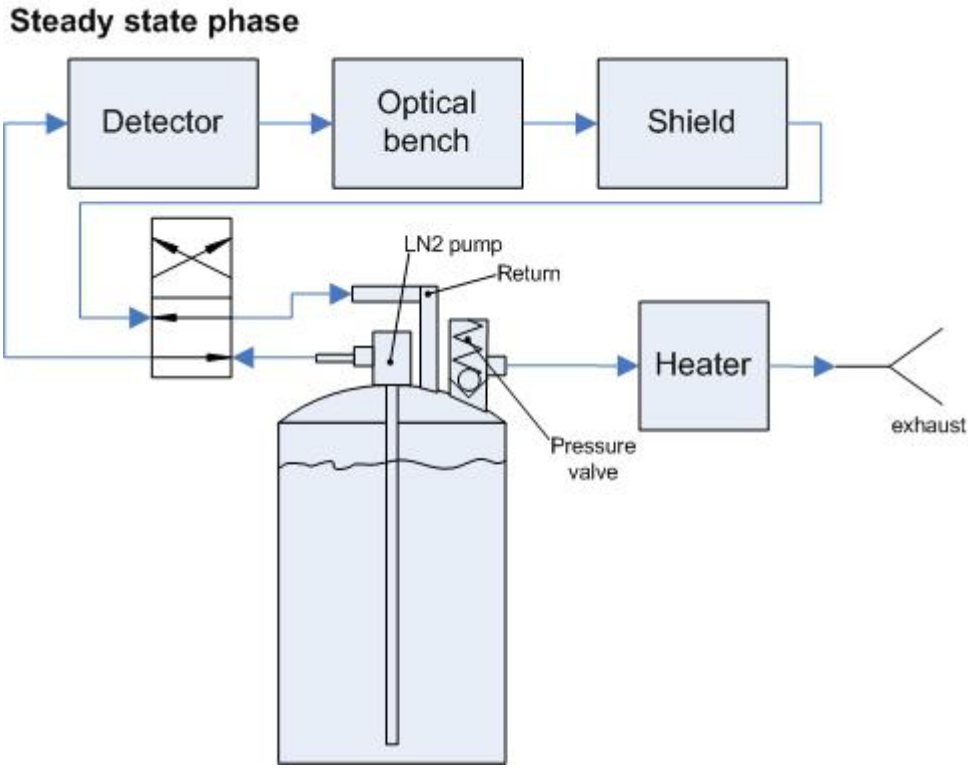

Figure 86: Closed continuous flow system

8.2.1.3 Detector Cooling

Controlling the detector temperature during cool down and steady state phase requires some thermal decoupling from the LN2 circuit because temperatures are bound to be fluctuating due to large cooling power fluctuations which are inherent to the LN2 phase changes. Such a system would look like that shown in Figure 87. The additional mass and resistance is added to realize damping for fast temperature changes.

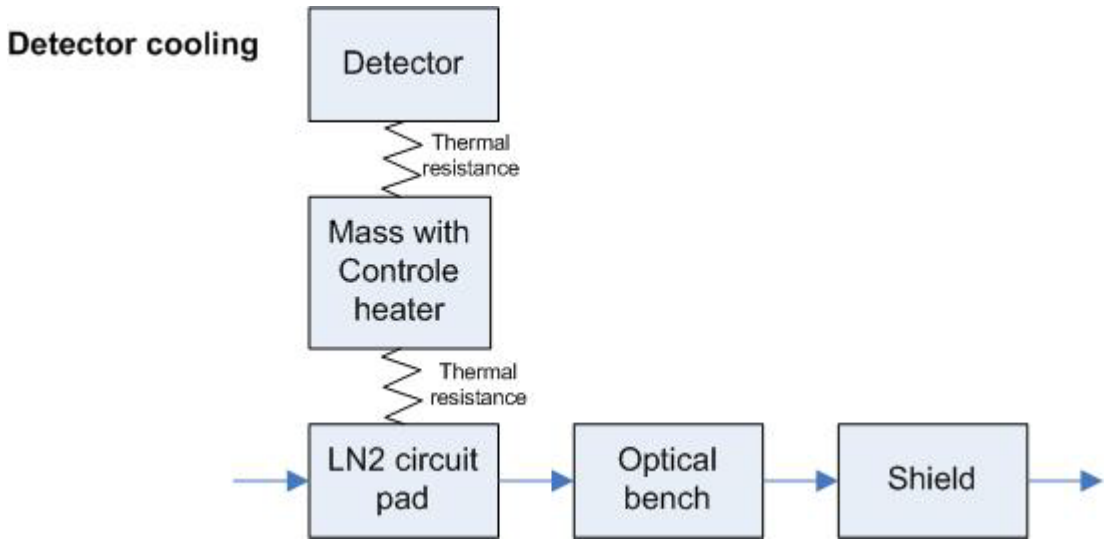

Figure 87: Detector temperature control

Dimensioning the damping RC circuit is done by determining the frequency or speed of temperature change which should be filtered. Assuming that stable temperatures over 15minutes (ΔT=15 min) are specified, the damping frequency should be about 4 times this which brings the damping frequency at 0.00027Hz.

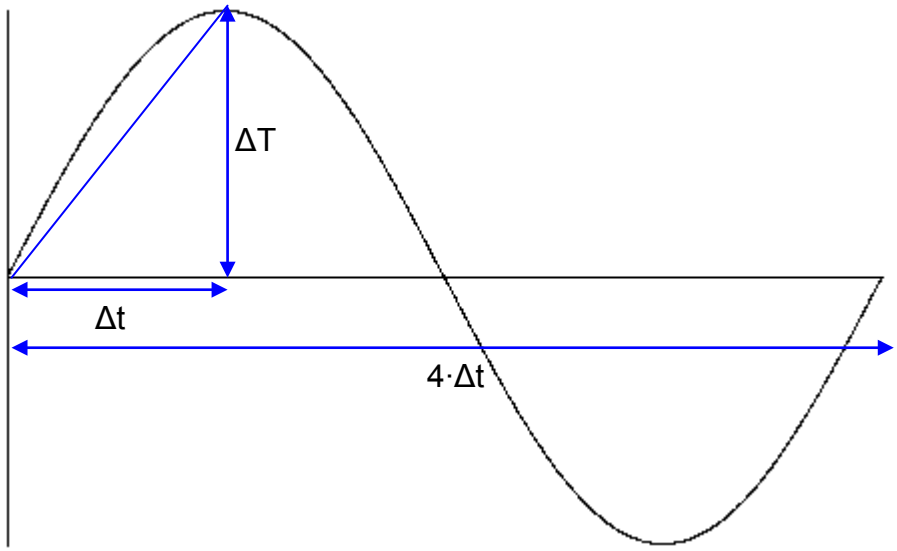

Figure 88: Translation of temperature variation to frequency

Now the resistance and capacitance can be determined by applying the following formula, which determines the 3dB cut off frequency. Assuming a resistance of 1K/W this will result in a 0.65 kg aluminium mass.

$$f_c = \frac{1}{2\pi\tau} = \frac{1}{2\pi RC}$$

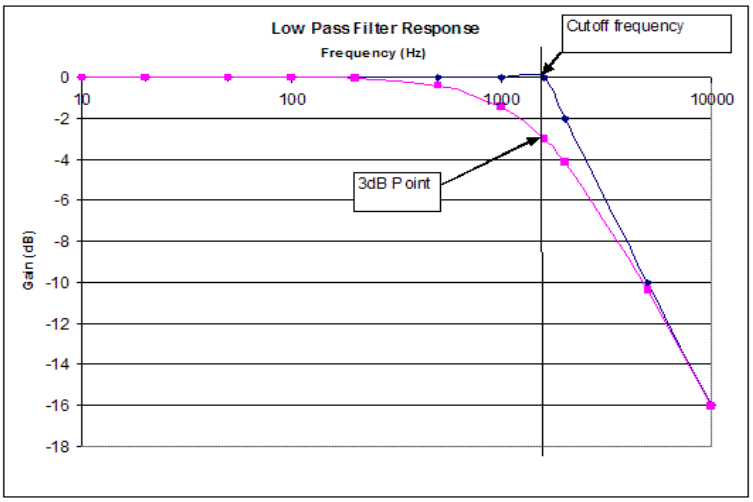

Figure 89: Low band pass filter calculation

This RC damping system in-between the LN2 cooling circuit and the detector unit should give sufficient decoupling so that temperature changes over 15 minute or higher will be damped significantly. It also realizes additional decoupling between the detector unit and the cooling circuit which enables temperature control by, for instance, a 5 Watt electric heater. This 5 Watt heater in combination with the 1K/W resistance will realize a temperature control range of 5 Kelvin.

8.2.2 Concept Choice

There are two main concept choices to be made for a LN2 continuous flow cryostat.

- Open or closed circuit
- Parallel, serial or combined circuits

Although the closed system will have a higher efficiency concerning LN2 usage, the adopted choice is the open system. The open system is a straight forward system which has been used many times previously to achieve LN2 temperatures. The closed system needs a cryogenic pump and pressure valve which will reduce the reliability of the cooling system.

The choice for serial or parallel circuit is driven by the temperature control during cool down. First there should be determined if it is possible to passively control the cool down order by dimensioning cooling capacity correctly for each temperature level. This is possible by specifying the resistance between cooling pad and for instance the optical bench. The detector temperature can be controlled by an electric heater. Detailed design of the cooling circuit within each temperature level shall be done during Phase B of the project.

8.3 Thermal Behaviour

8.3.1 Heat Loads

Table 10 shows the major heat loads on the cryostat (see also **Error! Reference source not found.**).

Table 10: Heat loads per temperature level

Conductivity	Heat load on detector circuit	Heat load on Optical bench circuit	Heat load to radiation shield circuit
Optical bench mounting (Ti V-rods)		38 W	
Harness/cabling		0.5W	2W
LN2 circuit piping		1W	1W
Support radiation shield			
Radiation			
Vacuurm vessel → shield			70W
Shield → Optical bench		1W	
Window → Optical bench		<1W	
Power dissipation			
Detectors	3W		
Temperature control heaters	Max 5W		
Total heat load	Ca 8W	41W	73W

V-rod Instrument Support

The V-rod instrument support is based upon the X-shooter V-rod design. Overall dimensions of the MICADO V-rods are approximately the same. However they need to support a mass that is about 8 times larger, and therefore the hinge cross-section should be increased linearly with the same factor. However MICADO only rotates around its vertical optical axis and not around two axes, as X-Shooter does due to its location in the Cassegrain focus. The hinge leaf springs are therefore only loaded by tensile forces. In combination with the X-Shooter safety factor of 3, this allows room for further optimisation by, for instance, increasing the leaf spring length. Increasing the cross-section by a factor 4 is therefore feasible and brings the heat load at steady state conditions to 38 W.

Further optimization is possible by using other material like G10 fibreglass. The Ti Triangle legs could be replaced by this material. This will then lower the heat leak from 38W to about 1W as shown in the calculation below.

G10 support structure

$k_{G10\_100K} := 0.5 \frac{W}{m \cdot K}$ $\quad \Delta T := 300K - 80K$

$A_{G10} := 0.25 \cdot \pi \cdot (20mm)^2$ $\quad L_{G10} := 200mm$

$G := \frac{A_{G10}}{L_{G10}} \cdot k_{G10\_100K}$ $\quad G = 7.854 \times 10^{-4} \frac{W}{K}$

$P_1 := \Delta T \ G$ $\quad P_1 = 0.173\,W$

$P_{tot} := P_1 \cdot 6$ $\quad P_{tot} = 1.037\,W$

Harness/Cabling

The heat load for the instrument harness is mainly determined by the copper cross-section that is needed to warm up the instrument within the specified warm up time. For the harness a length of 1 m is assumed. To warm up 1000 kg of Aluminium from 80 to 300 K within 24 hours requires a power input of about 2323 W. If the electrical power is supplied by a relative low (and safe) voltage of 48V this yields a current of 48 A. The main concern in current carrying wires is the occurrence of hotspots in the middle of the wires. The most critical situation arises at warm-up if the hot and cold sides of the wire are at room temperature. To limit the maximum temperature in the middle of the wire to about 50 °C, and taking into account supply and return wiring, the total cross-section amounts to 26 mm^2. To minimize the heat load on the 80 K Optical Bench, a heat sink of the harness on the Radiation Shield is needed.

Harness conductivity

$k_{Cu\_100K} := 454 \frac{W}{m \cdot K}$ $\quad \Delta T := 300K - 100K$

$A_{Cu} := 26mm^2$ $\quad L_{Cu} := 500mm$

$G := \frac{A_{Cu}}{L_{Cu}} \cdot k_{Cu\_100K}$ $\quad G = 0.024 \cdot \frac{W}{K}$

$P_1 := \Delta T \ G$ $\quad P_1 = 4.722 \cdot W$

Cooling Circuit Pipes

One could use stainless steel inlet and outlet pipes Ø17x20mm, which could be split-up into parallel circuits of, for instance, flexible stainless steel tubes of Ø8x12mm. The calculation below shows that the heat leak of the stainless steel cooling tubes is not a significant heat loss compared to the overall losses in the cryostat.

LN2 pipes conductivity

$k_{SS\_100K} := 10\frac{W}{m \cdot K}$ $\quad \Delta T := 300K - 80K$

$A_{SS\_tube} := 0.25 \cdot \pi \cdot \left[(20mm)^2 - (17mm)^2\right]$ $\quad L_{SS\_tube} := 200mm$

$G := \frac{A_{SS\_tube}}{L_{SS\_tube}} \cdot k_{G10\_100K}$ $\quad G = 2.179 \times 10^{-4}\frac{W}{K}$

$P_1 := \Delta T \; G$ $\quad P_1 = 0.048\,W$

$P_{tot} := P_1 \cdot 4$ $\quad P_{tot} = 0.192\,W$

Radiation

To minimize the radiation heat load from ambient on the cryostat, the use of Multi Layer Insulation (MLI) is assumed. The following equation developed by Lockheed Martin (C. Keller et al, Final Report: Thermal performance of Multilayer Insulations, NASA Contractor Report Number CR-134477, 1974) is used. The equation is valid for relatively ideal blankets with no seams or penetrations. MICADO will have a large surface with relatively few penetrations, and so the equation has been multiplied by a modest degradation factor of 5. The total outside surface area of the cryostat will be about 15 m^2. Therefore the expected heat load at the radiation shield is about 70 W.

The calculation below of the radiation load from the shield towards the optical bench results in only 1W due to the low temperatures of the shield and optical bench. The same calculation has been done for the radiation from the warm entrance window into the system which results in a load which is lower then 1 W.

Radiation

$C_s := 2.11 \cdot 10^{-9}$ Emperical constant

$C_r := 5.39 \cdot 10^{-10}$ Emperical constant

$N := 30$ Number of layers per cm

$N_s := 20$ Total numer of layers used

$T_h := 300$ Temperature hot side in Kelvin

$T_c := 120$ Temperature cold side in Kelvin

$\varepsilon_{tr} := 0.031$ Emissivity at 300K

$$q := \frac{1}{2} \cdot \frac{C_s \cdot N^{3.56}}{N_s + 1} \left(T_h^{\,2} - T_c^{\,2} \right) + \frac{C_r \cdot \varepsilon_{tr}}{N_s} \cdot \left(T_h^{\,4.67} - T_c^{\,4.67} \right)$$

$q = 0.994 \quad W/m^2$

$D := 1.6m$ Diameter shield cilinder

$L := 2m$ Length shield cilinder

$f := 5$ Degradation factor due to penetrations in the shield

$A := 2 \cdot \left(0.25 \cdot \pi \cdot D^2 \right) + L \cdot (\pi \cdot D)$ $\quad A = 14.074\,m^2$

$Q := f \cdot A \cdot q$ $\quad Q = 69.923\,m^2$

8.3.2 LN2 Usage

There are two phases in which LN2 is used.

Cool down

The cool down LN2 usage is determined by the mass and materials to be cooled down. The total mass (which includes detectors, optical bench with components, and radiation shield) is about 1000 kg. Almost all of the mass is made out of aluminium. The needed LN2 for a cool down to 80 K is about 1000 litres as shown in the calculation below.

Cooldown LN2 usage

$\text{Specific\_heat\_Alu} := 900\frac{\text{joule}}{\text{kg}\cdot\text{K}}$ $\quad \Delta T := 293\text{K} - 80\text{K}$

$\text{Entalpy\_LN2\_77\_273K} := 234\cdot 10^3\frac{\text{J}}{\text{kg}}$ $\quad \rho_{LN2} := 808\frac{\text{kg}}{\text{m}^3}$

$M_{Alu} := 1000\text{kg}$

$\text{Energie\_Alu} := \text{Specific\_heat\_Alu}\cdot M_{Alu}\cdot\Delta T$ $\quad \text{Energie\_Alu} = 1.917\times 10^8\,\text{J}$

$M_{LN2\_293\_70K} := \frac{\text{Energie\_Alu}}{\text{Entalpy\_LN2\_77\_273K}}$ $\quad M_{LN2\_293\_70K} = 819.231\cdot\text{kg}$

Cooldown LN2 volume

$V_{LN2\_tank} := \rho_{LN2}^{-1}\cdot M_{LN2\_293\_70K}$ $\quad V_{LN2\_tank} = 1.014\times 10^3\,\text{L}$

Steady State

The LN2 usage in this phase is determined by the heat load into the cryostat. The 2.6 litre/hour calculated is needed to keep the instrument at the required temperature levels.

24 hour steady state LN2 Volume

$\text{Heat\_load\_tot} := (73\text{W} + 38\text{W} + 8\text{W})$

$\text{LN2\_W\_ratio} := 45.6\frac{\text{W}\cdot\text{hr}}{\text{L}}$

$LN2_{stst\_usage\_hr} := \frac{\text{Heat\_load\_tot}}{\text{LN2\_W\_ratio}}$ $\quad LN2_{stst\_usage\_hr} = 2.61\cdot\frac{\text{L}}{\text{hr}}$

$LN2_{stst\_usage\_24hr} := 24\text{hr}\cdot LN2_{stst\_usage\_hr}$ $\quad LN2_{stst\_usage\_24hr} = 62.632\cdot\text{L}$

$LN2_{stst\_usage\_week} := 7\cdot LN2_{stst\_usage\_24hr}$ $\quad LN2_{stst\_usage\_week} = 438.421\,\text{L}$

Cooling Pads

The calculation below indicates that the number of cooling pads needed to keep the instrument at required temperature level will be 15. Of these, 9 are for the radiation shield, 5 are for the optical bench ,and 1 is for the detectors.

Number of cooling pads needed for steady state phase

$P_{pad\_stst} := 8W$

$Heat\_load\_tot = 119\,W$

$n_{pads} := \frac{Heat\_load\_tot}{P_{pad\_stst}}$ $\quad n_{pads} = 14.875$

8.3.3 Cool down Time

The cool down speed is limited by the amount of heat which can be removed by the LN2 pads. Each pad has a cooling capacity of 80W @ 300K and 8W @ 100K which brings the average cool down power between 300K and 100K to 44W.

Cool down time

$Specific\_heat\_Alu := 900\frac{joule}{kg \cdot K}$ $\quad \Delta T := 293K - 100K$ $\quad P_{pads} := 44W$

$M_{Alu} := 1000kg$ $\quad t_{cooldown} := 48hr$

$Cooling\_power := \frac{Specific\_heat\_Alu \cdot M_{Alu} \cdot \Delta T}{48hr}$ $\quad Cooling\_power = 1.005 \times 10^3\,W$

$n_{pads} := \frac{Cooling\_power}{P_{pads}}$ $\quad n_{pads} = 22.846$

This results in a total of 23 pads. Of these, 4 should be on the shield, 1 on the detector, and 18 on the optical bench for the cool down stage.

Since the number of cooling pads needed to keep the instrument at the required temperature levels during the steady state phase is only 15, one option to avoid having additional cooling pads would be to increase the cool down time to 31 hours.

8.3.4 Cool down Gradients

Since the optical bench is homogeneous built out of aluminium, and more than 9 cooling pads are used to cool it down, the temperature gradient will be very low. However the filters are thermally decoupled from the optical bench due to the filter wheel bearings and because of the contact resistance between the filters and aluminium wheel. The combined RC time for such a decoupled system will be close to 60 hr which results in cool down times exceeding 180 hr. The temperature differences between the optical bench and filter will exceed 120 K so that the mechanical mounting should be able to cope with these large temperature differences. Figure 92 shows the typical cool down temperature curve of such a system.

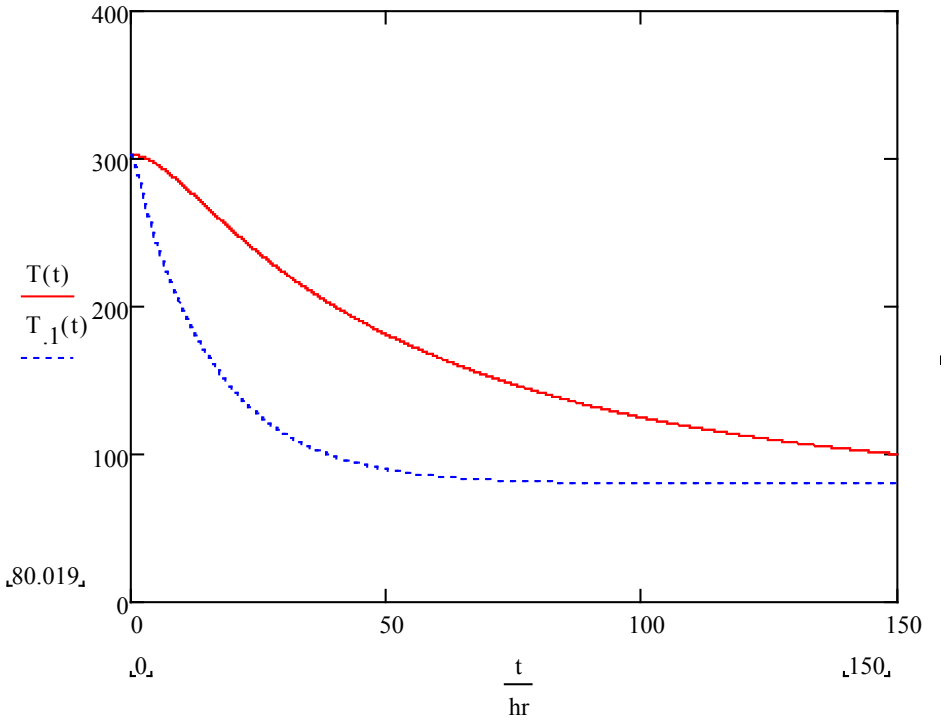

Figure 90: Temperature delay of filter

8.3.5 Warm-up

The warm-up is realized by electrical heaters which will be controllable for each temperature level. First the detector, then the optical bench, and last the radiation shield will be warmed up. The last stage of the warm-up could be speeded up by flushing dry nitrogen into the cryostat. This would level all temperatures in the cryostat, especially the decoupled filters. The needed amount of heating power is 2000 W for a 24 hour warm-up.

Warm up in 24 hours

$$\text{Specific\_heat\_Alu} := 900\,\frac{\text{joule}}{\text{kg}\cdot\text{K}} \qquad \Delta T := 293\text{K} - 100\text{K}$$

$$M_{Alu} := 1000\text{kg} \qquad t_{warmup} := 24\text{hr}$$

$$\text{Heating\_power} := \frac{\text{Specific\_heat\_Alu}\cdot M_{Alu}\cdot\Delta T}{t_{warmup}}$$

$$\text{Heating\_power} = 2.01 \times 10^{3}\,\text{W}$$

8.4 Vacuum

Before evacuation is started, flushing with dry nitrogen is required to remove water vapour from the cryostat. Every time the cryostat interior is exposed to atmospheric conditions, water vapour accumulates on the cryostat wall, the MLI and in the potential hygroscopic coatings of the optics. In particular, water accumulated in the coatings is, during evacuation, a potential hazard for the coatings. They may “boil off” when pressure drops. Nitrogen flushing removes this risk of coating freez off during cool down.

9 APPENDIX

A1: Primary arm Monte Carlo analysis data conversion to interface positional tolerances per interface

For the primary arm in **Error! Reference source not found.** the results are presented from the translation of optical Monte Carlo analysis data into average mechanical tolerances for every interface in its respective interface chain, starting from the focal plane to each optical surface.

Only input values of below 0.1mm or 0.1degree have been used to check the necessary manufacturing accuracy of each interface. Anything above 0.1 is easily achievable in production. The number of interfaces has been estimated on the basis of the current cold optics mechanical design.

Positional offset values have been translated into positional errors of the complete mounting plane (decenter Z) or set of two dowel pinholes (decenter X&Y).

Angular offset values have been translated into positional errors of one of the usually three mounting pads (tilt X&Y) or one of the two dowel pinholes (tilt Z).

The error stacking is done using the Root Sum Square (RSS) method, assuming partial random cancelation of error build-up (non linear).

The resulting values have been calculated for two scenarios:

- Separate part milling, interface values for each part:
    - 0.02mm Z offset of mounting plane and XY offset of dowel pinhole set
    - 0.01mm on Z offset of one of the three mounting pads or rotational XY offset of one of the two dowel pins.
- Milling in assembly, interface values for each of the three sub assemblies (results not shown in **Error! Reference source not found.**):
    - 0.03mm Z offset of mounting plane and XY offset of dowel pinhole set
    - 0.02mm Z offset of one of the three mounting pads or rotational XY offset of one of the two dowel pins.

Separate part milling would lead to rather strict accuracy demands on each single part contradicting the goal of easy outsourcing and low cost. Milling in assembly is chosen as the alternative reducing the stack of interfaces from about 6 to about 4. Using milling in assembly will therefore relax the interface accuracies by a factor of about 1.5.

For Phase B it is advisable to keep track of any interface changes (amount, location) and judge the impact on part/assembly tolerancing.

Table 11: Primary arm Monte Carlo analysis data conversion to interface positional tolerances per interface.

Primary arm			min	max	Base length, mm	Est. # of interfaces
Fold 1 & 2 (double pass)	radius of curvature	(mm)	lambda/10	lambda/10		
	decenter z	(mm)	-0,050	0,050		6
	decenter x	(mm)	-0,500	0,500	N/A	
	decenter y	(mm)	-0,500	0,500	N/A	
	tilt x	(degree)	-0,010	0,010	360	6
	tilt y	(degree)	-0,010	0,010	310	6
	tilt z	(degree)	-1,000	1,000		
Mounting plane offset error per interface, over # of interfaces, RSS, mm						**0,02**
One sided out-of-plane positional error per interface pad, over base, over # of interfaces, RSS, mm						**0,02**

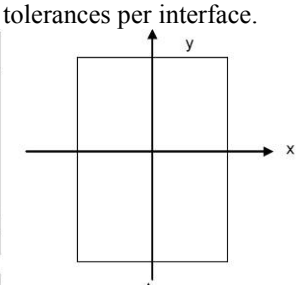

			min	max	Base length, mm	Est. # of interfaces
Parabolic collimator	radius of curvature	(mm)	-0,8	0,8		
	conic constant		-0,001	0,001		
	decenter z	(mm)	-0,100	0,100		
	decenter x	(mm)	-0,100	0,100		
	decenter y	(mm)	-0,100	0,100		
	tilt x	(degree)	-0,010	0,010	315	6
	tilt y	(degree)	-0,010	0,010	315	6
	tilt z	(degree)	-0,010	0,010	415	6
One sided out-of-XY-plane positional error per interface pad, over base, over # of interfaces, RSS, mm						**0,02**
One sided rotational displacement per pinholeset, over base, over # of interfaces, mm						**0,03**

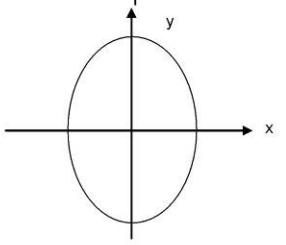

			min	max	Transfer base, mm	Est. # of interfaces
Fold 3	radius of curvature	(mm)	lambda/10	lambda/10		
	decenter z	(mm)	-0,100	0,100		
	decenter x	(mm)	-0,100	0,100		
	decenter y	(mm)	-0,100	0,100		
	tilt x	(degree)	-0,010	0,010	180	6
	tilt y	(degree)	-0,010	0,010	180	6
	tilt z	(degree)	-1,000	1,000		
One sided out-of-XY-plane positional error per interface pad, over base, over # of interfaces, RSS, mm						**0,01**

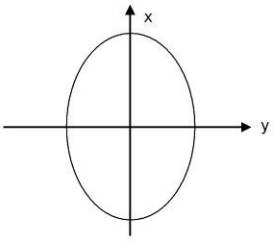

			min	max	Transfer base, mm	Est. # of interfaces
Fold 4	radius of curvature	(mm)	lambda/10	lambda/10		
	decenter z	(mm)	-0,100	0,100		
	decenter x	(mm)	-0,100	0,100		
	decenter y	(mm)	-0,100	0,100		
	tilt x	(degree)	-0,010	0,010	180	6
	tilt y	(degree)	-0,010	0,010	180	6
	tilt z	(degree)	-1,000	1,000		
One sided out-of-XY-plane positional error per interface pad, over base, over # of interfaces, RSS, mm						**0,01**

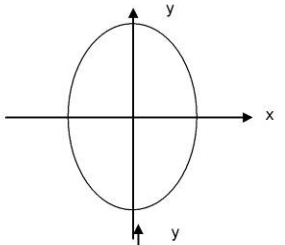

			min	max	Transfer base, mm	Est. # of interfaces
Aspheric	radius of curvature	(mm)	-0,1	0,1		
	conic constant		-0,001	0,001		
	decenter z	(mm)	-0,050	0,050		6
	decenter x	(mm)	-0,050	0,050		6
	decenter y	(mm)	-0,050	0,050		6
	tilt x	(degree)	-0,010	0,010	210	6
	tilt y	(degree)	-0,010	0,010	210	6
	tilt z	(degree)	-0,200	0,200		
Mounting plane offset error per interface, over # of interfaces, RSS, mm						**0,02**
Positional error in XY per pinholeset, over # of interfaces, RSS, mm						**0,02**
One sided out-of-XY-plane positional error per interface pad, over base, over # of interfaces, RSS, mm						**0,01**

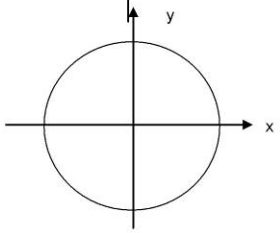

continued on next page

			min	max	Transfer base, mm	Est. # of interfaces
Toroidal	radius of curvature 1	(mm)	-0,2	0,2		
	conic constant 1		-0,001	0,001		
	radius of curvature 2	(mm)	-0,2	0,2		
	conic constant 2		-0,001	0,001		
	decenter z	(mm)	-0,050	0,050		6
	decenter x	(mm)	-0,100	0,100		
	decenter y	(mm)	-0,100	0,100		
	tilt x	(degree)	-0,010	0,010	180	6
	tilt y	(degree)	-0,020	0,020	180	6
	tilt z	(degree)	-0,050	0,050	240	6
				Mounting plane offset error per interface, over # of interfaces, RSS, mm		**0,02**
				One sided out-of-plane positional error per interface pad, over base, over # of interfaces, RSS, mm		**0,01**
				One sided rotational displacement per pinholeset, over base, over # of interfaces, mm		**0,09**

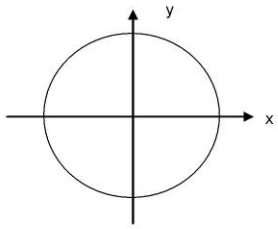

			min	max	Transfer base, mm	Est. # of interfaces
Spherical	radius of curvature	(mm)	-1,0	1,0		
	decenter z	(mm)	-0,06	0,06		
	decenter x	(mm)	-0,100	0,100		
	decenter y	(mm)	-0,100	-0,100		
	tilt x	(degree)	-0,050	-0,050	285	6
	tilt y	(degree)	-0,050	-0,050	285	6
	tilt z	(degree)	-0,050	-0,050	403	6
				One sided out-of-XY-plane positional error per interface pad, over base, over # of interfaces, RSS, mm		**0,10**
				One sided rotational displacement per pinholeset, over base, over # of interfaces, mm		**0,15**

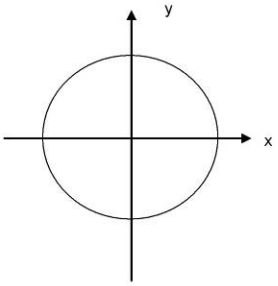

			min	max	Transfer base, mm	Est. # of interfaces
Detector	decenter x	(mm)	-0,100	0,100		
	decenter y	(mm)	-0,100	0,100		
	tilt x	(degree)	-0,100	0,100		
	tilt y	(degree)	-0,100	0,100		

compensator	decenter z	(mm)	-0,800	0,800

A2: Auxiliary arm Monte Carlo analysis data conversion to interface positional tolerances per interface

For the auxiliary arm in **Error! Reference source not found.** the results are presented from the translation of optical Monte Carlo analysis data into average mechanical tolerances for every interface in its respective interface chain, starting from the focal plane to each optical surface. The outcome is very similar to the primary arm results.

Only input values of below 0.1mm or 0.1degree have been used to check the necessary manufacturing accuracy of each interface. Anything above 0.1 is easily achievable in production. The number of interfaces has been estimated on the basis of the current cold optics mechanical design.

Positional offset values have been translated into positional errors of the complete mounting plane (decenter Z) or set of two dowel pinholes (decenter X&Y).

Angular offset values have been translated into positional errors of one of the usually three mounting pads (tilt X&Y) or one of the two dowel pinholes (tilt Z).

The error stacking is done using the Root Sum Square (RSS) method, assuming partial random cancelation of error build-up (non linear).

The resulting values have been calculated for two scenarios:

- Separate part milling, interface values for each part:
    - 0.02mm Z offset of mounting plane and XY offset of dowel pinhole set

- 0.01mm on Z offset of one of the three mounting pads or rotational XY offset of one of the two dowel pins.

- Milling in assembly, interface values for each of the three sub assemblies (results not shown in **Error! Reference source not found.**):
  - 0.03mm Z offset of mounting plane and XY offset of dowel pinhole set
  - 0.01mm Z offset of one of the three mounting pads or rotational XY offset of one of the two dowel pins.

Separate part milling would lead to rather strict accuracy demands on each single part contradicting the goal of easy outsourcing and low cost. Milling in assembly is chosen as the alternative reducing the stack of interfaces from about 6 to about 4. Using milling in assembly will therefore relax the interface accuracies by a factor of about 1.5, although the angular error stays the same (rounded off). This is related to the fact that the optics of the auxiliary arm is smaller in size, reducing the baseline length. However, in practice strict angular tolerances are easier to achieve in comparison to global positional tolerances so this will not be an issue during manufacturing.

For Phase B it is advisable to keep track of any interface changes (amount, location) and judge the impact on part/assembly tolerancing.

Table 12: Auxiliary arm Monte Carlo analysis data conversion to interface positional tolerances per interface.

Auxiliary arm			min	max	Base length, mm	Est. # of interfaces
Fold 1 & 2	radius of curvature	(mm)	lambda/10	lambda/10		
(double pass)	decenter z	(mm)	-0,050	0,050		6
	decenter x	(mm)	-0,500	0,500	N/A	
	decenter y	(mm)	-0,500	0,500	N/A	
	tilt x	(degree)	-0,010	0,010	360	6
	tilt y	(degree)	-0,010	0,010	310	6
	tilt z	(degree)	-1,000	1,000		
					Mounting plane offset error per interface, over # of interfaces, RSS, mm	**0,02**
					One sided out-of-plane positional error per interface pad, over base, over # of interfaces, RSS, mm	**0,02**

			min	max	Base length, mm	Est. # of interfaces
Parabolic	radius of curvature	(mm)	-0,4	0,4		
collimator	conic constant		-0,001	0,001		
	decenter z	(mm)	-0,100	0,100		
(axis)	decenter x	(mm)	-0,100	0,100		
	decenter y	(mm)	-0,100	0,100		
	tilt x	(degree)	-0,010	0,010	300	6
	tilt y	(degree)	-0,010	0,010	345	6
	tilt z	(degree)	-0,010	0,010	345	6
					One sided out-of-XY-plane positional error per interface pad, over base, over # of interfaces, RSS, mm	**0,02**
					One sided rotational displacement per pinholeset, over base, over # of interfaces, mm	**0,02**

continued on next page

			min	max	Transfer base, mm	Est. # of interfaces
Fold 3	radius of curvature	(mm)	lambda/10	lambda/10		
	decenter z	(mm)	-0,100	0,100		
	decenter x	(mm)	-0,100	0,100		
	decenter y	(mm)	-0,100	0,100		
	tilt x	(degree)	-0,010	0,010	174	6
	tilt y	(degree)	-0,010	0,010	200	6
	tilt z	(degree)	-1,000	1,000		
One sided out-of-XY-plane positional error per interface pad, over base, over # of interfaces, RSS, mm						**0,01**

			min	max	Transfer base, mm	Est. # of interfaces
Fold 4	radius of curvature	(mm)	lambda/10	lambda/10		
	decenter z	(mm)	-0,100	0,100		
	decenter x	(mm)	-0,100	0,100		
	decenter y	(mm)	-0,100	0,100		
	tilt x	(degree)	-0,010	0,010	165	6
	tilt y	(degree)	-0,010	0,010	190	6
	tilt z	(degree)	-1,000	1,000		
One sided out-of-XY-plane positional error per interface pad, over base, over # of interfaces, RSS, mm						**0,01**

			min	max	Transfer base, mm	Est. # of interfaces
Parabolic	radius of curvature	(mm)	-0,4	0,4		
camera	conic constant		-0,001	0,001		
	decenter z	(mm)	-0,050	0,050		6
(axis)	decenter x	(mm)	-0,100	0,100		
	decenter y	(mm)	-0,100	0,100		
	tilt x	(degree)	-0,010	0,010	113	6
	tilt y	(degree)	-0,010	0,010	165	6
	tilt z	(degree)	-0,010	0,010	165	6
Mounting plane offset error per interface, over # of interfaces, RSS, mm						**0,02**
One sided out-of-XY-plane positional error per interface pad, over base, over # of interfaces, RSS, mm						**0,01**
One sided rotational displacement per pinholeset, over base, over # of interfaces, mm						**0,01**

			min	max	Transfer base, mm	Est. # of interfaces
Fold 5	radius of curvature	(mm)	lambda/10	lambda/10		
	decenter z	(mm)	-0,050	0,050	N/A	
	decenter x	(mm)	-0,100	0,100		
	decenter y	(mm)	-0,100	0,100		
	tilt x	(degree)	-0,010	0,010	135	6
	tilt y	(degree)	-0,010	0,010	156	6
	tilt z	(degree)	-1,000	1,000		
One sided out-of-plane positional error per interface pad, over base, over # of interfaces, RSS, mm						**0,01**

			min	max	Transfer base, mm	Est. # of interfaces
Detector	decenter x	(mm)	-0,100	0,100		
	decenter y	(mm)	-0,100	0,100		
	tilt x	(degree)	-0,100	0,100		
	tilt y	(degree)	-0,100	0,100		

compensator	decenter z	(mm)	-2,000	2,000

A3: Throughput calculation for various bands and modes

MICADO Throughput

		#mirrors	I-Z band	Y-J band	H band	K band	
single mirror reflectance (Epner laser gold coating)			0.980	0.980	0.985	0.990	
primary arm		8.000	0.851	0.851	0.886	0.923	
auxiliary arm 1.5mas imaging		9.000	0.834	0.834	0.873	0.914	
auxiliary arm 4mas spectroscopy		7.000	0.868	0.868	0.900	0.932	
Entrance Window	AR coated ZnSe	0.95					
ADC	AR coated ZnSe/ZnS (1% / surface)	0.92					
grism efficiency		0.60					
			I band	Y band	J band	H band	K band
filters	as for HAWK-I		0.92	0.92	0.88	0.95	0.82
detector QE	ESO's detector memo		0.95	0.95	0.95	0.95	0.92
			I-Z bands	Y-J bands	H band	K band	
slit efficiencies	psf + diffraction		0.69	0.66	0.61	0.49	
Telescope	E-TRE-ESO-586-0252 issue 1	0.80	interface specification				
MAORY	E-TRE-INA-528-0004 issue 1	0.80	MAORY specification				

Throughputs (including detectors):	MICADO total	including telescope & AO
main channel 3mas imaging, Y-band	**0.65**	**0.42**
main channel 3mas imaging, J-band	**0.62**	**0.40**
main channel 3mas imaging, H-band	**0.70**	**0.45**
main channel 3mas imaging, K-band	**0.61**	**0.39**
auxiliary arm 1.5mas imaging, Y-band	**0.64**	**0.41**
auxiliary arm 1.5mas imaging, J-band	**0.61**	**0.39**
auxiliary arm 1.5mas imaging, H-band	**0.69**	**0.44**
auxiliary arm 1.5mas imaging, K-band	**0.60**	**0.39**
auxiliary arm 4mas, spectroscopy, 12mas slit, I-Z band	**0.28**	**0.18**
auxiliary arm 4mas, spectroscopy, 12mas slit, Y-J band	**0.26**	**0.16**
auxiliary arm 4mas, spectroscopy, 12mas slit, H band	**0.26**	**0.17**
auxiliary arm 4mas, spectroscopy, 12mas slit, K band	**0.18**	**0.12**

---oooOOOooo---